DEVELOPMENT AND SIMULATION OF A PSEUDOLITE-BASED FLIGHT REFERENCE SYSTEM

THESIS

Terry J. Bouska, Captain, USAF

AFIT/GE/ENG/03-03

DEPARTMENT OF THE AIR FORCE
AIR UNIVERSITY

AIR FORCE INSTITUTE OF TECHNOLOGY

Wright-Patterson Air Force Base, Ohio

APPROVED FOR PUBLIC RELEASE; DISTRIBUTION UNLIMITED

The views expressed in this thesis are those of the author and do not reflect the official policy or position of the United States Air Force, Department of Defense, or the United States Government.

AFIT/GE/ENG/03-03

DEVELOPMENT AND SIMULATION OF A PSEUDOLITE-BASED FLIGHT REFERENCE SYSTEM

THESIS

Presented to the Faculty of the

Department of Electrical and Computer Engineering

Graduate School of Engineering and Management

of the Air Force Institute of Technology

Air University

In Partial Fulfillment of the

Requirements for the Degree of

Master of Science

Terry J. Bouska, BS

Captain, USAF

March 2003

Approved for public release; distribution unlimited

AFIT/GE/ENG/03-03

DEVELOPMENT AND SIMULATION OF A PSEUDOLITE-BASED FLIGHT REFERENCE SYSTEM

Terry J. Bouska, BS

Captain, USAF

Approved:

Major John F. Raquet Thesis Advisor	Date
Doctor Peter S. Maybeck Committee Member	Date
Lieutenant Colonel Mikel M. Miller Committee Member	14 MAR 03 Date

Acknowledgements

I would like to thank my committee for their time and energy reviewing this thesis. Dr. Maybeck deserves credit for his expert advice in advanced Kalman filter theory. The largest source of thanks goes out to my advisor, Major John Raquet, because without him, this thesis would not have been possible. He was always happy to help me, and didn't run away or hide when he saw me coming up the hall with more questions. There isn't a more qualified person to serve as an advisor for this thesis topic, than Major Raquet.

I would like to thank my wife for her love and support for all the late nights, and times when although I was physically home, I was mentally working on my thesis.

Terry J. Bouska

Table of Contents

Page

Acknowledgements iii

List of Figures viii

List of Tables x

Abstract xi

I. Introduction 1-1

1.1 Background 1-1

1.2 Problem Definition 1-3

1.3 Related Research 1-4

1.4 Scope 1-5

1.5 Assumptions 1-6

1.6 Thesis Overview 1-6

II. Background 2-1

2.1 Overview 2-1

2.2 Kalman Filters 2-1

2.2.1 State and Measurement Model Equations . . . 2-2

2.2.2 Kalman Filter Equations 2-4

2.3 Extended Kalman Filters 2-5

2.3.1 State and Measurement Model Equations . . . 2-5

2.3.2 State and Measurement Model Linearization . 2-6

2.3.3 Extended Kalman Filter Equations 2-9

2.4 Optimal Smoothers 2-10

Page

2.5 Global Positioning System 2-11

2.5.1 GPS Signal 2-12

2.5.2 GPS Measurements 2-12

2.5.3 Code Measurements 2-12

2.5.4 Carrier-Phase Measurements 2-13

2.5.5 Single Differencing 2-15

2.5.6 Double Differencing 2-16

2.5.7 Widelane Measurements 2-18

2.5.8 Carrier-Phase Ambiguity Resolution 2-20

2.6 Pseudolites 2-25

2.6.1 GPS-Pseudolite Differences 2-25

2.6.2 Pseudolite Applications 2-26

2.6.3 Signal Interference and Near-Far Problem . . 2-27

2.6.4 Sources of Error 2-29

2.7 Summary 2-33

III. Methodology and Algorithm Development 3-1

3.1 Overview 3-1

3.2 Overall Simulation Design 3-1

3.3 Truth Model 3-1

3.4 Measurement and Measurement Model Error Generation 3-4

3.4.1 Pseudolite and Reference Receiver Position Errors 3-5

3.4.2 Measurement Noise 3-6

3.4.3 Multipath 3-6

3.4.4 Tropospheric Delay 3-9

3.5 Floating-Point Differential Pseudolite Kalman Filter . 3-10

3.5.1 Differential Pseudolite Model Equations . . . 3-11

Page

3.5.2 Differential Pseudolite Measurement Model . . 3-16

3.5.3 Discrete-Time Models 3-22

3.6 Floating-Point Filter Features 3-25

3.6.1 Pre-filter 3-25

3.6.2 Real Data Considerations 3-26

3.6.3 Tropospheric Model 3-30

3.6.4 Optimal Smoothing 3-30

3.6.5 Nonlinear Filtering 3-32

3.6.6 Weighted Measurement Covariance Matrix . . 3-34

3.6.7 Tropospheric Model Error States 3-35

3.7 Carrier-phase Ambiguity Resolution 3-38

3.8 Chapter Summary 3-39

IV. Results 4-1

4.1 Overview 4-1

4.2 Simulation Parameters, Scenario Descriptions and Test Case Definitions 4-1

4.3 Single Run Performance 4-5

4.4 Comparison of Code Versus Relative Motion for Ambiguity Convergence 4-11

4.5 Monte Carlo Performance 4-13

4.5.1 Baseline Filter 4-14

4.5.2 Error Sensitivity Analysis 4-16

4.5.3 Filter Enhancements 4-18

4.6 Alternate Trajectories with Nonlinear Filter Comparisons 4-27

4.6.1 Landing Scenario 4-27

4.6.2 Alternate Landing Scenario 4-30

4.6.3 Take Off Scenario 4-32

Page

4.7 Optimal Smoothing 4-33

4.8 Summary 4-35

V. Conclusions and Recommendations 5-1

5.1 Overview 5-1

5.2 Conclusions 5-1

5.3 Contributions 5-6

5.4 Recommendations 5-6

Bibliography BIB-1

Vita VITA-1

List of Figures

Figure		Page
1.1.	Pseudolite Aided Flight Reference System	1-4
2.1.	Single Difference GPS Between Receivers A and B and Satellite k	2-15
2.2.	Double Difference Between Satellites j and k with Receivers A and B	2-17
2.3.	Near-Far Problem	2-28
2.4.	Spherical and Planar Wavefronts	2-31
2.5.	Nonlinear Elongation of Range	2-32
3.1.	Pseudolite and Reference Receiver Relative Positions	3-2
3.2.	3-Dimensional View of Trajectory With Projections	3-3
3.3.	Position Error Effect on Ranges	3-6
3.4.	Typical Mobile Receiver Multipath Error for All Ten Pseudolites	3-8
3.5.	Typical Reference Receiver Multipath Error for All Ten Pseudolites	3-8
3.6.	Pseudolite Visibility Plot	3-26
3.7.	True Tropospheric Delay and Residual Tropospheric Error	3-36
3.8.	Residual Tropospheric Error Expressed as a Percent of Tropospheric Delay	3-37
3.9.	Ambiguity Resolution Algorithm Description	3-39
4.1.	Position Errors and Filter-Computed Standard Deviations (Dashed lines)	4-6
4.2.	3-Dimensional Position Error	4-7
4.3.	Filter-Estimated Velocity	4-8
4.4.	Filter-Estimated Acceleration	4-8

Figure Page

4.5. Code and Phase Ambiguity Residuals 4-10

4.6. Ambiguity Error and Ambiguity 1-σ Plots 4-11

4.7. RMS Ambiguity Error and Ambiguity 1-σ Plots for $\mathbf{R}_{code} = 10^{12} m^2$ 4-12

4.8. Filter Ambiguity Estimate Error and Ambiguity 1-σ Plots for Trajectory without Motion 4-13

4.9. Mobile and Reference Rcvr. Estimated Tropospheric Model Error Percentages for Tropospheric Delay Only 4-19

4.10. Mobile and Reference Rcvr. Tropospheric Model Error Percentages with all Measurement Errors 4-20

4.11. Combined Tropospheric Model Error Percentage with all Measurement Errors 4-21

4.12. Landing Scenario Trajectory Plot 4-28

4.13. Landing Scenario Pseudolite and Reference Receiver Locations with Trajectory Ground Projection 4-29

4.14. Alternate Landing Scenario Pseudolite and Reference Receiver Locations with Trajectory Ground Projection 4-30

4.15. Single Simulation Run for Alternate Landing Trajectory with an EKF 4-31

4.16. Single Simulation Run for Alternate Landing Trajectory with an EKF with Bias Correction Terms 4-31

4.17. Single Simulation Run for Takeoff Trajectory with an EKF (Initialized 73 meters away from a Pseudolite) 4-32

4.18. Visibility Plot for 20 Kilometer Maximum Range 4-34

4.19. Filter and Smoother RMS Ambiguity Error and Ambiguity 1-/sigma Plots 4-35

List of Tables

Table		Page
2.1.	Comparison between L1 and widelane (WL) phase errors (cycles)	2-19
3.1.	Pseudolite and Reference Receiver Truth Locations	3-2
3.2.	Multipath Parameter Values	3-7
3.3.	Floating-Point Filter Dynamics Driving Noise Values	3-15
3.4.	Floating-Point Filter Initial Covariance Values	3-16
3.5.	Measurement Covariance Values	3-22
4.1.	Atmospheric Parameters Used in Truth Model	4-2
4.2.	List of Scenario Descriptions	4-3
4.3.	Ambiguity Resolution Evaluation Criteria	4-5
4.4.	Widelane versus Single Frequency in Baseline Filter	4-14
4.5.	Baseline Single Frequency Retuned	4-16
4.6.	Best Case Error Sensitivity	4-17
4.7.	Worst Case Error Sensitivity	4-18
4.8.	Best Case Filter Enhancement	4-22
4.9.	Nominal Case Filter Enhancement	4-23
4.10.	Worst Case Filter Enhancement	4-24
4.11.	All Enhancement Test for Worst Case	4-25
4.12.	Weighted Measurement Covariance Matrix Scaling Factor Comparison	4-26
4.13.	Tropospheric Model Error States Time Constant Comparison	4-27
4.14.	Widelane versus Single Frequency in Baseline Filter	4-29

AFIT/GE/ENG/03-03

Abstract

Current flight reference systems are vulnerable to GPS jamming and also lack the accuracy required to test new systems. Pseudolites can augment flight reference systems by improving accuracy, especially in the presence of GPS jamming. This thesis evaluates a pseudolite-based flight reference system which applies and adapts carrier-phase differential GPS techniques. The algorithm developed in this thesis utilizes an extended Kalman filter along with carrier-phase ambiguity resolution techniques.

A simulation of the pseudolite-based positioning system realistically models measurement noise, multipath, pseudolite position errors, and tropospheric delay. A comparative evaluation of the algorithms performance for single and widelane frequency measurements is conducted in addition to a sensitivity analysis for each measurement error source, in order to determine design tradeoffs. Other analyses included the use of optimal smoothing, non-linear filtering techniques, and code averaging. Specific emphasis is given to two alternate methods, both developed in this research, for handling the residual tropospheric error after applying a standard tropospheric model.

Results indicate that the algorithm is capable of accurately resolving the pseudolite carrier-phase ambiguities, and providing a highly accurate (centimeter-level) navigation solution. The filter enhancements, particularly the optimal smoother and tropospheric error reduction methods, improved filter performance significantly.

DEVELOPMENT AND SIMULATION OF A PSEUDOLITE-BASED FLIGHT REFERENCE SYSTEM

I. Introduction

1.1 Background

Applications for the Global Positioning System (GPS) have increased tremendously since its inception, including the development of many differential GPS (DGPS) techniques. Differential GPS performs relative positioning between two or more receivers by calculating and removing sources of errors that are common between receivers. The integration of a GPS receiver and an Inertial Navigation System (INS) is another application that has produced accurate and robust navigation systems.

One of the most advanced navigation systems is the modern flight reference system operated by the 746th Test Squadron, Holloman AFB, NM, which is used to test and evaluate new flight navigation systems. To be useful, a flight reference system should have an order of magnitude greater accuracy than the system under test, because the output from the reference system is regarded as the truth. Any degradation in reference system performance will invalidate the evaluation of the system under test. The flight reference system has evolved through the years from radar tracking, ground-based camera and aircraft transponders, to the current system of DGPS integrated with an inertial unit, barometric altimeter, and a ground transponder/interrogator system [14]. The current reference system used by the 746th Test Squadron's Central Inertial Guidance Test Facility (CIGTF) is called the CIGTF High Accuracy Post-processing Reference System (CHAPS) [17].

The type of differential GPS that CHAPS uses is called carrier-phase DGPS, which relies on measuring the carrier component of GPS signals. The carrier-phase signal provides a relative measurement because the total number of carrier phase cycles are not known. Phase ambiguities exist, which are the unknown number of carrier-cycles present at the start of the signal integration [28]. The carrier signal can be broken up into two segments that are separated by the point in time that signal integration starts. The first segment consists of the unknown integer number of cycles up to the point of signal integration. The second segment consists of the measured carrier-phase, which is not constrained to be an integer. The highest level of accuracy is attained when the unknown number of cycles before signal integration is determined.

Carrier-phase DGPS can be categorized into two classes based on how the estimation of the unknown integer cycles is performed. Floating-point carrier-phase techniques estimate the integer number of cycles as floating-point numbers, without forming integer ambiguity values. Fixed-integer carrier-phase techniques select a set of integer ambiguities through a process called ambiguity resolution [15]. If the correct ambiguities are selected, a fixed-integer solution achieves greater accuracy than floating-point solution. Fixed-integer solutions are vulnerable to selecting the incorrect integers, which result in degraded performance.

CHAPS currently faces two challenges: accuracy during periods of GPS jamming and accuracy when a GPS signal is available. Operation in the presence of GPS signal interference impedes CHAPS from using its most accurate sensor. When jamming denies CHAPS from using GPS measurements, it must rely on its other sensors, primarily the INS. INS accuracy degrades over time, causing the performance of CHAPS to suffer. Although post-processing techniques are applied to reduce the impact of INS errors, CHAPS cannot maintain centimeter level accuracy during periods of GPS jamming. The second challenge facing CHAPS is accuracy when GPS

is available. As new systems become more accurate, CHAPS must also improve its accuracy to be a useful reference.

One technology that potentially solves the challenges of reference system accuracy is the use of pseudolites (or pseudo-satellites) [25]. Pseudolites are ground-based transmitters that send GPS-like signals which can be received with GPS receivers that are adapted for pseudolite signals. DGPS techniques, such as carrier-phase ambiguity resolution, can be adapted and applied for pseudolite navigation. Pseudolites have the flexibility of operating at various frequencies, which allow them to avoid GPS jamming signals.

The aiding with pseudolites will increase the accuracy of CHAPS or other flight reference systems when GPS jamming signals are present, and also during periods of normal GPS operation. Pseudolites potentially can provide CHAPS with a navigation source that maintains centimeter-level positioning accuracies during periods of GPS jamming. The increase in accuracy during normal (non-jamming) GPS operation is the result of CHAPS having access to two highly accurate sensors, as compared to just one when pseudolites are not used. A system that uses two sensors with roughly the same accuracy can expect to see a $1/\sqrt{2}$ factor improvement in accuracy over just using one sensor. That is nearly a 30 percent improvement, assuming that both sensors are independent. The errors between GPS and pseudolite signals are not completely independent, but a practical system would still show improvement over DGPS-only navigation.

1.2 Problem Definition

The primary goal of this thesis is the development and testing of an algorithm that resolves the carrier-phase ambiguities of ground-based GPS transmitters called pseudolites. Figure 1.1 depicts the process of resolving the ambiguities first to floating-point numbers in a Kalman filter, resolving the phase ambiguities to integer numbers, and then passing the carrier-phase measurements with resolved ambigui-

ties to aid the flight reference system. This research includes the simulation of the pseudolite environment, along with the creation of realistic errors in the pseudolite code and phase measurements. The secondary goals include analysis of the effect of each error source, and the application of new methodologies for dealing with pseudolite error sources. The objective of this work is to develop an algorithm that can improve both the accuracy and robustness to jamming of a flight reference system

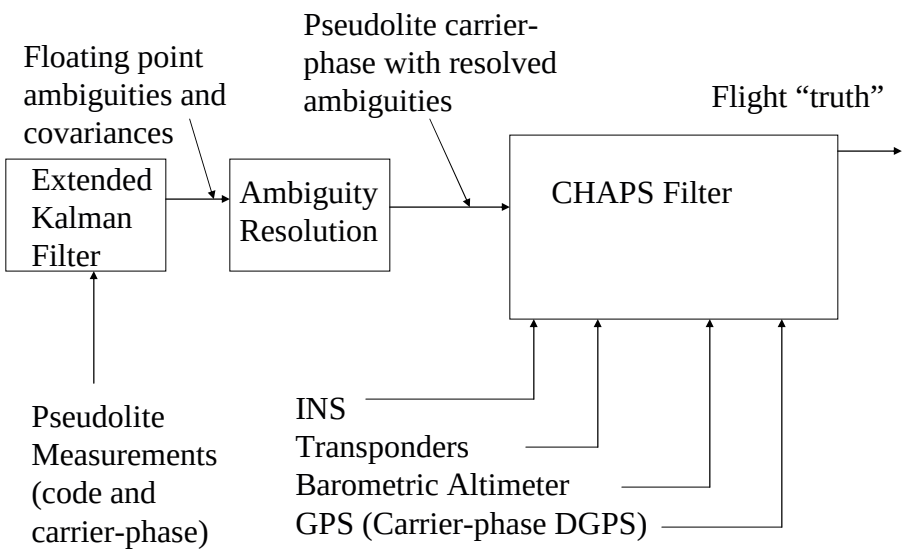

Figure 1.1 Pseudolite Aided Flight Reference System

1.3 Related Research

Raquet et al. [25] conducted an early test of a pseudolite-only flight reference system. This work was accomplished at Holloman AFB under the partnership of the 746th Test Squadron, NovAtel Communications, Stanford Telecom, and the University of Calgary. This proof of concept involved an "inverted" mode of operation in which the position of the pseudolite is solved in relation to an array of stationary receivers that are placed at known locations.

NovAtel Communications and Stanford Telecom continued work with pseudolite navigation by conducting a follow-on test to duplicate some of the results from the Holloman proof-of-concept test. They prototyped a GPS/pseudolite system that allowed coverage during times of reduced GPS availability [12].

Although pseudolite signals are very similar to GPS signals, many assumptions that are made for GPS navigation cannot be applied to pseudolite operations. Section 2.6.1 details the differences between GPS and pseudolite systems. Dai et al. [8] addressed some of the challenges that pseudolites present by developing unique modelling strategies to deal with pseudolite error sources. They also analyzed the impact of pseudolite-user geometry on differential pseudolite navigation.

1.4 Scope

The development of an extended Kalman filter to produce the floating point estimates of carrier-phase ambiguities and the ambiguity resolution techniques are the focus of this research. A simulation is used to evaluate the algorithm's integer ambiguity resolution performance. The scope of this thesis included the simulation and development of the pseudolite network, along with the generation of error-corrupted ranges between the pseudolites and the receivers.

All software development was developed in the Matlab 6.5 environment. An evaluation of single versus widelane frequency measurements is conducted. This thesis includes the sensitivity analysis of each pseudolite signal error source, including the impact on the ambiguity resolution process. It also explores new methodologies applied to reduce the effect of errors and improve the accuracy of estimated ambiguities. Two of these methodologies were developed as part of this research. This thesis does not address the design and implementation of pseudolite transmitters and receivers.

1.5 Assumptions

The following assumptions are made in this thesis:

a) Real-time ambiguity resolution is not required because the focus is the augmentation of a post-processed flight reference system.

b) The extended Kalman filter is not dependent upon a specific pseudolite system implementation. The pseudolite can utilize transmitters and receivers that operate at the GPS L1 and L2 frequency or in another band such as the S-band. GPS jamming is mitigated for L-band transmitters and receivers by the use of frequency translators.

c) All calculations use the Earth-Centered Earth-Fixed (ECEF) frame and World Geodetic Systems 1984 (WGS-84) coordinates.

d) No jamming analysis is required, because the pseudolites in a fielded system would operate at another frequency.

e) The sources of error present in the code and phase pseudolite measurements are assumed to be of similar characteristics to those available with high-quality GPS receivers.

f) Carrier-phase cycle slip detection is already accomplished.

1.6 Thesis Overview

Chapter 2 presents the background theory for this research through an in-depth review of Kalman filter methods, GPS fundamentals, carrier-phase ambiguity resolution, and pseudolite navigation. The section on Kalman filtering includes the derivation of an extended Kalman filter, optimal smoothing techniques, and conditional moment estimators. Chapter 3 details the error truth model, pseudolite filter models, and the carrier-phase ambiguity resolution techniques used in this thesis. Chapter 4 describes the single run and Monte Carlo analysis of the effects of each source of measurement error, along with the ability of filter enhancements to

improve the accuracy of the position and ambiguity solutions. Chapter 5 summarizes the results and provides recommendations for future research on a pseudolite-based reference system.

II. Background

2.1 Overview

This chapter begins by providing a basic overview of Kalman filter theory, including the extension to extended Kalman filter applications. The next section is on GPS operation and DGPS techniques. From there a section on pseudolites describes the challenges and issues of pseudolite navigation. The last section provides the theory behind the carrier-phase ambiguity resolution techniques used in this research.

2.2 Kalman Filters

Deterministic analysis has been successfully applied to many systems, but is not totally sufficient when applied to particular problems of interest. The linear Kalman filter is an optimal recursive data processing algorithm [19] that is a common tool technique that can be applied when deterministic analysis is not sufficient. The optimality is based on the assumptions that form the basis for Kalman filter, namely, an adequate model of the real-world application in the form of a linear dynamics model driven by white Gaussian noise of known statistics, from which are taken linear measurements, corrupted by white Gaussian noises of known statistics [19]. The Kalman filter can produce very sub-optimal results if either the dynamics or measurement model is an inadequate model of the real world [34]. The Kalman filter is also optimal because it incorporates all available measurements, regardless of their accuracy, to compute the estimates of the variables of interest based on the system dynamics and measurement models, the statistical description of the system noises, measurement errors, and the model uncertainties [15, 36, 19].

When discrete-time measurements are available, a Kalman filter includes both a time propagation cycle and an measurement update cycle. The propagation cycle

computes an estimate of the system state based on its previous system state and its (imperfect) dynamics model. The update cycle then uses the noise-corrupted measurements to refine the system state estimates. A complete derivation can be found in [19].

2.2.1 State and Measurement Model Equations. The following development is similar to those in references [15, 19]. The the system dynamics are assumed to be modeled as a linear system with a state equation of the form

$$\dot{\mathbf{x}}(t) = \mathbf{F}(t)\mathbf{x}(t) + \mathbf{B}(t)\mathbf{u}(t) + \mathbf{G}(t)\mathbf{w}(t) \tag{2.1}$$

where

$$\begin{aligned}
\mathbf{x}(t) &= \text{the n-dimensional system state vector} \\
\mathbf{F}(t) &= \text{the n-by-n state dynamics matrix} \\
\mathbf{B}(t) &= \text{the n-by-r control input matrix} \\
\mathbf{u}(t) &= \text{the r-dimensional control input} \\
\mathbf{G}(t) &= \text{the n-by-s noise input matrix} \\
\mathbf{w}(t) &= \text{the s-dimensional dynamics driving noise vector}
\end{aligned}$$

Upper case bold letters indicate matrices, lower case bold letters indicate vectors, and normal or italics represent scalar variables. Random vectors are denoted by boldface sans serif type. For the purposes of this research there are no control inputs, so the $\mathbf{B}$ and $\mathbf{u}$ terms will be dropped from any subsequent equations.

At discrete times the solution to equation (2.1) can be written as:

$$\mathbf{x}(t_{i+1}) = \mathbf{\Phi}(t_{i+1}, t_i)\mathbf{x}(t_i) + \left[\int_{t_i}^{t_{i+1}} \mathbf{\Phi}(t_{i+1}, \tau)\mathbf{G}(\tau)\boldsymbol{d\beta}(\tau)\right] \tag{2.2}$$

where $\boldsymbol{\beta}$ is a vector valued Brownian motion process of diffusion $\mathbf{Q}(t)$ [19], and $\mathbf{\Phi}(t_{i+1}, t_i)$ is the state transition matrix from t_i to t_{i+1} and is given by

$$\mathbf{\Phi}(t_{i+1}, t_i) = \mathbf{\Phi}(\Delta t) = e^{\mathbf{F}\Delta t} \text{ where } \Delta t \equiv t_{i+1} - t_i \tag{2.3}$$

which assumes a time-invariant $\mathbf{F}$ matrix. The equivalent discrete-time model is expressed by the stochastic difference equation as

$$\mathbf{x}(t_{i+1}) = \mathbf{\Phi}(t_{i+1}, t_i)\mathbf{x}(t_i) + \mathbf{w}_d(t_i) \tag{2.4}$$

where

$$\mathbf{w}_d(t_i) = \int_{t_i}^{t_{i+1}} \mathbf{\Phi}(t_{i+1}, \tau)\mathbf{G}(\tau)\boldsymbol{\beta}(\tau) \tag{2.5}$$

The discrete-time white Gaussian dynamics driving noise has the statistics:

$$E\{\mathbf{w}_d(t_i)\} = \mathbf{0} \tag{2.6}$$

$$E\{\mathbf{w}_d(t_i)\mathbf{w}_d^T(t_i)\} = \mathbf{Q}_d(t_i) = \int_{t_i}^{t_{i+1}} \mathbf{\Phi}(t_{i+1}, \tau)\mathbf{G}(\tau)\mathbf{Q}(\tau)\mathbf{G}^T(\tau)\mathbf{\Phi}^T(t_{i+1}, \tau)d\tau \tag{2.7}$$

$$E\{\mathbf{w}_d(t_i)\mathbf{w}_d^T(t_j)\} = \mathbf{0},\ \mathrm{t}_i \neq \mathrm{t}_j \tag{2.8}$$

Typical problems of interest are defined by a continuous-time dynamics process with discrete-time measurements produced by sensors. Assume the measurement model can be given as a linear, discrete-time system of the form

$$\mathbf{z}(t_i) = \mathbf{H}(t_i)\mathbf{x}(t_i) + \mathbf{v}(t_i) \tag{2.9}$$

The statistics of the measurement corruption noise are described by

$$E\{\mathbf{v}(t_i)\} = \mathbf{0} \tag{2.10}$$

$$E\{\mathbf{v}(t_i)\mathbf{v}^T(t_j)\} = \begin{cases} \mathbf{R}(t_i) & \text{for } t_i = t_j \\ \mathbf{0} & \text{for } t_i \neq t_j \end{cases} \tag{2.11}$$

The dynamics driving noise $\mathbf{w}_d(t_i)$ and the measurement corruption noise $\mathbf{v}(t_i)$ are assumed to be independent, so

$$E\{\mathbf{w}_d(t_i)\mathbf{v}^T(t_j)\} = \mathbf{0} \text{ for all } t_i \text{ and } t_j \tag{2.12}$$

2.2.2 Kalman Filter Equations. The Kalman filter propagates forward in time from t_{i-1}^+ to t_i^-, starting from the last update cycle state and covariance estimates. The superscripts "+" and "−" denote the time after a measurement update and before a measurement update respectively. Propagating the filter from t_i to t_{i+1} is equivalent to propagating from t_{i-1} to t_i. The initial conditions $\hat{\mathbf{x}}(t_0)$ and $\mathbf{P}(t_0)$ are used in the first propagation cycle. The propagation cycle is given by

$$\hat{\mathbf{x}}(t_i^-) = \mathbf{\Phi}(t_i, t_{i-1})\hat{\mathbf{x}}(t_{i-1}^+) \tag{2.13}$$

$$\mathbf{P}(t_i^-) = \mathbf{\Phi}(t_i, t_{i-1})\mathbf{P}(t_{i-1}^+)\mathbf{\Phi}^T(t_{i,}t_{i-1}) + \mathbf{G}_d(t_{i-1})\mathbf{Q}_d(t_{i-1})\mathbf{G}_d^T(t_{i-1}) \tag{2.14}$$

When measurements are available, the Kalman filter is updated by:

$$\mathbf{A}(t_i) = \mathbf{H}(t_i)\mathbf{P}(t_i^-)\mathbf{H}^T(t_i) + \mathbf{R}(t_i) \tag{2.15}$$

$$\mathbf{K}(t_i) = \mathbf{P}(t_i^-)\mathbf{H}^T(t_i)\mathbf{A}(t_i)^{-1} \tag{2.16}$$

$$\mathbf{r}(t_i) = \mathbf{z}_i - \mathbf{H}(t_i)\hat{\mathbf{x}}(t_i^-) \tag{2.17}$$

$$\hat{\mathbf{x}}(t_i^+) = \hat{\mathbf{x}}(t_i^-) + \mathbf{K}(t_i)\mathbf{r}(t_i) \tag{2.18}$$

$$\mathbf{P}(t_i^+) = \mathbf{P}(t_i^-) - \mathbf{K}(t_i)\mathbf{H}(t_i)\mathbf{P}(t_i^-) \tag{2.19}$$

A properly designed filter has a zero-mean residual vector $\mathbf{r}(t_i)$ with the filter-computed covariance $\mathbf{A}(t_i)$ [15]. The outputs of the Kalman filter update cycle are $\hat{\mathbf{x}}(t_i^+)$ and $\mathbf{P}(t_i^+)$, which are then used in the next propagation cycle.

2.3 Extended Kalman Filters

The linear Kalman filter cannot be used when either the state dynamics or measurement model contains nonlinearities. Methods that choose to ignore old data due to cumulative errors, or that decrease the filter's confidence in the adequacy of the filter model have been used to address the problem of nonlinearities. A better way to deal with nonlinearities is through a linearization of the measurement or dynamics model, thus enabling linearized estimation techniques.

A linearized Kalman filter consists of a first order Taylor series approximation to the nonlinear models, linearizing about a nominal trajectory that is normally pre-computed. The extended Kalman filter (EKF) differs from the linearized Kalman filter in that it relinearizes about each state estimate as it progresses, enabling it to handle larger degrees of nonlinearities more adequately. A complete derivation of extended Kalman filters can be found in reference [20].

2.3.1 State and Measurement Model Equations. Following the Kalman filter development in references [15, 20], a nonlinear system dynamics model takes the form

$$\dot{\mathbf{x}}(t) = \mathbf{f}[\mathbf{x}(t), t] + \mathbf{G}(t)\mathbf{w}(t) \tag{2.20}$$

The state dynamics vector is now defined to be a possibly nonlinear function of the n-dimensional state vector $\mathbf{x}(t)$, and of the continuous time, t, itself. The definitions of the n-dimensional state dynamics vector $\mathbf{x}(t)$ and the n-by-s noise distribution matrix $\mathbf{G}(t)$ are unchanged from those seen in association with Equation 2.1. The dynamics driving noise vector $\mathbf{w}(t)$ is also unchanged and assumed to be white

Gaussian noise process with mean and covariances defined by:

$$E\{\mathbf{w}(t)\} = \mathbf{0} \tag{2.21}$$

$$E\{\mathbf{w}(t)\mathbf{w}^T(t+\tau)\} = \mathbf{Q}(t)\delta(\tau) \tag{2.22}$$

where τ has units of time.

The nonlinear discrete-time measurement equation takes the form

$$\mathbf{z}(t_i) = \mathbf{h}[\mathbf{x}(t_i), t_i] + \mathbf{v}(t_i) \tag{2.23}$$

The m-dimensional measurement vector $\mathbf{z}(t_i)$ is a linear or nonlinear function of the state vector and time ($\mathbf{h}[\mathbf{x}(t_i), t_i]$), corrupted by the linearly additive m-dimensional discrete-time noise input vector $\mathbf{v}(t_i)$. The discrete-time noise vector is unchanged from that of the linear Kalman filter.

2.3.2 State and Measurement Model Linearization. If either the system or measurement model equations 2.20 and 2.23 are nonlinear, they must be linearized in order to produce an optimal state estimate, to first order. Reference [20] uses a perturbation technique of the state about a nominal or reference trajectory. The dynamics model for this research is linear, but the linearization of both the dynamics model and measurement model is presented for completeness.

The nominal state trajectory can be generated from the initial condition $\mathbf{x}_n(t_0) = \mathbf{x}_{n0}$ and the differential equation

$$\dot{\mathbf{x}}_n(t) = \mathbf{f}[\mathbf{x}_n(t), t] \tag{2.24}$$

which differs from the nonlinear state equation by being deterministic. The nominal measurements can be defined in a similar fashion by

$$\mathbf{z}_n(t_i) = \mathbf{h}[\mathbf{x}_n(t_i), t_i] \tag{2.25}$$

which is also deterministic. The perturbation state derivative $\delta\dot{\mathbf{x}}(t)$, is formed by the subtraction of the nominal trajectory (2.24) from the system model (2.20) to give

$$\delta\dot{\mathbf{x}}(t) \equiv [\dot{\mathbf{x}}(t) - \dot{\mathbf{x}}_{\mathrm{n}}(t)] = \mathbf{f}[\mathbf{x}(t), t] - \mathbf{f}[\mathbf{x}_{\mathrm{n}}(t), t] + \mathbf{G}(t)\mathbf{w}(t) \tag{2.26}$$

A Taylor series expansion of $\mathbf{f}[\mathbf{x}(t), t]$ about $\mathbf{x}_{\mathrm{n}}(t)$ yields

$$\mathbf{f}[\mathbf{x}(t), t] = \mathbf{f}[\mathbf{x}_{\mathrm{n}}, t] + \left.\frac{\partial \mathbf{f}[\mathbf{x}(t), t]}{\partial \mathbf{x}}\right|_{\mathbf{x}=\mathbf{x}_n(t)} [\mathbf{x}(t) - \mathbf{x}_n(t)] + h.o.t. \tag{2.27}$$

where "*h.o.t.*" represents the higher order terms in powers of $[\mathbf{x}(t) - \mathbf{x}_n(t)]$ greater than one [20]. When Equation 2.27 is substituted into Equation 2.26, the $\mathbf{f}[\mathbf{x}_{\mathrm{n}}(t), t]$ term is cancelled to produce the perturbation equation. The first order approximation ignores the higher order terms which yields

$$\dot{\delta\mathbf{x}}(t) = \mathbf{F}[t; \mathbf{x}_n(t)]\delta\mathbf{x}(t) + \mathbf{G}(t)\mathbf{w}(t) \tag{2.28}$$

This linearized dynamics equation can be implemented in a linearized Kalman filter with the n-by-n partial derivative matrix $\mathbf{F}[t; \mathbf{x}_n(t)]$ evaluated along a nominal trajectory and defined as

$$\mathbf{F}[t; \mathbf{x}_n(t)] = \left.\frac{\partial \mathbf{f}[\mathbf{x}, t]}{\partial \mathbf{x}}\right|_{\mathbf{x}=\mathbf{x}_n(t)} \tag{2.29}$$

This approximation is valid as long as the higher order terms of the Taylor series expansion are negligible.

The development of the measurement perturbation equation is formed in a similar way. The measurement perturbation $\delta\mathbf{z}(t)$ is formed by the subtraction of the nominal measurement Equation 2.25 from the measurement model Equation 2.23 to give

$$\delta\mathbf{z}(t_\mathrm{i}) \equiv [\mathbf{z}(t_i) - \mathbf{z}_n(t_i)] = \mathbf{h}[\mathbf{x}(t_i), t_i] - \mathbf{h}[\mathbf{x}_\mathrm{n}(t_i), t_i] + \mathbf{v}(t_i) \tag{2.30}$$

A Taylor series expansion of $\mathbf{h}[\mathbf{x}(t_i), t_i]$ about $\mathbf{x}_\mathrm{n}(t)$ yields

$$\mathbf{h}[\mathbf{x}(t_i), t_i] = \mathbf{h}[\mathbf{x}_\mathrm{n}(t_i), t_i] + \left.\frac{\partial \mathbf{h}[\mathbf{x}, t_i]}{\partial \mathbf{x}}\right|_{\mathbf{x}=\mathbf{x}_\mathrm{n}(t_i)} [\mathbf{x}(t_i) - \mathbf{x}_n(t_i)] + h.o.t. \tag{2.31}$$

When Equation 2.31 is substituted into Equation 2.30, the $\mathbf{h}[\mathbf{x}_\mathrm{n}(t_i), t_i]$ term is cancelled to produce the perturbation equation. The first order approximation ignores the higher order terms which yields

$$\delta\mathbf{z}(t_\mathrm{i}) \equiv \mathbf{H}[t_i; \mathbf{x}_n(t_i)]\delta\mathbf{x}(t_i) + \mathbf{v}(t_i) \tag{2.32}$$

This linearized measurement equation can be implemented in the linearized Kalman filter with the m-by-n partial derivative matrix $\mathbf{H}[t_i; \mathbf{x}_n(t_i)]$ evaluated along a nominal trajectory and defined as:

$$\mathbf{H}[t_i; \mathbf{x}_n(t_i)] = \left.\frac{\partial \mathbf{h}[\mathbf{x}, t_i]}{\partial \mathbf{x}}\right|_{\mathbf{x}=\mathbf{x}_\mathrm{n}(t_i)} \tag{2.33}$$

This approximation is valid as long as the higher order terms of the Taylor series expansion in Equation 2.31 are negligible. The state and measurement perturbation equations are error state representations which must be added to the nominal state values to produce the total state estimate.

The equations developed in this section define the linearized Kalman filter. Real-world measurements $\mathbf{z}(t_i)$ are differenced with $\mathbf{z}_n(t_i)$ computed via Equation 2.25, and then fed into a linear Kalman filter based on Equations 2.28 and 2.32, to generate estimates of $\delta\mathbf{x}(t)$. These can be added to $\mathbf{x}_n(t)$, generated as solutions to

Equation 2.24, to estimate the total states. It is important to point out that the EKF relinearizes the model about the new estimate ($\hat{\mathbf{x}}(t_i^+)$) and the corresponding trajectory. The relinearization process helps to validate the assumption that the deviations from the nominal trajectory are sufficiently small.

2.3.3 Extended Kalman Filter Equations. The extended Kalman filter propagates forward in time t_{i-1} to t_i by integrating from the last update cycle, state and covariance estimates. The initial conditions $\hat{\mathbf{x}}(t_0)$ and $\mathbf{P}(t_0)$ are used in the first propagation cycle. The EKF propagation equations are defined by:

$$\dot{\hat{\mathbf{x}}} = \mathbf{f}[\hat{\mathbf{x}}(t|t_{i-1}), t] \tag{2.34}$$

$$\dot{\mathbf{P}}(t|t_{i-1}) = \mathbf{F}[t; \hat{\mathbf{x}}(t|t_{i-1})]\mathbf{P}(t|t_{i-1}) + \mathbf{P}(t|t_{i-1})\mathbf{F}^T[t; \hat{\mathbf{x}}(t|t_{i-1})] + \mathbf{G}(t)\mathbf{Q}(t)\mathbf{G}^T(t) \tag{2.35}$$

with $t|t_{i-1}$ denoting the value of a given variable at time t, conditioned on all the measurements up to and including time t_{i-1}. The term $\mathbf{F}[t; \hat{\mathbf{x}}(t|t_{i-1})]$ is the n-by-n partial derivative matrix:

$$\mathbf{F}[t; \hat{\mathbf{x}}(t|t_{i-1})] = \left.\frac{\partial \mathbf{f}[\mathbf{x}, \mathbf{u}(t), t]}{\partial \mathbf{x}}\right|_{\mathbf{x}=\hat{\mathbf{x}}(t|t_{i-1})} \tag{2.36}$$

The differential equation initial conditions are given by

$$\hat{\mathbf{x}}(t_{i-1}|t_{i-1}) \equiv \hat{\mathbf{x}}(t_{i-1}^+) \tag{2.37}$$

$$\mathbf{P}(t_{i-1}|t_{i-1}) \equiv \mathbf{P}(t_{i-1}^+) \tag{2.38}$$

After integrating equations (2.34) and (2.35) to the next sample time, the state and covariance estimates are defined as:

$$\hat{\mathbf{x}}(t_i^-) \equiv \hat{\mathbf{x}}(t_i|t_{i-1}) \tag{2.39}$$

$$\mathbf{P}(t_i^-) \equiv \mathbf{P}(t_i|t_{i-1}) \tag{2.40}$$

The EKF incorporates the measurements in the following update equations:

$$\mathbf{K}(t_i) = \mathbf{P}(t_i^-)\mathbf{H}^T[t_i;\hat{\mathbf{x}}(t_i^-)]\{\mathbf{H}[t_i;\hat{\mathbf{x}}(t_i^-)]\mathbf{P}(t_i^-)\mathbf{H}^T[t_i;\hat{\mathbf{x}}(t_i^-)] + \mathbf{R}(t_\mathrm{i})\}^{-1} \tag{2.41}$$

$$\hat{\mathbf{x}}(t_\mathrm{i}^+) = \hat{\mathbf{x}}(t_\mathrm{i}^-) + \mathbf{K}(t_\mathrm{i})\{\mathbf{z}_i - \mathbf{h}[\hat{\mathbf{x}}(t_\mathrm{i}^-), t_i]\} \tag{2.42}$$

$$\mathbf{P}(t_\mathrm{i}^+) = \mathbf{P}(t_\mathrm{i}^-) - \mathbf{K}(t_\mathrm{i})\mathbf{H}[t_i;\hat{\mathbf{x}}(t_\mathrm{i}^-)]\mathbf{P}(t_\mathrm{i}^-) \tag{2.43}$$

2.4 Optimal Smoothers

The traditional Kalman filters runs forward in time—that is, it incorporates all information available up to and including the current time. An estimator that uses future data to improve the state and covariance estimate at the current time is called an optimal smoother. The three class of smoothers include the fixed-interval, fixed-point and fixed-lag smoothers [20]. The fixed-interval smoother is the type that was used in this research.

A fixed-interval smoother can be conceptualized by the combination of two filters. The first is a traditional forward-running Kalman filter, and the second is a backward-running Kalman filter that is of inverse covariance formulation [20]. The smoothed estimate is formed by combining the forward and backward state estimates, using a weighting based on their respective covariance matrices. An equivalent approach to the forward-backward configuration was developed by Meditch [20]. The filter requires that the state and covariance matrices be stored both before and after measurement updates. The state transition matrices are also required. Once the forward filter is run through all data until the final time, the smoothed state estimate at the last time increment is set equal to the state estimate from the forward running filter after the last measurement update, which is denoted by

$$\hat{\mathbf{x}}(t_f|t_f) = \hat{\mathbf{x}}(t_f^+) \tag{2.44}$$

Then, starting with the second-to-last time increment, and running backward in time, the smoothed estimate is defined as

$$\hat{\mathbf{x}}(t_i|t_f) = \hat{\mathbf{x}}(t_i^+) + \mathbf{A}(t_i)[\hat{\mathbf{x}}(t_{i+1}|t_f) - \hat{\mathbf{x}}(t_{i+1}^-)] \tag{2.45}$$

where the matrix $\mathbf{A}(t_i)$ is defined as the smoothing estimator gain matrix [20], given by

$$\mathbf{A}(t_i) = \mathbf{P}(t_i^+)\mathbf{\Phi}^T(t_{i+1}, t_i)\mathbf{P}^{-1}(t_{i+1}^-) \tag{2.46}$$

In a similar manner, the covariance at the final time increment is defined as

$$\mathbf{P}(t_f|t_f) = \mathbf{P}(t_f^+) \tag{2.47}$$

and the covariance at every other time increment is calculated by

$$\mathbf{P}(t_i|t_f) = \mathbf{P}(t_i^+) + \mathbf{A}(t_i)[\mathbf{P}(t_{i+1}|t_f) - \mathbf{P}(t_f^+)]\mathbf{A}^{\mathrm{T}}(t_i) \tag{2.48}$$

Smoothers outperform standard Kalman filters particularly when the dynamics model includes relatively large dynamic driving noises. The more uncertainty in the model, the greater the benefit from incorporating future information. At the last time epoch, the smoothed estimate is equal to the forward filter state estimate. A more rigorous derivation of smoothers can be found in reference [20].

2.5 Global Positioning System

The Global Positioning System uses a constellation of medium earth orbit satellites to provide a continuous ranging source. The user can calculate position, velocity, and time from the received signal. Differential GPS (DGPS) is a term that includes many different methods and techniques that result in a greater accuracy than stand alone GPS. A detailed overview of GPS concepts can be found in references [21, 26].

2.5.1 GPS Signal. The GPS signal contains both a code and carrier-phase component. The GPS code that is available to civilian users is the Coarse/Acquisition (C/A) code while the military also has the precision (P) code (which is called P(Y) after encryption). The carrier-phase frequencies are currently set at 1575.42 MHz and 1227.6 MHz, which are called the L1 and L2 frequencies respectively [21]. The P(Y) is transmitted on both L1 and L2 while the C/A code is only available on the L1 frequency. The 1023 bit sequence C/A code repeats every millisecond and the P(Y) repeats every 7 days per satellite. The chipping rates for the C/A and P codes are 1.023 MHz and 10.23 MHz respectively. The code component of the GPS signal contain a pseudorandom noise (PRN) code that is unique to each satellite.

Civilian receivers can only track the C/A code on the L1 frequency. Military receivers that track both the P(Y) codes on the L1 and L2 frequencies are called dual-frequency receivers. Some civilian receivers use semi-codeless techniques that can be used to get range information from the P(Y) code without actually decrypting it [15, 34]. These high-precision civilian receivers are used in CHAPS to get the L2 carrier-phase information without really tracking the P(Y) code.

2.5.2 GPS Measurements. Typically, there are three measurements from a GPS receiver—code, doppler, and carrier-phase. The code measurement is often called a "pseudorange" because it is the actual range corrupted by measurement errors (primarily the clock error). The Doppler measurement describes the frequency shift in the signal due to vehicle (and clock) dynamics, and the carrier-phase can be thought of as an integrated Doppler. The term "raw" is included to distinguish these measurements from the navigation processor outputs such as position, velocity, and acceleration. DGPS techniques will be distinguished based on the use of code, carrier-phase, or both.

2.5.3 Code Measurements. The code pseudorange is true range between the satellite and user plus the impact of a number of error sources. The pseudo-

range is calculated as the time difference between the transmission and reception time multiplied by speed of light (to give the range in meters). The pseudorange measurement can be expressed as:

$$\rho = r + c(\delta t_u - \delta t_{sv}) + T + I + m_\rho + v_\rho \tag{2.49}$$

where

$$\begin{aligned}
\rho &= \text{GPS pseudorange measurement (meters)} \\
r &= \text{true range from the user to satellite (meters)} \\
c &= \text{speed of light (meters / second)} \\
\delta t_u &= \text{receiver (user) clock error (seconds)} \\
\delta t_{sv} &= \text{transmitter (satellite vehicle) clock error (seconds)} \\
T &= \text{errors due to tropospheric delay (meters)} \\
I &= \text{errors due to ionospheric delay (meters)} \\
m_\rho &= \text{errors due to pseudorange multipath (meters)} \\
v_\rho &= \text{errors in pseudorange due to receiver noise (meters)}
\end{aligned}$$

2.5.4 Carrier-Phase Measurements. The carrier-phase of the received signal can also be used for positioning, especially when high precision is required. The carrier-phase measurement can be expressed in cycles as:

$$\phi = \lambda^{-1}(r + c(\delta t_u - \delta t_{sv}) + T - I + m_\phi + v_\phi) + N \tag{2.50}$$

where

ϕ= carrier-phase measurement (cycles)

λ= carrier-phase wavelength (meters / cycle)

N= carrier-phase integer ambiguity (cycles)

T= errors due to tropospheric delay (meters)

I= errors due to ionospheric delay (meters)

m_ϕ= errors due to carrier-phase measurement multipath (meters)

v_ϕ= errors in carrier-phase measurement due to receiver noise (meters)

The rest of the terms were previously defined in Equation (2.49) except that the measurement noise and multipath are different and significantly less for the carrier-phase than for the code. Some sources of error do not affect the code and carrier-phase measurement in the same manner. The sign on the ionospheric delay term is opposite from the code measurement equation, because the ionosphere advances a carrier-phase measurement, but delays a code measurement. This phenomenon is called code-carrier divergence. Tropospheric delay affects both the code and carrier-phase by the same magnitude.

The carrier-phase integer ambiguity term is an error source that is present in carrier-phase measurements, but not in code measurements. The ambiguity term represents the unknown number of carrier-cycles present at the start of the signal integration [28]. The carrier signal can be broken up into two segments that are separated by the point in time that signal integration starts. The first segment consists of the unknown integer number of cycles up to the point of signal integration. The second segment consists of the measured carrier-phase which is not constrained to be an integer. A high level of accuracy is attained when the unknown number of cycles before signal integration is determined.

2.5.5 Single Differencing. Differential GPS uses linear combinations of observations (code or carrier measurements) between receivers, satellites, or times to reduce the effect of some errors [22]. A single difference can be between two satellites (∇) or between two receivers ($\triangle$). Figure 2.1 depicts the concept of a single difference between two receivers.

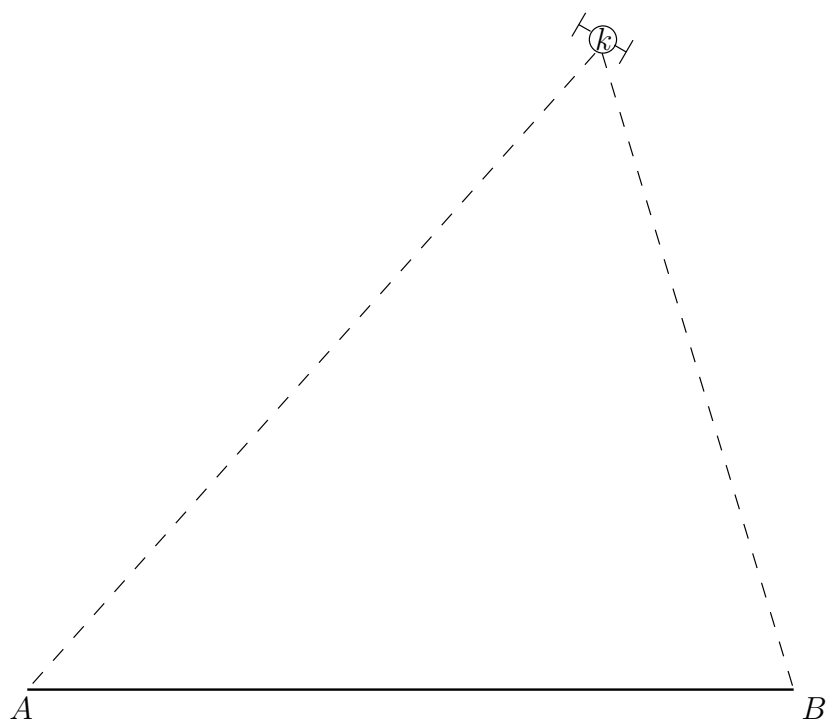

Figure 2.1 Single Difference GPS Between Receivers A and B and Satellite k

The single-differenced carrier-phase measurement between two receivers corresponding to the above figure is defined as

$$\Delta\phi_{AB}^{k} \equiv \phi_{A}^{k} - \phi_{B}^{k} \tag{2.51}$$

where ϕ_A^k is the phase measurement between receiver A and satellite k, and ϕ_B^k is the phase measurement between receiver B and satellite k.

This type of difference eliminates the satellite clock error and reduces the atmospheric errors. Combining the carrier-phase measurement Equation 2.50 with

the single difference Equation 2.51 yields

$$\begin{aligned}\Delta\phi_{AB}^k = \lambda^{-1}[r_A^k + c(\delta t_{u_A}^k - \delta t_{sv_A}^k) + T_A^k - I_A^k + m_{\phi A}^k + v_{\phi A}^k] + N_A^k \\ - \lambda^{-1}[r_B^k + c(\delta t_{u_B}^k - \delta t_{sv_B}^k) + T_B^k - I_B^k + m_{\phi B}^k + v_{\phi B}^k] + N_B^k \end{aligned} \tag{2.52}$$

Combining like terms yields

$$\begin{aligned}\Delta\phi_{AB}^k = \lambda^{-1}[(r_A^k - r_B^k) + c(\delta t_{u_A}^k - \delta t_{u_B}^k) - c(\delta t_{sv_A}^k - \delta t_{sv_B}^k) + (T_A^k - T_B^k) \\ - (I_A^k - I_B^k) + (m_{\phi A}^k - m_{\phi B}^k) + (v_{\phi A}^k - v_{\phi B}^k)] + (N_A^k - N_B^k) \end{aligned} \tag{2.53}$$

After the satellite clock term is eliminated (because the measurements are synchronous and the satellite clock error is the same for both), differences are represented as (Δ), and the above equation can be written as

$$\Delta\phi_{AB}^k = \lambda^{-1}(\Delta r_{AB}^k + c\Delta\delta t_{u_{AB}}^k + \Delta T_{AB}^k - I_{AB}^k + \Delta m_{\phi AB}^k + v_{\phi AB}^k) + \Delta N_{AB}^k \tag{2.54}$$

The integer value ΔN_{AB}^k is the difference in the carrier-phase ambiguity between the two receivers' measurements.

2.5.6 Double Differencing. A double difference is the combination of a single difference between satellites (transmitters) and a single difference between receivers. Because a single difference between receivers cancels the satellite clock error and a single difference between satellites cancels the receiver clock error, the double difference cancels both clock error terms. Figure 2.2 displays the concept of a double difference.

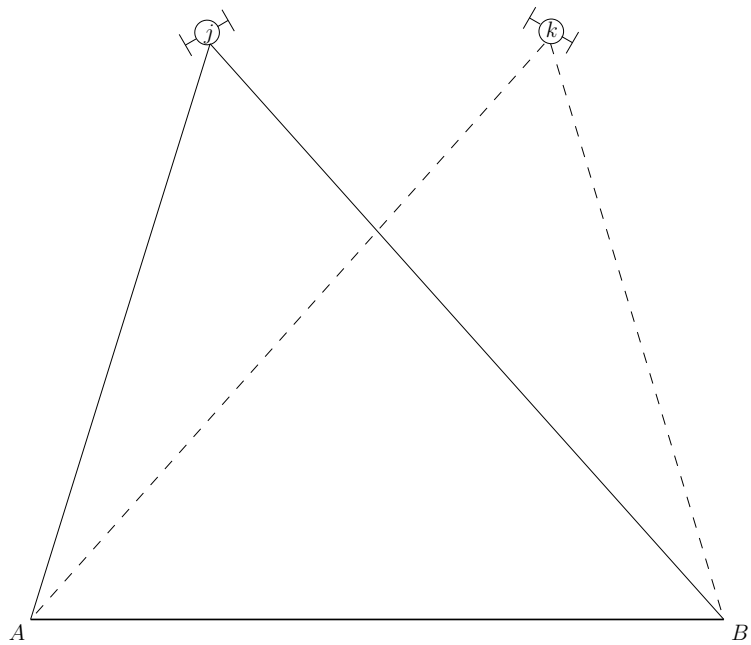

Figure 2.2 Double Difference Between Satellites j and k with Receivers A and B

The phase measurement will be used in the following example. The double differenced carrier-phase measurement is defined as

$$\Delta\nabla\phi^k_{AB}j = \Delta\phi^k_{AB} - \Delta\phi^j_{AB} \tag{2.55}$$

After the single differenced phase Equation 2.54 is substituted in the above equation, it yields

$$\begin{aligned}\Delta\nabla\phi^k_{AB}j = \lambda^{-1}(&\Delta r^k_{AB} + c\Delta\delta t^k_{u_{AB}} + \Delta T^k_{AB} - \Delta I^k_{AB} + \Delta m^k_{AB} + \Delta v^k_{AB} + \Delta N^k_{AB} \\ &- \left[\lambda^{-1}(\Delta r^j_{AB} + c\Delta\delta t^j_{u_{AB}} + \Delta T^j_{AB} - \Delta I^j_{AB} + \Delta m^j_{\phi AB} + \Delta v^j_{\phi AB} + \Delta N^j_{AB}\right]\end{aligned} \tag{2.56}$$

When the user clock error term is cancelled and the double difference operator ($\Delta\nabla$) is used to express the double difference error terms, the equation can be written as

$$\Delta\nabla\phi^{kj}_{AB} = \lambda^{-1}(\Delta\nabla r^{kj}_{AB} + \Delta\nabla T^{kj}_{AB} - \Delta\nabla I^{kj}_{AB} + \Delta\nabla m^{kj}_{\phi AB} + \Delta\nabla v^{kj}_{\phi AB}) + \Delta\nabla N^{kj}_{AB} \tag{2.57}$$

Differencing reduces the effects of frequency correlated errors (such as the atmospheric errors) at the expense of increasing the effects of uncorrelated frequency errors (such as measurement noise and multipath). The single difference increases the magnitude of the noise and multipath by a factor of ($\sqrt{2}$) and the double difference increases the magnitude by a factor of 2. Although the integer ambiguity term ($\Delta\nabla N_{AB}^{kj}$) is different from the ambiguity term from the observation equation, it has maintained its integer nature.

The double differenced code measurement can be adapted from Equation 2.57 by dropping the ambiguity terms and expressing the range in terms of meters, yielding

$$\Delta\nabla\rho_{AB}^{kj} = \Delta\nabla r_{AB}^{kj} + \Delta\nabla T_{AB}^{kj} - \Delta\nabla I_{AB}^{kj} + \Delta\nabla m_{\rho AB}^{kj} + \Delta\nabla v_{\rho AB}^{kj} \tag{2.58}$$

It is important to note that double-difference code measurements are not typically used. Rather, single difference measurements are used and the receiver clock error is estimated directly.

2.5.7 Widelane Measurements. When two GPS frequencies are available, linear combinations can be formed to create new virtual frequencies. The widelane measurement is commonly used in DGPS applications and can be written as [28]

$$\phi_{WL} = \phi_{L1} - \phi_{L2} \tag{2.59}$$

The widelane measurement has a wavelength of approximately 86.19 cm, while the wavelengths of signals at the L1 and L2 frequency are 19.03 cm and 24.42 cm, respectively. Although the integer ambiguity value for a widelane measurement is different from either of the values for the L1 or L2 frequency, it is still an integer.

Table 2.1 shows a comparison between error sources for a widelane versus single frequency in terms of cycles, where c represents the speed of light and f_1 and f_2 are

Table 2.1 Comparison between L1 and widelane (WL) phase errors (cycles)

Error	L1 error (cycles)	WL error (cycles)	WL/L1 ratio
SV Position	$\frac{1}{\lambda_1}\nabla\Delta\delta p_{sv}$	$\frac{1}{\lambda_{WL}}\nabla\Delta\delta_{p_{SV}}$	$\frac{\lambda_1}{\lambda_{WL}} \approx 0.221$
Troposphere	$\frac{1}{\lambda_1}\nabla\Delta T$	$\frac{1}{\lambda_{WL}}\nabla\Delta T$	$\frac{\lambda_1}{\lambda_{WL}} \approx 0.221$
Ionosphere	$\frac{1}{\lambda_1 f_1^2}\nabla\Delta I$	$-\frac{(f_1-f_2)}{cf_1f_2}\nabla\Delta I$	$\frac{(f_1-f_2)}{f_2} \approx 0.283$
L1 Multipath	$\frac{1}{\lambda_1}\nabla\Delta m_\phi$	$\frac{1}{\lambda_1}\nabla\Delta m_\phi$	1
L1 Noise	$\frac{1}{\lambda_1}\nabla\Delta v_\phi$	$\frac{1}{\lambda_1}\nabla\Delta v_\phi$	1
L2 Multipath	$\frac{1}{\lambda_2}\nabla\Delta m_\phi$	$\frac{1}{\lambda_2}\nabla\Delta m_\phi$	1
L2 Noise	$\frac{1}{\lambda_2}\nabla\Delta v_\phi$	$\frac{1}{\lambda_2}\nabla\Delta v_\phi$	1

the frequencies of L1 and L2 respectively [28]. The widelane significantly reduces the impact of the correlated error sources (i.e., the satellite and receiver position errors and the atmospheric errors). Measurement noise and multipath are frequency uncorrelated and thus not reduced by a widelane implementation.

Although the widelane measurement reduces some of the error sources when expressed in cycles, it actually increases some of the error sources when expressed in meters. To convert the widelane to L1 ratio, a conversion of $\frac{\lambda_{WL}}{\lambda_1} \approx 4.529$ is multiplied by the ratio give in the table. This means that, when the multipath and measurement noise are not affected in terms of cycles, the effect is amplified by a factor of approximately 4.529 when expressed in meters. The satellite position, receiver position, and tropospheric errors are reduced when expressed in cycles, but are unaffected when expressed in terms of meters of error. The ionospheric error is slightly increased in terms of meters for a widelane measurement, but this error source will be ignored for pseudolite applications.

The longer wavelength of a widelane measurement reduces the number of candidate ambiguity sets that are generated within the ambiguity resolution search space (see Section 2.5.8). This makes ambiguity resolution easier and more reliable, but with a decreased accuracy when compared to a single frequency, because the errors in the widelane phase measurements are actually larger than the single frequency

case. A more detailed discussion on linear combinations of measurements can be found in references [22, 28].

2.5.8 Carrier-Phase Ambiguity Resolution. Carrier-phase ambiguity resolution is the process of selecting the correct integer value for the phase ambiguity. It is not always possible to perform ambiguity resolution, and sometimes the wrong integer is chosen, producing erroneous results. Ambiguity resolution generally consists of two primary operations [27]. The first is to create the ambiguity search space by the generation of candidate ambiguity sets. The second operation is the selection of the correct ambiguity set. The next two sections cover the algorithms used in this research.

2.5.8.1 Ambiguity Set Generation. Ambiguity set generation can be characterized by being either a position-domain, measurement-domain, or ambiguity-centered approach. This section provides an overview of the Least squares AMbiguity Decorrelation Adjustment (LAMBDA) developed by Teunissen [31] and the Fast Ambiguity Search Filter developed by Chen and Lapachelle [4]

LAMBDA is not a set generation technique, but rather a search space transformation technique. The ambiguity estimates of the floating-point solution contain a high degree of correlation, which makes ambiguity resolution difficult. LAMBDA reduces the correlation of the ambiguity estimates to enable a fast and efficient search [31]. Teunissen referred to the ambiguity transformation process as a "Z-transformation", not to be confused with the Z transformation of discrete time signal processing. The LAMBDA method preserves the volume of the search space while also maintaining the integer nature of the ambiguities. The Z-Transform is defined as:

$$\mathbf{z} = \mathbf{Z}^T\mathbf{x} \qquad \hat{\mathbf{z}} = \mathbf{Z}^T\hat{\mathbf{x}} \qquad \mathbf{Q}_{\hat{\mathbf{z}}} = \mathbf{Z}^T\mathbf{Q}_{\hat{\mathbf{x}}}\mathbf{Z} \tag{2.60}$$

where

$$\mathbf{x}, \mathbf{z} = \text{untransformed and transformed ambiguities, respectively}$$

$$\hat{\mathbf{x}}, \hat{\mathbf{z}} = \text{untransformed and transformed ambiguity estimates, respectively}$$

$$\mathbf{Z} = \text{Z-Transformation matrix}$$

$$\mathbf{Q}_{\hat{\mathbf{x}}}, \mathbf{Q}_{\hat{z}} = \text{untransformed and transformed covariance matrix, respectively}$$

The transformation technique can be constructed for the simple two-dimensional case, starting with the untransformed covariance ambiguity covariance matrix given by

$$\mathbf{Q}_{\hat{\mathbf{x}}} = \begin{bmatrix} \sigma_1^2 & \sigma_{12} \\ \sigma_{21} & \sigma_2^2 \end{bmatrix} \tag{2.61}$$

In this case, the Z-Transformation matrices can be defined as

$$\mathbf{Z}_1^T = \begin{bmatrix} 1 & \text{int}(-\sigma_{12}\sigma_2^{-2}) \\ 0 & 1 \end{bmatrix} \tag{2.62}$$

or alternatively

$$\mathbf{Z}_2^T = \begin{bmatrix} 1 & 0 \\ \text{int}(-\sigma_{21}\sigma_1^{-2}) & 1 \end{bmatrix} \tag{2.63}$$

where either the upper ($\mathbf{Z}_1^T$) or lower ($\mathbf{Z}_2^T$) diagonal form can be used. The rounding of the off-diagonal terms (denoted by "int") to integers is necessary to maintain the integer nature of the ambiguities.

Rizos and Han [29] developed an efficient method for high-order Z-transformations. The first step is to perform an upper triangular factorization of the ambiguity co-

variance matrix by:

$$\mathbf{Q}_{\hat{\mathrm{x}}} = \mathbf{U}_1 \mathbf{D}_{U_1} \mathbf{U}_1^T \tag{2.64}$$

where $\mathbf{U}_1$ is an upper triangular matrix and $\mathbf{D}_{U_1}$ is a diagonal matrix.

In the next step an intermediate transformation matrix is computed by first rounding the elements of $\mathbf{U}_1$ to integer values and then taking the inverse.

$$\mathbf{Z}_{U_1} = ([\mathbf{U}_1]_{\mathrm{int}})^{-1} \tag{2.65}$$

An intermediate covariance matrix ($\mathbf{Q}_{\hat{\mathrm{Z}}_{U_1}}$) uses the intermediate transformation matrix ($\mathbf{Z}_{U_1}$) by

$$\mathbf{Q}_{\hat{\mathrm{Z}}_{U_1}} = \mathbf{Z}_{U_1} \mathbf{Q}_{\hat{\mathrm{x}}} \mathbf{Z}_{U_1}^T \tag{2.66}$$

This process is repeated again, except with a lower triangular factorization given by

$$\mathbf{Q}_{\hat{\mathrm{Z}}_{L_1}} = \mathbf{L}_1 \mathbf{D}_{L_1} \mathbf{L}_1^T \tag{2.67}$$

where $\mathbf{L}_1$ is a lower triangular matrix and $\mathbf{D}_{L_1}$ is a diagonal matrix.

Again the matrix is first rounded and then the inverse is taken.

$$\mathbf{Z}_{L_1} = ([\mathbf{L}_1]_{\mathrm{int}})^{-1} \tag{2.68}$$

The intermediate covariance is calculated by:

$$\mathbf{Q}_{\hat{\mathrm{Z}}_{L_1}} = \mathbf{Z}_{L_1} \mathbf{Q}_{\hat{\mathrm{Z}}_{U_1}} \mathbf{Z}_{L_1}^T \tag{2.69}$$

The process is repeated until Equations 2.65 and 2.68 result in identity matrices. The Z-transformation is then given by

$$\mathbf{Z} = \mathbf{Z}_{L_{\mathrm{k}-1}} \mathbf{Z}_{U_{\mathrm{k}-1}} ... \mathbf{Z}_{L_2} \mathbf{Z}_{U_2} \mathbf{Z}_{L_1} \mathbf{Z}_{U_1} \tag{2.70}$$

Because the LAMBDA method does not actually generate an ambiguity search space, other ambiguity resolution techniques are used on the transformed estimates and resulting covariances. The Fast Ambiguity Search Filter (FASF) is the method used in this thesis.

The FASF method was developed by Chen and Lachapelle [4] as an efficient approach for ambiguity resolution. FASF operates recursively and takes advantage of the related nature of ambiguity ranges. Along with the ambiguity state and covariance, FASF requires the constant k to be given to define the search space for the ambiguity $\nabla\Delta N_{\text{int}}$ by

$$\hat{\mathrm{x}}_n - k\sigma_n \leq \nabla\Delta N_{\text{int}} \leq \hat{\mathrm{x}}_n + k\sigma_n \tag{2.71}$$

with $\hat{\mathrm{x}}_n$ and σ_n representing the floating-point estimate and standard deviation of the nth ambiguity. Conditional ambiguity estimates and their associated covariances are determined with the condition that the first ambiguity is correct. The process is recursive with each new ambiguity calculated in the same manner [4]. The new conditional state estimate and covariance are defined by:

$$\tilde{\mathbf{x}} = \hat{\mathbf{x}} - \mathbf{p}_n(x_n - \nabla\Delta N_{\text{int}})/\sigma_n^2 \tag{2.72}$$

$$\mathbf{P}_{\tilde{x}} = \mathbf{P}_{\hat{x}} - (\mathbf{p}_n\mathbf{p}_n^T)/\sigma_n^2 \tag{2.73}$$

where

$\hat{\mathbf{x}}$ = unconditioned estimated parameter vector

$\mathbf{P}_{\hat{x}}$ = unconditioned estimated parameter covariance matrix

$\tilde{\mathbf{x}}$ = estimated parameter vector conditioned on $\hat{x}_n = \nabla\Delta N_{\text{int}}$

$\mathbf{P}_{\tilde{x}}$ = covariance matrix conditioned on $\hat{x}_n = \nabla\Delta N_{\text{int}}$

$\mathbf{p}_n$ = nth column of the covariance matrix $P_{\hat{x}}$

σ_n^2 = scalar variance of the nth parameter (taken from the diagonal of $\mathbf{P}\hat{x}$)

FASF can be performed in either the normal or Z-transformed domain. If FASF is performed in the Z-transform domain (as done in this thesis research), it must be transformed back into the original ambiguity domain.

2.5.8.2 Ambiguity Set Determination. Ambiguity set determination is the second operation in the ambiguity resolution process. A common technique used in set discrimination is the use of a ratio test using a sum of squared residuals. The correct set of ambiguities typically has the smallest residuals. By comparing the sum of squared residuals the correct set generally stands out. This techniques can be further broken down into two methods based on how the residuals are formed.

The first method is to define a residual as the difference between the floating-point ambiguity state estimate and each candidate set [24]. When this approach is used, the weighted sum of squared residuals is expressed by:

$$\Omega_i = (\hat{\mathbf{x}}_{float} - \bar{\mathbf{x}}_i)^T \mathbf{P}^{-1}_{\hat{\mathbf{x}}_{float}} (\hat{\mathbf{x}}_{float} - \bar{\mathbf{x}}_i) \tag{2.74}$$

where $\bar{\mathbf{x}}_i$ is the ith candidate integer ambiguity vector and Ω_i is the sum of squared residuals for the ith candidate ambiguity vector. This is the method used in this research.

The second method involves defining residuals based on the difference between the measurement and measurement prediction such as

$$\mathbf{r}_i = \mathbf{z}_i - \mathbf{h}[\mathbf{x}(t_i); t_i] \tag{2.75}$$

This requires that a filter operates on each candidate ambiguity set to determine the best fit for discrimination. The sum of squared residuals for this convention is given as

$$\Omega_i = \mathbf{r}^T \mathbf{A}^{-1} \mathbf{r} \tag{2.76}$$

where $\mathbf{r}$ is a residual based on equation (2.75), and $\mathbf{A}$ is defined to be the measurement covariance [24].

The ratio test can be applied to either residual convention by comparing the magnitude of the best (smallest) and second best (second smallest) sum of squared residual terms by

$$\text{ratio} = \frac{\Omega_i(2^{nd}best)}{\Omega_i(best)} \tag{2.77}$$

The ambiguity set corresponding to the one selected as best is determined to be the correct one if the ratio is consistently large (typically, greater than 2).

2.6 Pseudolites

The term pseudolite is short for "pseudo-satellite", refering to ground-based GPS-like transmitters. Pseudolites have the flexibility to vary the location, power, and frequency of the transmitter. Pseudolites also are able to provide signals for navigation purposes in adverse environments such as open-pit mining, where GPS signals are often block by the steep sides of the pit. Many of the assumptions that are made with GPS navigation cannot be applied to pseudolites, as will be seen. This section begins with a discussion of differences between GPS and pseudolite navigation, then presents typical pseudolite applications, and ends with descriptions of the problems and sources of error in pseudolite measurements.

2.6.1 GPS-Pseudolite Differences. Many of the assumptions that are used in GPS processing cannot be made for pseudolite navigation. These include:

- The expected ranges for pseudolites are much more dynamic than for GPS operation and will affect receiver power levels
- When a static reference receiver is used, there is not any relative motion between the reference receiver and each pseudolite like there is between a reference receiver and the orbiting GPS satellites. This results in measurement

biases due to pseudolite location errors that do not average out over time. Also the multipath error between pseudolites and the reference receiver will have stronger time correlations than the multipath experienced at the mobile receiver, when in motion.

- Pseudolites do not have to operate at the GPS L1 and L2 frequencies. They also do not have to use the same code sequence or chipping rates that GPS satellites use.
- Due to the short ranges between pseudolite transmitters and receivers the measurement model is more nonlinear than for GPS operation.
- Pseudolites do not have an orbital or ephemeris error, but rather a position error that is dependent on the type of surveying accuracy used to estimate the phase center of the pseudolite antenna.
- A pseudolite signal will not travel through the ionosphere, so any error terms associated with ionospheric delay can be ignored.
- Depending on the relation of the mobile receiver to the reference receiver, single and double differencing will not reduce tropospheric error as much as with GPS. This is similar to extremely long baselines in GPS processing.

2.6.2 Pseudolite Applications. The four categories of pseudolite applications include direct positioning, digital data transmission, carrier-phase ambiguity resolution, and as a differential reference station [7]. Direct positioning using a network of pseudolites is the application addressed in this research.

Pseudolite direct positioning can be accomplished with both the code and carrier-phase measurements in a similar manner as for conventional GPS positioning. The majority of work with pseudolites has been concerned with the augmentation of GPS or GPS/INS. Pseudolites can improve the overall geometry of the augmented system, providing greater positioning accuracy, reliability, availability, continuity, and integrity monitoring [23]. They can also be used as a sole source signal of

navigation. Additionally, GPS signals are typically weak or not present indoors, and pseudolites can be used to provide an indoor navigation source.

Digital data transmission is also possible for pseudolite transmitters. One of the advantages of using a pseudolite for data transmission to a GPS receiver is that only minor changes are needed in the receiver [7]. GPS reference data has frequently been proposed for transmission via pseudolites [10, 30].

Pseudolites can assist and speed up the carrier-phase ambiguity resolution in a GPS system augmented by pseudolites. This is accomplished through the large changes in geometries of the pseudolite signal [23]. An example of this is the Kinematic GPS Landing Systm (KGLS) at Stanford [7].

When a pseudolite rebroadcasts a coherent replica of received GPS signals, it is known as a differential reference station [7]. The difference between the direct and reflected signal can be used for navigation purposes.

2.6.3 Signal Interference and Near-Far Problem. One of the largest issues facing practical pseudolite applications is the signal interference and the associated near-far problem. While the distance from a given receiver to any GPS satellite is relatively constant, the ranges between a pseudolite and its receiver vary greatly. The large dynamic difference in ranges result in large differences in received power levels. This can cause the automatic gain control in a receiver to adjust to the highest powered signal, which effectively jams all other pseudolites.

Pseudolites have both a "near" and a "far" radius that define its usable area. A pseudolite will jam all other pseudolites within its near radius. The far radius is the distance within which a receiver must stay to maintain lock on that pseudolite. The near and far radii are a function of transmission power, so increasing or decreasing power will increase or decrease the near and far radii by the same ratio. The relationship between the near and far radius is given as a ratio that is generally accepted to be 1/10 for practical systems [7], although this can vary depending on the

cross-correlation of the codes. An example of the near-far radii is shown in Figure 2.3.

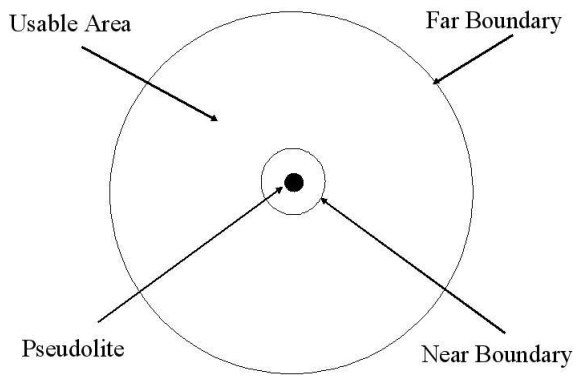

Figure 2.3 Near-Far Problem

The various techniques that have been proposed to reduce the near-far problem can be grouped into three categories—Time Division Multiple Access (TDMA), Frequency Division Multiple Access (FDMA), and Code Division Multiple Access (CDMA).

TDMA can be accomplished through the pulsing of the pseudolites. If pulsed pseudolites are operated at greater than 20-25 percent of a duty cycle, then the GPS signal will be jammed [5]. It has been proposed to operate two pseudolites each pulsing at 10-12.5 percent of the duty cycle to facilitate an integrated GPS/Pseudolite navigation system [5]. This arrangement still only allows the use of two pseudolites if the GPS signal is also desired. If the GPS signal is not of interest, 10 pseudolites could be used (given a 10 percent duty cycle each).

The second technique for interference reduction, FDMA, can be implemented by modifying GPS signals with small frequency offsets. Elrod et. al [11] suggested offsetting the frequency to the first null of the GPS satellite signal in order to reduce cross-correlation with the GPS signal. It resembles a large doppler offset that most receivers can handle.

CDMA has been demonstrated through concatenations of C/A codes. Ndili [23] showed through simulation that a code length of 4092 (4 times that of C/A code) would provide a 6 dB enhancement, and thus double the far radius while maintaining the same near radius. By combining 20 C/A codes for a length of 20460 in addition to operating at a P-code chipping rate would add a 23 dB enhancement. The longer the code length and higher the chipping rate, the larger the near-far ratio.

2.6.4 Sources of Error. Pseudolite error can be broken up into measurement and measurement model errors. Both of these will affect the accuracy of a pseudolite system because the residual term is formed by subtracting the measurement prediction from the measurement as shown by the following equation:

$$\mathbf{r}_i = \mathbf{z}_i - \mathbf{h}[\mathbf{x}(t_i); t_i] \tag{2.78}$$

The next two subsections describe the errors present in pseudolite measurements and measurement models.

2.6.4.1 Pseudolite Measurement Errors. Pseudolite signal errors are reduced less by double differencing than for the analogous GPS equations due to a different geometric configuration [6]. The errors that remain in a pseudolite carrier-phase measurement after a double difference operation are the measurement noise, multipath, and residual tropospheric error (i.e., the error after a tropospheric model has been applied).

The measurement noise associated with pseudolites is determined by the quality of the receiver (just like for a GPS measurement). Along with proper modelling in the navigation filter, improving the receiver design is one of the few ways to reduce the effect of measurement noise.

Multipath can be considered a dominant error source in pseudolite applications [35]. Even after multipath mitigating techniques (such as antenna placement

and chokering antennas) are used in a pseudolite system, the multipath error is generally larger for a pseudolite signal than for a satellite signal [8]. This is due to the relative geometries in the transmitter-receiver setup in a pseudolite network.

Because, unlike satellites, the transmitters do not move relative to the reference receiver, time-invariant or standing multipath is a concern for pseudolite applications. This contributes to a multipath error that is more difficult to handle than the multipath error associated with satellite signals. The navigation filter assumes that all errors sources are white (uncorrelated in time) and the more time-invariant the multipath becomes, the further this assumption is broken. Careful calibration is required to estimate and remove this constant error from the corresponding measurements. The use of carrier-phase measurements and antenna design have been shown to help reduce multipath [35]. Multipath affects code measurements to a higher degree than carrier-phase measurements for both a pseudolite or satellite source. Antenna gain shaping helps to reduce multipath by adjusting the gain in the direction of large reflectors [18, 35].

The residual tropospheric error that exists after a tropospheric model is applied cannot be ignored in precise pseudolite applications. The amount that single and double differencing reduce the effect of tropospheric delay in GPS operation is a function of the baseline difference in the mobile and reference receiver positions. Pseudolite applications are equivalent to a very large baseline for which differencing may reduce, but not significantly remove, tropospheric delay.

2.6.4.2 Pseudolite Measurement Model Errors. Pseudolite measurement model errors include the effect of position errors in the location of the pseudolites and reference receiver in addition to the error due to linear approximations in the measurement model.

The source of errors from the imprecise locations of the pseudolite transmitters and reference receivers are analogous to the ephemeris or orbital errors in GPS

satellite locations. Like tropospheric errors, these position errors are not reduced for pseudolites as much as GPS for single and double differencing.

For outdoor pseudolite applications, static surveying techniques that use carrier-phase DGPS can be used to solve for the positions of the pseudolites to within centimeters. Because GPS is generally not available indoors, this cannot be used to estimate the locations of pseudolite transmitters indoors precisely. Changdon et.al. [2] presented a method to calculate the pseudolite positions using only the user's position information and the pseudolite signals. This is advantageous because the location found was the phase center of the antenna and not just the physical center.

One of the biggest differences between GPS and pseudolite navigation is the typical ranges between transmitters and receivers. GPS signals travel on the order of 20,000 kilometers or more, while pseudolite signal ranges could be measured in meters (depending on signal power). As the ranges in pseudolite navigation become shorter, the signal waveform becomes more spherical than planar. Figure 2.4 depicts this relationship with a planar signal from a GPS satellite and a spherical signal from a pseudolite. In reality a GPS signal is spherical, but the radius is so large that it is essentially planar for a GPS user.

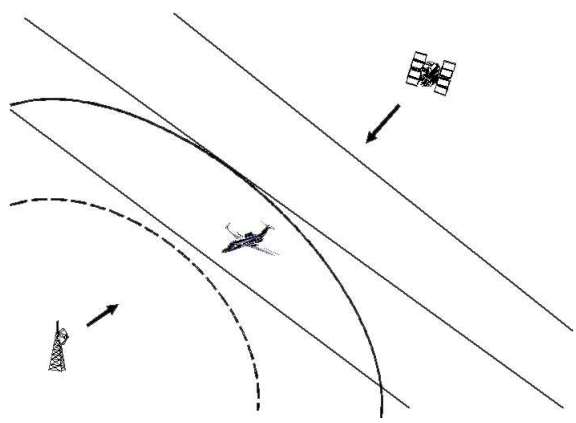

Figure 2.4 Spherical and Planar Wavefronts

The measurement model equation for the extended Kalman filter (EKF) is nonlinear for both GPS and pseudolite navigation. An EKF does a linearization of the nonlinear measurement equation by using a first order Taylor series approximation. As the waveforms become more spherical, the measurement nonlinearity becomes more severe and the first order approximation becomes more inadequate. For GPS signals, the approximation error is small enough to be ignored, but pseudolite navigation is different and requires care in handling the large measurement nonlinearities.

The nonlinearity error can also be explained by graphically. Figure 2.5 shows a spherical waveform at the receiver location. The uncertainty orthogonal to the line-of-sight from transmitter to receiver will only increase the range. This results in the range to be under-estimated. As the waveforms become more spherical, this error becomes more substantial.

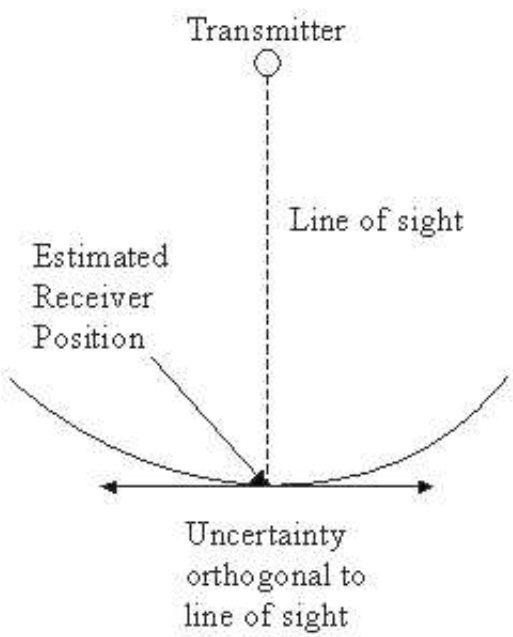

Figure 2.5 Nonlinear Elongation of Range

This problem is not unique to GPS or pseudolite operation. Widnall [**?**] referred to this problem as a nonlinear elongation of measured range. He suggested applying nonlinear filtering techniques to enlarge the region of convergence of a Kalman filter. He stated that, if the nonlinearity is comparable to the measurement error, divergence can occur.

2.7 Summary

This chapter has provided a basic overview of Kalman filter theory including the extended Kalman filters. GPS techniques including carrier-phase differential algorithms were presented. The section on pseudolites described the challenges and issues of pseudolite navigation.

III. Methodology and Algorithm Development

3.1 Overview

This chapter begins with the laying out the simulation design and setup. It then gives a description of the truth model and continues with the generation of the measurement and measurement model errors. Next, the floating-point DGPS filter is described, along with the features of this filter. This chapter ends with a description of the specific carrier-phase ambiguity techniques used in this research.

3.2 Overall Simulation Design

This research involved development of a Kalman filter-based processing algorithm for calculating position and ambiguities for the pseudolite system, as well as simulating a truth model. The truth model was not a traditional truth model, in the traditional Kalman filter performance evaluation sense, in which a low order filter is compared to a higher order truth model. Rather, the truth model represents the true positions of the transmitters and receivers along with the true ambiguities, and simulated errors in the simulated measurements. The purpose of the filter algorithm was to estimate the position of the mobile receiver and the ambiguities in the carrier-phase measurements.

3.3 Truth Model

The first step in the generation of the truth model consisted of selecting the coordinates of the stationary pseudolites and reference receiver. The projected coordinates of the Inverted GPS Range (IGR) were used for this research [16]. The IGR is a GPS modernization field test program which is currently unfunded at the time of this writing. The coordinates reflect realistic pseudolite locations near Holloman AFB, NM. Table 3.1 lists the positions of the pseudolites (numbered 1-10) and ref-

erence receiver while their positions are shown in Figure 3.1 relative to the reference receiver.

Table 3.1 Pseudolite and Reference Receiver Truth Locations

PRN #	Latitude (deg)	Longtitude (deg)	Ellipsoid height (m)
1	33.50321	-106.56055	1433
2	33.54685	-106.43650	1630
3	33.67726	-106.67454	1447
4	33.39548	-106.67449	1541
5	33.66746	-106.43772	1602
6	33.78633	-106.48492	1562
7	33.82624	-106.66540	1574
8	33.64742	-106.56846	1426
9	33.72906	-106.41564	1656
10	33.72990	-106.63744	1442
Ref Rcvr	33.65695	-106.53696	1424

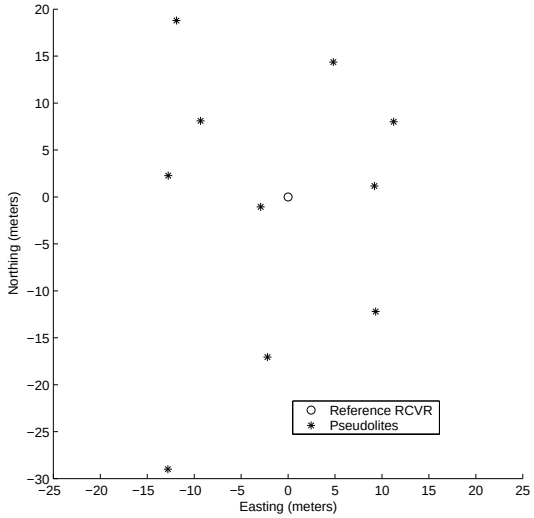

Figure 3.1 Pseudolite and Reference Receiver Relative Positions

The second step in the truth model generation was the selection of a realistic flight trajectory. The flight trajectory used for this research came from actual flight test data collected from a C-21 operated by the 746th Test Squadron at Holloman AFB. The simulation is constructed so only the positions, i.e. no velocities or accelerations, of the mobile receiver are required to run additional flight scenarios. CHAPS is normally flown on a C-21 from Holloman AFB, NM, so the flight trajectory used in this research is realistic of a typical reference system flight. The three-dimensional view of the trajectory with projections unto each axis is plotted in Figure 3.2.

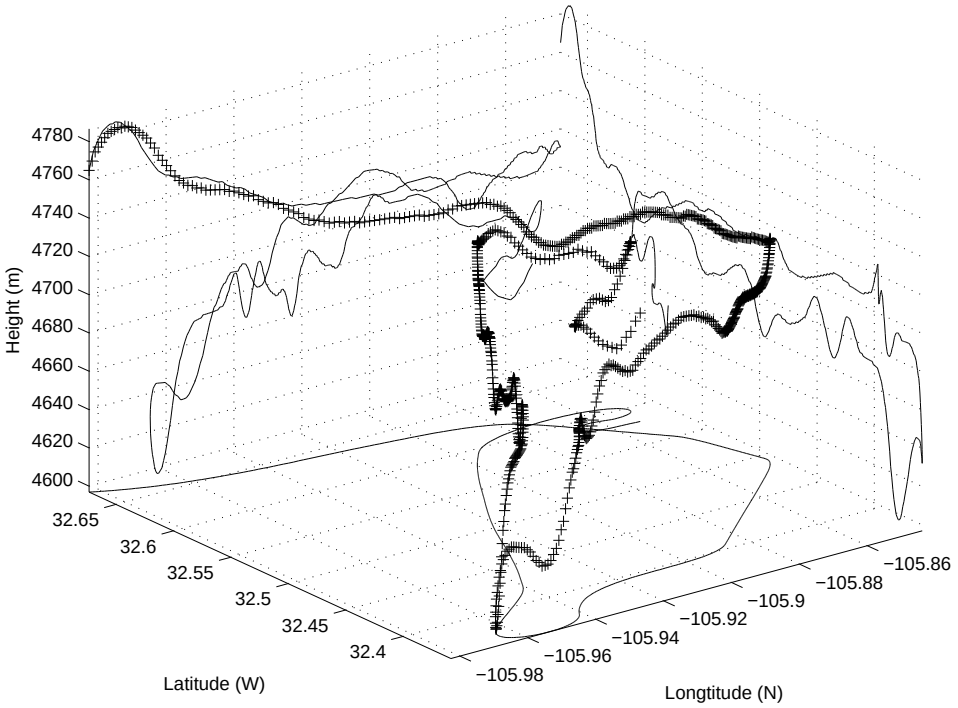

Figure 3.2 3-Dimensional View of Trajectory With Projections

Although the flight trajectory and the coordinates of the pseudolites and reference receiver are located near Holloman AFB, New Mexico, they are not co-located. The coordinates of the pseudolites and reference receiver were adjusted to within range of the mobile receiver flight trajectory. This was accomplished by first converting them from the LLH frame to an ECEF frame, shifting them in a local level

frame, and finally converting back to ECEF. This arrangement was necessary to maintain the exact relative arrangement of the pseudolite network.

3.4 Measurement and Measurement Model Error Generation

Section 2.5.6 developed the double-differenced code and carrier-phase measurement equations for GPS applications. Those equations require adaptation for use with pseudolite measurements. The ionospheric error terms can be removed because pseudolite signals will not travel through the ionosphere. The resulting equations for pseudolite applications are

$$\Delta\nabla\rho_{AB}^{kj} = \Delta\nabla r_{AB}^{kj} + \Delta\nabla T_{AB}^{kj} + \Delta\nabla m_{\rho AB}^{kj} + \Delta\nabla v_{\rho AB}^{kj} \tag{3.1}$$

for the code and

$$\Delta\nabla\phi_{AB}^{kj} = \lambda^{-1}(\Delta\nabla r_{AB}^{kj} + \Delta\nabla T_{AB}^{kj} + \Delta\nabla m_{\phi AB}^{kj} + \Delta\nabla v_{\phi AB}^{kj}) + \Delta\nabla N_{AB}^{kj} \tag{3.2}$$

for the carrier-phase. GPS navigation is affected by errors in the predicted motion of the satellites, commonly referred to as ephemeris or orbital errors. This error is not present in the signal itself, but occurs when the receiver uses the imprecise satellite locations for range calculations. Pseudolites have a corresponding error that is due to the imprecise estimates of the reference receiver and pseudolite locations. These pseudolite and reference receiver position errors, along with the measurement noise, multipath, and tropospheric delay errors terms were simulated in this research.

The following sections describe the process of generating the measurement and measurement model errors used in this research. First the pseudolite position errors are described, followed by the descriptions of measurement noise, multipath, and tropospheric delay. Measurement noise, multipath, and tropospheric delay error were added to the true ranges. The pseudolite and reference receiver position errors were added to the true positions, and those positions were used in the filter. The

figures in each section show plots for code and carrier-phase errors for ten pseudolites for every epoch in the simulation. These plots show the relative magnitudes and time correlations for each error source. After the errors were added to the true ranges, but before a data file was created with the code and carrier-phase measurements, a maximum range limitation was implemented. The maximum range feature simulated a pseudolite that was out of signal range from the mobile receiver. Pseudolite prn 4 was 31,698 meters from the reference receiver, so the maximum range was typically set higher than that at 32,000 meters. This resulted in 7-10 satellites visible for the mobile receiver.

3.4.1 Pseudolite and Reference Receiver Position Errors. The imprecise estimated positions of the pseudolites and reference receiver affect the code and carrier-phase measurement by the same magnitude. The location errors of the pseudolites and reference receiver were modeled as biases with a zero-mean Gaussian distribution. Errors were created in an East-North-Up reference frame with independent horizontal and vertical components which were added to the true positions. The horizontal standard deviation was set to 1 cm and the vertical was set to 2 cm to represent the expected accuracies of precision surveying.

The errors due to inaccurate positions of the pseudolites and reference receiver were not added to the true range, but instead used by the filer in the measurement prediction calculation. Figure 3.3 shows the equivalent effect of the position errors on the ranges to the mobile and reference receiver. The ranges calculated at the mobile receiver include only the effect of position errors at the pseudolites while the ranges calculated at the reference receiver include both the position errors of the pseudolites and the errors of the reference receiver itself.

The ten lines shown on Figure 3.3, one for each visible pseudolite, denote the range error. The lines for the reference receiver range errors are constants because the positions errors are constant during a simulation run.

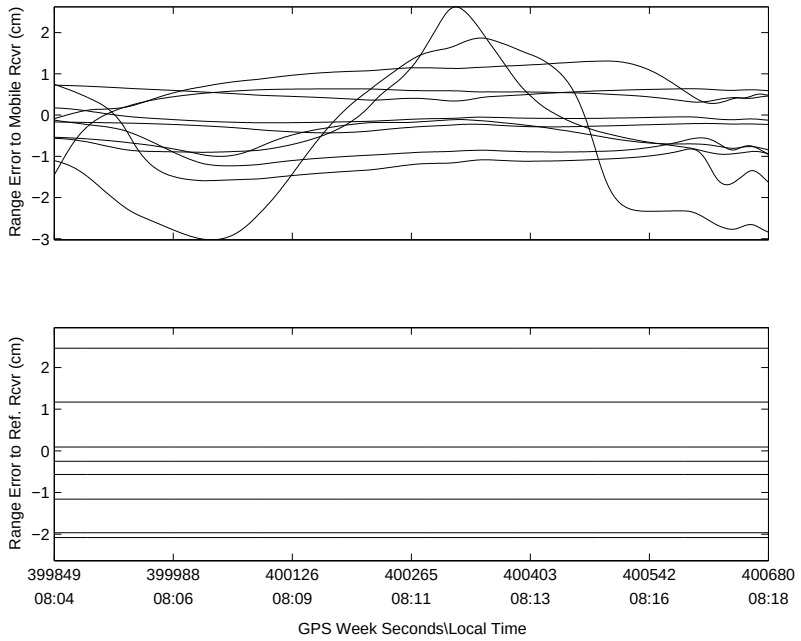

Figure 3.3 Position Error Effect on Ranges

3.4.2 Measurement Noise. The measurement noise was modeled as zero-mean white Gaussian noise. Measurement noise is considerably smaller for carrier-phase measurements than for code measurements, and it was modeled with a 55 cm standard deviation for the code versus a 3.5 mm standard deviation for the carrier-phase [28]. The measurement noise was modeled as uncorrelated between the mobile and reference receiver.

3.4.3 Multipath. The multipath that exists in a pseudolite system is caused by the environment at the location of the transmitters and receivers [8, 12]. The reference receiver can experience more time-invariant multipath than the mobile receiver because there isn't any relative movement between the reference receiver and the pseudolites . These pseudolite phenomena can be reduced with a Multipath-Limiting-Antenna on both the transmitters and receivers [8]. For the purposes of this research, the multipath for the received signal at the reference receiver was modeled with longer time correlations than the multipath for the mobile receiver.

The multipath was generated as a first order Gauss Markov process driven with the parameters σ and τ, which are themselves modeled as first order gauss Markov processes (shown below as FOGM(σ, τ). A minimum threshold was set for the σ and τ values. The code multipath was generated as 1.5 times the summation of source 1 and source 2, to accurately model multipath error. These equations can be summarized by

$$\text{multipath} = \text{FOGM}(\sigma, \tau) \tag{3.3}$$

$$\sigma = \sigma_0 + \text{FOGM}(\sigma_\sigma, \tau_\sigma) \tag{3.4}$$

$$\tau = \tau_0 + \text{FOGM}(\tau_\tau, \tau_\tau) \tag{3.5}$$

$$\sigma \geq \sigma_{\text{min}} \tag{3.6}$$

$$\tau \geq \tau_{\text{min}} \tag{3.7}$$

The values used for the mobile receiver multipath are listed in Table 3.2 are taken from.

Table 3.2 Multipath Parameter Values

Parameter	Mob Code (Source 1)	Mob Code (Source 2)	Mobile Phase	Ref Code (Source 1)	Ref Code (Source 2)	Reference Phase
σ_0 (cm)	10.0	20.0	0.19	10.0	20.0	0.19
τ_0 (sec)	500	25	1000	500	25	1000
σ_σ (cm)	4.0	0.1	0.038	4.0	0.1	0.038
τ_σ (sec)	2000	2000	1500	2000	2000	1500
σ_τ (sec)	200	2	400	200	2	400
τ_τ (sec)	2000	2000	2000	2000	2000	2000
σ_{min} (cm)	5.0	1.0	0.019	5.0	1.0	0.019
τ_{min} (sec)	100	1	0.019	100	1	0.019

The parameters for the reference receiver multipath were the same for the mobile receiver except that the time constants were tripled to simulate stronger time correlations. Figure 3.4 depicts a typical run for mobile receiver multipath error, while Figure 3.5 depicts the reference receiver multipath. Both plots show the code multipath on the top subplot and the carrier-phase multipath on the bottom subplot.

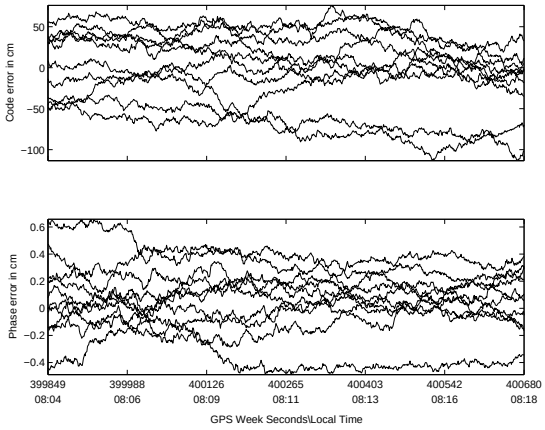

Figure 3.4 Typical Mobile Receiver Multipath Error for All Ten Pseudolites

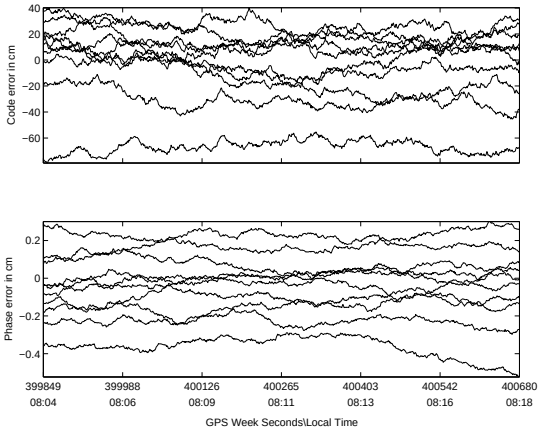

Figure 3.5 Typical Reference Receiver Multipath Error for All Ten Pseudolites

By comparing Figures 3.5 and 3.4 it is clear that the multipath simulated at the reference receiver had strong time correlations between epochs. Recall that this

was the purpose of tripling the time constants for the reference receiver tropospheric truth model.

3.4.4 Tropospheric Delay. The truth model for generating the tropospheric delay was taken from reference [3, 33] which was a function of temperature, atmospheric pressure, relative humidity, elevation angle, and range. The atmospheric parameters are the ones taken at the reference receiver. The tropospheric delay calculation for the mobile receiver is defined as

$$\tau_{APL,u}(R_u, \Delta h_u) = \frac{\Delta\tau_{v,dry} + \Delta\tau_{v,wet}}{\sin(el_u)} = \frac{(\Delta\tau_{v,dry} + \Delta\tau_{v,wet})}{\Delta h_u} R_u$$
$$= \frac{77.6 P_s \times (42700 - h_s) \times 10^{-6}}{5 T_s \Delta h_u} \left[\left(1 - \frac{\Delta h_{APL}}{42700 - h_s}\right)^5 - \left(1 - \frac{\Delta h_{APL} + \Delta h_u}{42700 - h_s}\right)^5 \right] R_u$$
$$+ \frac{N_s \times (13000 - h_s) \times 10^{-6}}{5 \Delta h_u} \left[\left(1 - \frac{\Delta h_{APL}}{13000 - h_s}\right)^5 - \left(1 - \frac{\Delta h_{APL} + \Delta h_u}{13000 - h_s}\right)^5 \right] R_u \tag{3.8}$$

where the variables are defined as

$\tau_{APL,u}$ = tropospheric delay for mobile receiver (meters)
R_u = slant range between the pseudolite and user (meters)
Δh_u = the height of the user above the pseudolite (meters)
$\Delta\tau_{v,dry}$ = differential vertical dry delay (meters)
$\Delta\tau_{v,wet}$ = differential vertical wet delay (meters)
el_u = elevation angle in radians
Δh_{APL} = difference in height between pseudolites and reference receiver
h_s = height of reference receiver
P_s = surface pressure (millibars)
T_s = surface temperature (Kelvins)
N_s = surface refractivity

Equation 3.8 is adapted for reference receiver tropospheric delay calculation and given by

$$\tau_{APL,R}(R_R, \Delta h_R) = \frac{77.6P_s \times (42700 - h_s) \times 10^{-6}}{5T_s \Delta h_{APL}} \left[1 - \left(1 - \frac{\Delta h_{APL}}{42700 - h_s}\right)^5\right] R_R + \frac{N_s \times (13000 - h_s) \times 10^{-6}}{5\Delta h_{APL}} \left[1 - \left(1 - \frac{\Delta h_{APL}}{13000 - h_s}\right)^5\right] R_R \quad (3.9)$$

Both Equations 3.8 and 3.9 are valid for positive and negative elevation angles but indeterminate for zero elevation angles [3, 33]. The reference did develop equations for zero elevation angles, but they were not implemented in this research, because the placement of the reference receivers and mobile receiver trajectory did not result in zero elevation angles.

3.5 Floating-Point Differential Pseudolite Kalman Filter

The floating-point differential pseudolite Kalman filter used in this research is a post-processed algorithm. It is a modified version of the filter developed in reference [27], which is adapted for pseudolite navigation. The double-difference operation is applied to both the code and carrier-phase measurements, allowing the removal of the states modelling clock error. This section presents the baseline filter development, and the modifications are presented in the next section. The baseline filter calculates position, velocity, acceleration, and carrier-phase ambiguity estimates for the mobile receiver. The objective of the filter is to produce carrier-phase ambiguity estimates and associated covariances that will be processed through ambiguity resolution techniques to produce the fixed-integer results.

Before the filter is run on the data, a pre-processing step is conducted to determine the number of visible pseudolites, a vector of visible pseudolite prns, the base pseudolite for double-difference operation, and the non-base pseudolite prns for each epoch data.

3.5.1 Differential Pseudolite Model Equations. A First Order Gauss Markov Acceleration (FOGMA) model was used to define the three positions, three velocities, and three accelerations states of the floating-point differential pseudolite Kalman filter. The remaining states consisted of $(n-1)$ carrier-phase ambiguity states, where n is the number of pseudolites in view at that epoch.

The positions, given in the ECEF coordinate frame, are modeled as the time derivatives of the velocities, and the velocities are modeled as the time derivatives of the accelerations by:

$$\begin{aligned} \dot{x}_1 &= x_4 & \dot{x}_4 &= x_7 \\ \dot{x}_2 &= x_5 & \dot{x}_5 &= x_8 \\ \dot{x}_3 &= x_6 & \dot{x}_6 &= x_9 \end{aligned} \tag{3.10}$$

The position and velocity states are completely determined by other states, and they do no include any direct driving noise. The acceleration states are modeled as first-order Gauss-Markov processes by

$$\begin{aligned} \dot{x}_7 &= (-1/T_a)x_7 + w_{a_1}(t) \\ \dot{x}_8 &= (-1/T_a)x_8 + w_{a_2}(t) \\ \dot{x}_9 &= (-1/T_a)x_9 + w_{a_3}(t) \end{aligned} \tag{3.11}$$

with associated dynamic driving noise processes given by

$$\begin{aligned} E\left\{w_{a_1}(t)w_{a_1}(t+\tau)\right\} &= E\left\{w_{a_2}(t)w_{a_2}(t+\tau)\right\} = E\left\{w_{a_3}(t)w_{a_3}(t+\tau)\right\} \\ &= \frac{2\sigma_a^2}{T_a}\delta(\tau) = q_a\delta(\tau) \end{aligned} \tag{3.12}$$

The correlation time, T_a, and variance (or mean square value), σ_a^2, for the accelerations are determined based on the anticipated acceleration maneuvers and time

correlations. The value T_a was set to 3 seconds to account for relatively short acceleration maneuvers in a C-12, and σ_a was set to 15 m/s^2 to handle the "worst case" acceleration. With these values q_a is calculated to be 150 m^2/sec^5.

The floating-point filter can accept either a single or widelane frequency. In either case, the double difference is performed with the ambiguity terms still maintaining an integer nature. The ambiguities were modeled as random walks rather than constant biases to ensure that, if the filter converged to an incorrect value, it could correct itself (i.e., the gain of the . The cycle ambiguities were modeled in an additional $(n-1)$ states after the initial 9 states for position, velocity, and acceleration. The double-differenced carrier-phase ambiguities are defined by:

$$\begin{aligned}
\dot{x}_{10} &= w_{\nabla\Delta N^{1-2}} \\
\dot{x}_{11} &= w_{\nabla\Delta N^{1-3}} \\
&\vdots \\
\dot{x}_{(8+n)} &= w_{\nabla\Delta N^{1-n}}
\end{aligned} \tag{3.13}$$

where PRN 1 is given as the base and n represents the total number of pseudolites visible.

The process noise is given as

$$\begin{aligned}
E\{w_{\nabla\Delta N^{bi}}(t) w_{\nabla\Delta N^{bi}}(t+\tau)\} &= q_N \delta(\tau) \\
q_N &= 1.1 \times 10^{-5} (\text{cycles}^2/\,\text{sec})
\end{aligned}$$

The value of q_N will yield an increase of approximately 0.2 cycles in the ambiguity standard deviation over a 1 hour period [27]. This will allow the filter to correct itself if it converged to the incorrect value.

The state vector for the floating-point Kalman filter is defined as

$$\mathbf{x} = \left[\mathbf{X}\ \mathbf{Y}\ \mathbf{Z}\ \dot{\mathbf{X}}\ \dot{\mathbf{Y}}\ \dot{\mathbf{Z}}\ \ddot{\mathbf{X}}\ \dot{\mathbf{Y}}\ \ddot{\mathbf{Z}}\ \nabla\boldsymbol{\Delta}\mathbf{N}^{\mathbf{1-2}}\ \ldots\ \nabla\boldsymbol{\Delta}\mathbf{N}^{\mathbf{1-n}}\right]^{\mathbf{T}} \tag{3.14}$$

where

$x_1 = X =$ ECEF X position (m)

$x_2 = Y =$ ECEF Y position (m)

$x_3 = Z =$ ECEF Z position (m)

$x_4 = \dot{X} =$ ECEF X velocity (m/s)

$x_5 = \dot{Y} =$ ECEF Y velocity (m/s)

$x_6 = \dot{Z} =$ ECEF Z velocity (m/s)

$x_7 = \ddot{X} =$ ECEF X acceleration (m/s^2)

$x_8 = \dot{Y} =$ ECEF Y acceleration (m/s^2)

$x_9 = \ddot{Z} =$ ECEF Z acceleration (m/s^2)

$x_{10} = \nabla\Delta N^{1-2} =$ double-differenced phase ambiguity (cycles)

$x_{11} = \nabla\Delta N^{1-3} =$ double-differenced phase ambiguity (cycles)

$\vdots$

$x_{9+(\mathrm{n}-1)} = \nabla\Delta N^{1-n} =$ double-differenced phase ambiguity (cycles)

The differential equation is similar to Equation 2.1 and is represented by

$$\dot{\mathbf{x}}(t) = \mathbf{F}(t)x(t) + \mathbf{G}(t)w(t) \tag{3.15}$$

which expands to:

$$
\begin{bmatrix} \dot{x}_1 \\ \dot{x}_2 \\ \dot{x}_3 \\ \dot{x}_4 \\ \dot{x}_5 \\ \dot{x}_6 \\ \dot{x}_7 \\ \dot{x}_8 \\ \dot{x}_9 \\ \dot{x}_{10} \\ \dot{x}_{11} \\ \vdots \\ \dot{x}_n \end{bmatrix}
=
\begin{bmatrix}
0 & 0 & 0 & 1 & 0 & 0 & 0 & 0 & 0 & 0 & 0 & \cdots & 0 \\
0 & 0 & 0 & 0 & 1 & 0 & 0 & 0 & 0 & 0 & 0 & \cdots & 0 \\
0 & 0 & 0 & 0 & 0 & 1 & 0 & 0 & 0 & 0 & 0 & \cdots & 0 \\
0 & 0 & 0 & 0 & 0 & 0 & 1 & 0 & 0 & 0 & 0 & \cdots & 0 \\
0 & 0 & 0 & 0 & 0 & 0 & 0 & 1 & 0 & 0 & 0 & \cdots & 0 \\
0 & 0 & 0 & 0 & 0 & 0 & 0 & 0 & 1 & 0 & 0 & \cdots & 0 \\
0 & 0 & 0 & 0 & 0 & 0 & -1/T_a & 0 & 0 & 0 & 0 & \cdots & 0 \\
0 & 0 & 0 & 0 & 0 & 0 & 0 & -1/T_a & 0 & 0 & 0 & \cdots & 0 \\
0 & 0 & 0 & 0 & 0 & 0 & 0 & 0 & -1/T_a & 0 & 0 & \cdots & 0 \\
0 & 0 & 0 & 0 & 0 & 0 & 0 & 0 & 0 & 0 & 0 & \cdots & 0 \\
0 & 0 & 0 & 0 & 0 & 0 & 0 & 0 & 0 & 0 & 0 & \cdots & 0 \\
\vdots & \vdots & \vdots & \vdots & \vdots & \vdots & \vdots & \vdots & \vdots & \vdots & \vdots & \ddots & 0 \\
0 & 0 & 0 & 0 & 0 & 0 & 0 & 0 & 0 & 0 & 0 & 0 & 0
\end{bmatrix}
\begin{bmatrix} x_1 \\ x_2 \\ x_3 \\ x_4 \\ x_5 \\ x_6 \\ x_7 \\ x_8 \\ x_9 \\ x_{10} \\ x_{11} \\ \vdots \\ x_n \end{bmatrix}
+
\begin{bmatrix} 0 \\ 0 \\ 0 \\ 0 \\ 0 \\ 0 \\ w_{a1} \\ w_{a2} \\ w_{a3} \\ w_{\nabla\Delta N^{bi}} \\ w_{\nabla\Delta N^{bi}} \\ \vdots \\ w_{\nabla\Delta N^{bi}} \end{bmatrix}
\tag{3.16}
$$

In Equation 3.16, the variable T_a represents the FOGMA acceleration time constant. The $\mathbf{G}(t)$ matrix is defined to be an identity matrix for this research. The dynamics driving noise $\mathbf{Q}$ is defined by:

$$
\mathbf{E}\{\mathbf{w}(t)\mathbf{w}^T(t+\tau)\} = \mathbf{Q}(t)\delta(\tau) \tag{3.17}
$$

The matrix $\mathbf{Q}$ is represented by:

$$\mathbf{Q} = \begin{bmatrix} 0 & 0 & 0 & 0 & 0 & 0 & 0 & 0 & 0 & 0 & 0 & \cdots & 0 \\ 0 & 0 & 0 & 0 & 0 & 0 & 0 & 0 & 0 & 0 & 0 & \cdots & 0 \\ 0 & 0 & 0 & 0 & 0 & 0 & 0 & 0 & 0 & 0 & 0 & \cdots & 0 \\ 0 & 0 & 0 & 0 & 0 & 0 & 0 & 0 & 0 & 0 & 0 & \cdots & 0 \\ 0 & 0 & 0 & 0 & 0 & 0 & 0 & 0 & 0 & 0 & 0 & \cdots & 0 \\ 0 & 0 & 0 & 0 & 0 & 0 & 0 & 0 & 0 & 0 & 0 & \cdots & 0 \\ 0 & 0 & 0 & 0 & 0 & 0 & q_a & 0 & 0 & 0 & 0 & \cdots & 0 \\ 0 & 0 & 0 & 0 & 0 & 0 & 0 & q_a & 0 & 0 & 0 & \cdots & 0 \\ 0 & 0 & 0 & 0 & 0 & 0 & 0 & 0 & q_a & 0 & 0 & \cdots & 0 \\ 0 & 0 & 0 & 0 & 0 & 0 & 0 & 0 & 0 & q_N & 0 & \cdots & 0 \\ 0 & 0 & 0 & 0 & 0 & 0 & 0 & 0 & 0 & 0 & q_N & \cdots & 0 \\ \vdots & \vdots & \vdots & \vdots & \vdots & \vdots & \vdots & \vdots & \vdots & \vdots & \vdots & \ddots & 0 \\ 0 & 0 & 0 & 0 & 0 & 0 & 0 & 0 & 0 & 0 & 0 & 0 & q_N \end{bmatrix} \tag{3.18}$$

The acceleration mean squared value, time constant, and acceleration noise, and the phase ambiguity noise values, which were previously justified, are summarized in Table 3.3.

Table 3.3 Floating-Point Filter Dynamics Driving Noise Values

Term	**Definition**	**Value**
σ_a^2	Mean squared value	$(12.25\ m/sec^2)^2$
T_a	Acceleration time constant	$3\ seconds$
q_a	Acceleration noise	$100\ m^2/sec^5$
q_N	Phase ambiguity noise	$1.1 \times 10^{-4}\ cycles^2/sec$

The initial conditions for the position states were set to the true value at the first epoch with an additive zero-mean error term that had a Gaussian distribution and a standard deviation of 5 meters. The velocity and acceleration initializations

were set to zero with the covariance initialization matrix defined by:

$$\mathbf{P}(t_0) = \begin{bmatrix} \sigma_x^2 & 0 & 0 & 0 & 0 & 0 & 0 & 0 & 0 & 0 & 0 & \dots & 0 \\ 0 & \sigma_y^2 & 0 & 0 & 0 & 0 & 0 & 0 & 0 & 0 & 0 & \dots & 0 \\ 0 & 0 & \sigma_z^2 & 0 & 0 & 0 & 0 & 0 & 0 & 0 & 0 & \dots & 0 \\ 0 & 0 & 0 & \sigma_{\dot{x}}^2 & 0 & 0 & 0 & 0 & 0 & 0 & 0 & \dots & 0 \\ 0 & 0 & 0 & 0 & \sigma_{\dot{y}}^2 & 0 & 0 & 0 & 0 & 0 & 0 & \dots & 0 \\ 0 & 0 & 0 & 0 & 0 & \sigma_{\dot{z}}^2 & 0 & 0 & 0 & 0 & 0 & \dots & 0 \\ 0 & 0 & 0 & 0 & 0 & 0 & \sigma_{\ddot{x}}^2 & 0 & 0 & 0 & 0 & \dots & 0 \\ 0 & 0 & 0 & 0 & 0 & 0 & 0 & \sigma_{\ddot{y}}^2 & 0 & 0 & 0 & \dots & 0 \\ 0 & 0 & 0 & 0 & 0 & 0 & 0 & 0 & \sigma_{\ddot{z}}^2 & 0 & 0 & \dots & 0 \\ 0 & 0 & 0 & 0 & 0 & 0 & 0 & 0 & 0 & \sigma_{\nabla\Delta N^{bi}}^2 & 0 & \dots & 0 \\ 0 & 0 & 0 & 0 & 0 & 0 & 0 & 0 & 0 & 0 & \sigma_{\nabla\Delta N^{bi}}^2 & \dots & 0 \\ \vdots & \vdots & \vdots & \vdots & \vdots & \vdots & \vdots & \vdots & \vdots & \vdots & \vdots & \ddots & 0 \\ 0 & 0 & 0 & 0 & 0 & 0 & 0 & 0 & 0 & 0 & 0 & 0 & \sigma_{\nabla\Delta N^{bi}}^2 \end{bmatrix} \tag{3.19}$$

The initial covariance values used in this research are given in Table 3.4 where the number of visible pseudolites in the first epoch is given as n.

Table 3.4 Floating-Point Filter Initial Covariance Values

Term	**Definition**	**Value**
$\sigma_{x,y,z}^2$	Position state variance	$(100\ m)^2$
$\sigma_{\dot{x},\dot{y},\dot{z}}^2$	Velocity State variance	$(400\ m/s)^2$
$\sigma_{\ddot{x},\ddot{y},\ddot{z}}^2$	Acceleration state variance	$(20\ m/s^2)^2$
$\sigma_{\nabla\Delta N^{bi}}^2$	Phase ambiguity variance	$(\frac{50}{\lambda}\ cycles)^2$

3.5.2 Differential Pseudolite Measurement Model. The floating-point differential pseudolite Kalman filter uses a nonlinear measurement model which consists of double-differenced code and phase measurements resulting in a $2(n-1)$ measure-

ment vector (where n is the number of pseudolites in view) defined by

$$\mathbf{z}(t_i) = [\nabla\Delta\rho^{1-2} \cdots \nabla\Delta\rho^{1-n} \nabla\Delta\phi^{1-2} \cdots \nabla\Delta\phi^{1-n}]^T \tag{3.20}$$

From Chapter 2, Equation 2.23 described the nonlinear measurement model for an extended Kalman filter which is in the form:

$$\mathbf{z}(t_i) = \mathbf{h}[\mathbf{x}(t_i), t_i] + \mathbf{v}(t_i) \tag{3.21}$$

It must be linearized before it is used in the gain and covariance calculations of the extended Kalman filter. Recall from Chapter 2 that thee partial derivative matrix $\mathbf{H}$ was defined as

$$\mathbf{H}[t_i; \hat{\mathbf{x}}(t_i^-)] \equiv \left.\frac{\partial \mathbf{h}[\mathbf{x}, t_i]}{\partial \mathbf{x}}\right|_{\mathbf{x}=\hat{\mathbf{x}}(t_i^-)} \tag{3.22}$$

which is an $m \times s$ matrix, where m is the number of measurements and s is the number of states. Each row corresponds to a single measurement and is defined as

$$\left.\frac{\partial \mathbf{h}[\mathbf{x}, t_i]}{\partial \mathbf{x}}\right|_{\mathbf{x}=\hat{\mathbf{x}}(t_i^-)} = \left[\left.\frac{\partial \mathbf{h}[\mathbf{x}, t_i]}{\partial \mathrm{x}_1}\right|_{\mathbf{x}=\hat{\mathbf{x}}(t_i^-)} \left.\frac{\partial \mathbf{h}[\mathbf{x}, t_i]}{\partial \mathrm{x}_2}\right|_{\mathbf{x}=\hat{\mathbf{x}}(t_i^-)} \cdots \left.\frac{\partial \mathbf{h}[\mathbf{x}, t_i]}{\partial \mathrm{x}_\mathrm{s}}\right|_{\mathbf{x}=\hat{\mathbf{x}}(t_i^-)} \right] \tag{3.23}$$

Recall from Equation 2.57 that the double-differenced carrier-phase measurement is given by

$$\Delta\nabla\phi_{AB}^{kj} = \lambda^{-1}(\Delta\nabla r_{AB}^{kj} + \Delta\nabla T_{AB}^{kj} + \Delta\nabla m_{AB}^{kj} + \Delta\nabla v_{AB}^{kj}) + \Delta\nabla N_{AB}^{kj} \tag{3.24}$$

The λ term in Equation 3.24 is the carrier wavelength and will depend on whether a single or widelane frequency is used.

When the double-differenced range term is expanded and the measurement errors are combined the carrier-phase equation is expressed as

$$\Delta\nabla\phi_{AB}^{jk} = \frac{1}{\lambda}\left[r_B^j - r_A^j - (r_B^k - r_A^k)\right] + \Delta\nabla N_{AB}^{jk} + v_{\Delta\nabla\phi} \tag{3.25}$$

In the preceding equation, the term $v_{\Delta\nabla\phi}$ is modeled as a white noise, and it represents the combination of the doubled-differenced measurement noise, multipath, and tropospheric delay. It is important to note that the tropospheric delay terms are the residual error after a tropospheric model has been applied. When the range terms in Equation 3.25 are further expanded and expressed in terms of state variables, the equation becomes

$$\begin{aligned}\Delta\nabla\Phi_{AB}^{jk} = & \frac{1}{\lambda}\left[(x^j - x_1)^2 + (y^j - x_2)^2 + (z^j - x_3)^2\right]^{1/2} \\ & - \left[(x^k - x_1)^2 + (y^k - x_2)^2 + (z^k - x_3)^2\right]^{1/2} \\ & + \frac{1}{\lambda}\left\{r_A^k - r_A^j\right\} + \Delta\nabla N_{AB}^{jk} + v_{\Delta\nabla\Phi}\end{aligned} \tag{3.26}$$

where $x^{j,k}, y^{j,k}, z^{j,k}$ represent the estimate of the pseudolites indexed by j and k. Recall the $\frac{1}{\lambda}\left\{r_B^k - r_B^j\right\}$ term represents the mobile receiver and is expanded, but the $\frac{1}{\lambda}\left\{r_A^k - r_A^j\right\}$ term represents the reference receiver so it is not a function of state variables, and thus not expanded.

The partial derivatives for each row of the double-differenced carrier-phase measurements are given as

$$\begin{aligned}\left.\frac{\partial h[\mathbf{x}, t_i]}{\partial x_1}\right|_{\mathbf{x}=\hat{\mathbf{x}}(t_i^-)} & = \frac{1}{\lambda}\left\{\frac{x^j - x_1}{[(x^j-x_1)^2+(y^j-x_2)^2+(z^j-x_3)^2]^{1/2}}\right\} \\ & - \frac{1}{\lambda}\left\{\frac{x^k - x_1}{\left[(x^k-x_1)^2+(y^k-x_2)^2+(z^k-x_3)^2\right]^{1/2}}\right\} \\ & = \frac{1}{\lambda}\left\{e_1^j - e_1^k\right\}\end{aligned} \tag{3.27}$$

$$\begin{aligned}\left.\frac{\partial h[\mathbf{x}, t_i]}{\partial x_2}\right|_{\mathbf{x}=\hat{\mathbf{x}}(t_i^-)} & = \frac{1}{\lambda}\left\{\frac{y^j - x_2}{[(x^j-x_1)^2+(y^j-x_2)^2+(z^j-x_3)^2]^{1/2}}\right\} \\ & - \frac{1}{\lambda}\left\{\frac{y^k - x_3}{\left[(x^k-x_1)^2+(y^k-x_2)^2+(z^k-x_3)^2\right]^{1/2}}\right\} \\ & = \frac{1}{\lambda}\left\{e_2^j - e_2^k\right\}\end{aligned} \tag{3.28}$$

$$\left.\frac{\partial h[\mathbf{x},t_i]}{\partial x_3}\right|_{\mathbf{x}=\hat{\mathbf{x}}(t_i^-)} = \frac{1}{\lambda}\left\{\frac{z^j-x_3}{[(x^j-x_1)^2+(y^j-x_2)^2+(z^j-x_3)^2]^{1/2}}\right\} - \frac{1}{\lambda}\left\{\frac{z^k-x_3}{\left[(x^k-x_1)^2+(y^k-x_2)^2+(z^k-x_3)^2\right]^{1/2}}\right\} = \frac{1}{\lambda}\left\{e_3^j - e_3^k\right\} \tag{3.29}$$

$$\left.\frac{\partial h[\mathbf{x},t_i]}{\partial x_{bi}}\right|_{\mathbf{x}=\hat{\mathbf{x}}(t_i^-)} = 1 \tag{3.30}$$

where

$$\mathbf{e}_{mob}^j = [e_1^j \ e_2^j \ e_3^j] \tag{3.31}$$

is the unit line-of-sight vectors pointing from the mobile receiver to pseudolite j.

When these individual partial derivatives are combined they represent one row of the $\mathbf{H}$ matrix as

$$\mathbf{H}^{jk} = \left[\frac{1}{\lambda}(\mathbf{e}_{mob}^j - \mathbf{e}_{mob}^k) \ 0 \ 0 \ 0 \ 0 \ 0 \ 0 \ \cdots 1 \cdots 0\right] \tag{3.32}$$

where $\frac{1}{\lambda}(\mathbf{e}_{mob}^j - \mathbf{e}_{mob}^k)$ represents the scaled difference vector between two unit line-of-site vectors from the mobile receiver to pseudolite "j" and the mobile receiver to pseudolite "k". The "1" is placed in the column for the appropriate ambiguity state.

The corresponding rows for the double differenced code measurements are the same values after the $\frac{1}{\lambda}$ term is removed and the "1" for the ambiguity state values is dropped:

$$\mathbf{H}^{jk} = \left[(\mathbf{e}_{mob}^j - \mathbf{e}_{mob}^k) \ 0 \ 0 \ 0 \ 0 \ 0 \ 0 \ \cdots 0\right] \tag{3.33}$$

The entire measurement matrix $\mathbf{H}$ is an 9+(n-1) by 2(n-1) matrix defined by

$$\mathbf{H} = \begin{bmatrix} (\mathbf{e}^1 - \mathbf{e}^2) & 0 & 0 & 0 & 0 & 0 & 0 & 0 & 0 & \cdots & 0 \\ (\mathbf{e}^1 - \mathbf{e}^3) & 0 & 0 & 0 & 0 & 0 & 0 & 0 & 0 & \cdots & 0 \\ \vdots & \vdots & \vdots & \vdots & \vdots & \vdots & \vdots & \vdots & \vdots & \ddots & \vdots \\ (\mathbf{e}^1 - \mathbf{e}^n) & 0 & 0 & 0 & 0 & 0 & 0 & 0 & 0 & \cdots & 0 \\ \frac{1}{\lambda}(\mathbf{e}^1 - \mathbf{e}^2) & 0 & 0 & 0 & 0 & 0 & 0 & 1 & 0 & \cdots & 0 \\ \frac{1}{\lambda}(\mathbf{e}^1 - \mathbf{e}^3) & 0 & 0 & 0 & 0 & 0 & 0 & 0 & 1 & \cdots & 0 \\ \vdots & \vdots & \vdots & \vdots & \vdots & \vdots & \vdots & \vdots & \vdots & \ddots & 0 \\ \frac{1}{\lambda}(\mathbf{e}^1 - \mathbf{e}^n) & 0 & 0 & 0 & 0 & 0 & 0 & 0 & 0 & \cdots & 1 \end{bmatrix} \tag{3.34}$$

where b is the base pseudolite for n pseudolites where $i = 1 \cdots n$, with $i \neq$ base pseudolite.

The measurement covariance matrix $\mathbf{R}$ is defined by

$$E\{\mathbf{v}(t_i)\mathbf{v}^T(t_i)\} = \begin{cases} \mathbf{R}(t_i) \text{ for } t_i \neq t_j \\ \mathbf{0} \text{ for } t_i \neq t_j \end{cases} \tag{3.35}$$

is required by the filter. This matrix can be broken up into 4 different types of covariance terms.

- Case 1: Variance of code measurement errors
- Case 2: Variance of phase measurement errors
- Case 3: Covariance of two different code measurement errors
- Case 4: Covariance of two different phase measurement errors

The full $\mathbf{R}$ matrix can be partitioned into four sections represented by

$$\begin{bmatrix} \mathbf{R}_{code} & \mathbf{0} \\ \mathbf{0} & \mathbf{R}_{phase} \end{bmatrix}$$

where the code variance and covariances denoted by cases 1 and 3, respectively, are placed in the upper left corner. The phase variances and covariances denoted by cases 2 and 4 are located in the lower right corner. The upper right and lower left corners represent the cross-covariance of a code and phase measurement. These values were assumed to be sufficiently small to ignore them.

The variances for the code measurement are a combination of residual tropospheric error and the non-tropospheric components (transmitter location error, multipath, and measurement noise). For this research, the non-tropospheric error was assumed to be uncorrelated between measurements, which means that the double-differenced standard deviation is a factor of two greater than the observation standard deviation. The double-differenced standard deviations for the tropospheric and non-tropospheric errors were 3.2 meters and 0.07 meters, respectively, which resulted in a total standard deviation of 3.2008 meters. It is important to note that the tropospheric contribution to the total standard deviation is sufficiently small to ignore, but is included for completeness. The covariances of two different code measurements were set as one half of the code variances, because half of the measurements are in common due to double differencing. The following matrix defines the code segment of the $\mathbf{R}$ matrix.

$$\mathbf{R}_{code} = \begin{bmatrix} r_{\nabla\Delta\rho^{ij},\nabla\Delta\rho^{ij}} & r_{\nabla\Delta\rho^{ij},\nabla\Delta\rho^{ik}} & \cdots & r_{\nabla\Delta\rho^{ij},\nabla\Delta\rho^{ik}} \\ r_{\nabla\Delta\rho^{ij},\nabla\Delta\rho^{ik}} & r_{\nabla\Delta\rho^{ij},\nabla\Delta\rho^{ij}} & \ddots & \vdots \\ \vdots & \ddots & \ddots & r_{\nabla\Delta\rho^{ij},\nabla\Delta\rho^{ik}} \\ r_{\nabla\Delta\rho^{ij},\nabla\Delta\rho^{ik}} & \cdots & r_{\nabla\Delta\rho^{ij},\nabla\Delta\rho^{ik}} & r_{\nabla\Delta\rho^{ij},\nabla\Delta\rho^{ij}} \end{bmatrix} \tag{3.36}$$

The phase variances and covariances were developed in a similar manner to the code values. The double-differenced tropospheric and non-tropospheric standard deviations are 0.0812 cycles and 0.0464 cycles, respectively, with the resulting total standard deviation of 0.0935 cycles. The phase variance was calculated to be 0.0087 square cycles and the covariances 0.00435 square cycles. The following matrix dis-

plays the phase component of the full $\mathbf{R}$ matrix.

$$\mathbf{R}_{phase} = \begin{bmatrix} r_{\nabla\Delta\phi^{ij},\nabla\Delta\phi^{ij}} & r_{\nabla\Delta\phi^{ij},\nabla\Delta\phi^{ik}} & \cdots & r_{\nabla\Delta\phi^{ij},\nabla\Delta\phi^{ik}} \\ r_{\nabla\Delta\phi^{ij},\nabla\Delta\phi^{ik}} & r_{\nabla\Delta\phi^{ij},\nabla\Delta\phi^{ij}} & \ddots & \vdots \\ \vdots & \ddots & \ddots & r_{\nabla\Delta\phi^{ij},\nabla\Delta\phi^{ik}} \\ r_{\nabla\Delta\phi^{ij},\nabla\Delta\phi^{ik}} & \cdots & r_{\nabla\Delta\phi^{ij},\nabla\Delta\phi^{ik}} & r_{\nabla\Delta\phi^{ij},\nabla\Delta\phi^{ij}} \end{bmatrix} \tag{3.37}$$

The values for the the $\mathbf{R}$ matrix are shown in Table 3.5.

Table 3.5 Measurement Covariance Values

Term	**Definition**	**Value**
$r_{\nabla\Delta\rho^{ij},\nabla\Delta\rho^{ij}}$	Double-differenced code variance error	10.24 m^2
$r_{\nabla\Delta\rho^{ij},\nabla\Delta\rho^{ik}}$	Double-differenced code covariance error	5.12 m^2
$r_{\nabla\Delta\phi^{ij},\nabla\Delta\phi^{ij}}$	Double-differenced carrier-phase variance error	.0087 $cycles^2$
$r_{\nabla\Delta\phi^{ij},\nabla\Delta\phi^{ik}}$	Double-differenced carrier-phase covariance error	.00435 $cycles^2$

3.5.3 Discrete-Time Models. The linear stochastic differential equations must be converted to be implemented on a digital computer. This requires the formulation of the linear stochastic difference equations to describe the equivalent discrete-time system model [19], which is in the form

$$\mathbf{x}(t_{k+1}) = \mathbf{\Phi}(t_{k+1}, t_k)\mathbf{x}(t_k) + \mathbf{w}_d \tag{3.38}$$

where

$$\begin{aligned} E\{\mathbf{w}_d\} &= \mathbf{0} \\ E\{\mathbf{w}_d(t_k)\mathbf{w}_d^T(t_k)\} &= \mathbf{Q}_d \\ E\{\mathbf{w}_d(t_j)\mathbf{w}_d^T(t_k)\} &= \mathbf{0}, \mathrm{t_j} \neq t_k \end{aligned} \tag{3.39}$$

Equations 3.38 through 3.40 were derived in Chapter 2. The discrete-time state transition matrix $\mathbf{\Phi}(t_{k+1}, t_k)$ is defined as:

$$\mathbf{\Phi}(t_{k+1}, t_k) = \mathbf{\Phi}(\Delta t) = e^{\mathbf{F}\Delta t} \tag{3.40}$$

where $\Delta t \equiv t_{k+1} - t_k$ which results in the matrix

$$\mathbf{\Phi}(t_{k+1}, t_k) = \begin{bmatrix} 1 & 0 & 0 & \Delta t & 0 & 0 & A & 0 & 0 & 0 & 0 & \cdots & 0 \\ 0 & 1 & 0 & 0 & \Delta t & 0 & 0 & A & 0 & 0 & 0 & \cdots & 0 \\ 0 & 0 & 1 & 0 & 0 & \Delta t & 0 & 0 & A & 0 & 0 & \cdots & 0 \\ 0 & 0 & 0 & 1 & 0 & 0 & B & 0 & 0 & 0 & 0 & \cdots & 0 \\ 0 & 0 & 0 & 0 & 1 & 0 & 0 & B & 0 & 0 & 0 & \cdots & 0 \\ 0 & 0 & 0 & 0 & 0 & 1 & 0 & 0 & B & 0 & 0 & \cdots & 0 \\ 0 & 0 & 0 & 0 & 0 & 0 & C & 0 & 0 & 0 & 0 & \cdots & 0 \\ 0 & 0 & 0 & 0 & 0 & 0 & 0 & C & 0 & 0 & 0 & \cdots & 0 \\ 0 & 0 & 0 & 0 & 0 & 0 & 0 & 0 & C & 0 & 0 & \cdots & 0 \\ 0 & 0 & 0 & 0 & 0 & 0 & 0 & 0 & 0 & 1 & 0 & \cdots & 0 \\ 0 & 0 & 0 & 0 & 0 & 0 & 0 & 0 & 0 & 0 & 1 & \cdots & 0 \\ \vdots & \vdots & \vdots & \vdots & \vdots & \vdots & \vdots & \vdots & \vdots & \vdots & \vdots & \ddots & 0 \\ 0 & 0 & 0 & 0 & 0 & 0 & 0 & 0 & 0 & 0 & 0 & 0 & 1 \end{bmatrix} \tag{3.41}$$

where

$$A = T_a^2(e^{-\Delta t/T_a} - 1) + T_a \Delta t$$
$$B = T_a(1 - e^{-\Delta t/T_a})$$
$$C = (e^{-\Delta t/T_a})$$

The discrete dynamics driving noise is given by

$$\mathbf{Q}_d(t_k) = \int_{t_k}^{t_{k+1}} \mathbf{\Phi}(t_{k+1,}\tau)\mathbf{G}(\tau)\mathbf{Q}(\tau)\mathbf{G}^T(\tau)\mathbf{\Phi}^T(t_{k+1,\tau})d\tau \tag{3.42}$$

which expands to

$$\mathbf{Q}_{d=}\begin{bmatrix} D & 0 & 0 & E & 0 & 0 & G & 0 & 0 & 0 & 0 & \cdots & 0 \\ 0 & D & 0 & 0 & E & 0 & 0 & G & 0 & 0 & 0 & \cdots & 0 \\ 0 & 0 & D & 0 & 0 & E & 0 & 0 & G & 0 & 0 & \cdots & 0 \\ E & 0 & 0 & K & 0 & 0 & L & 0 & 0 & 0 & 0 & \cdots & 0 \\ 0 & E & 0 & 0 & K & 0 & 0 & L & 0 & 0 & 0 & \cdots & 0 \\ 0 & 0 & E & 0 & 0 & K & 0 & 0 & L & 0 & 0 & \cdots & 0 \\ G & 0 & 0 & L & 0 & 0 & M & 0 & 0 & 0 & 0 & \cdots & 0 \\ 0 & G & 0 & 0 & L & 0 & 0 & M & 0 & 0 & 0 & \cdots & 0 \\ 0 & 0 & G & 0 & 0 & L & 0 & 0 & M & 0 & 0 & \cdots & 0 \\ 0 & 0 & 0 & 0 & 0 & 0 & 0 & 0 & 0 & N & 0 & \cdots & 0 \\ 0 & 0 & 0 & 0 & 0 & 0 & 0 & 0 & 0 & 0 & N & \cdots & 0 \\ \vdots & \vdots & \vdots & \vdots & \vdots & \vdots & \vdots & \vdots & \vdots & \vdots & \vdots & \ddots & 0 \\ 0 & 0 & 0 & 0 & 0 & 0 & 0 & 0 & 0 & 0 & 0 & 0 & N \end{bmatrix} \tag{3.43}$$

where these values were taken from reference [27] and defined as

$$
\begin{aligned}
D &= \frac{1}{2}T_a^5 q_a(1 - e^{-2\Delta t/T_a}) + T_a^4 q_a \Delta t(1 - 2^{-\Delta t/T_a}) - T_a^3 q_a (\Delta t)^2 + \frac{1}{3}T_a^2 q_a (\Delta t)^3 \\
E &= T_a^4 q_a(\frac{1}{2}e^{-2\Delta t/T_a} - e^{-\Delta t/T_a} + \frac{1}{2}) + T_a^3 q_a \Delta t(e^{-\Delta t/T_a} - 1) + \frac{1}{2}T_a^2 q_a (\Delta t)^2 \\
G &= \frac{1}{2}T_a^3 q_a(1 - e^{-2\Delta t/T_a}) - T_a^2 q_a \Delta t e^{-\Delta t/T_a} \\
K &= \frac{1}{2}T_a^3 q_a(-e^{-2\Delta t/T_a} + 4e^{-\Delta t/T_a} + 2\frac{\Delta t}{T_a} - 3) \\
L &= -\frac{1}{2}T_a^2 q_a(-e^{-2\Delta t/T_a} + 2e^{-\Delta t/T_a} - 1) \\
M &= -\frac{1}{2}T_a q_a(-e^{-2\Delta t/T_a} - 1) \\
N &= q_N \Delta t
\end{aligned}
$$

3.6 Floating-Point Filter Features

The floating-point filter included a pre-filtering step, real-data considerations, a tropospheric model, and adaptations to improve upon the performance of the baseline filter. These adaptations consisted of optimal smoothing techniques, second order filtering, weighted measurement covariance matrix, and estimating errors in the tropospheric model.

3.6.1 Pre-filter. A pre-filter function was implemented to determine the number of available PRNs, vector of available PRNs, and base PRN for double difference operations. The base PRN was initially chosen from a vector of prns that were in view at the first epoch. The PRN that stayed in view the longest was chosen. If that PRN did not stay in view the entire data set, the process was repeated in a similiar manner. The process then defined a vector of PRNs that were in view at the second-to-last epoch the initial base PRN went out of view. The PRN that stayed in view the longest was chosen as the base, and if it did not stay in view until the end of the data set, the process repeated itself. The pre-filter function then generates a

pseudolite visibility plot denoting the base PRN with a thick line. Figure 3.6 shows a typical pseudolite visibility plot.

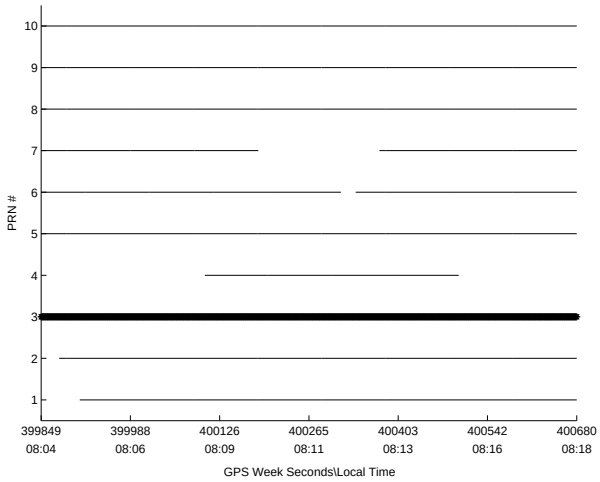

Figure 3.6 Pseudolite Visibility Plot

3.6.2 Real Data Considerations. Although only simulated data was used in this research, every attempt was made to make it as realistic as possible. The filter was designed to handle these real data considerations. The algorithm developed in this thesis included the ability to handle pseudolites going out of view, pseudolites coming into view, and a change in the base double difference PRN.

In a real-world system, pseudolites will go out of view. When this happened, the filter eliminated the appropriate state estimate and the rows and columns associated with this pseudolite prn in the covariance matrix. For example, if pseudolites 1 through 5 were visible with prn 1 as the double difference base, sample ambiguity state values could be

$$x_{10} = \nabla\Delta N^{12} = \text{-2837.24}$$
$$x_{11} = \nabla\Delta N^{13} = 10314.35$$
$$x_{12} = \nabla\Delta N^{14} = \text{-563.10}$$
$$x_{13} = \nabla\Delta N^{15} = 124.73$$

These four ambiguity states would be in states 10 through 13, because the first 9 states represent the 3 position, 3 velocity, and 3 acceleration states. If pseudolite 4 went out of view, the new ambiguity vector would be

$$\begin{aligned} x_{10} &= \nabla\Delta N^{12} = \text{-2837.24} \\ x_{11} &= \nabla\Delta N^{13} = 10314.35 \\ x_{12} &= \nabla\Delta N^{15} = 124.73 \end{aligned}$$

The covariance matrix P also requires adjusting. In this example, it would have initially been a 13 by 13 matrix. By way of example, consider a case in which the 4-by-4 partition of the ambiguity variances and covariances is

$$\mathrm{P} = \begin{bmatrix} 0.0063449 & 0.0037111 & 0.004901 & 0.00066232 \\ 0.0037111 & 0.059193 & 0.0038798 & 0.0012557 \\ 0.004901 & 0.0038798 & 0.0064154 & 0.001028 \\ 0.00066232 & 0.0012557 & 0.001028 & 0.0032174 \end{bmatrix}$$

In order to remove the $\nabla\Delta N^{14}$ state the second to last row and second to last column are eliminated. As a result, the covariance becomes

$$\mathrm{P} = \begin{bmatrix} 0.0063449 & 0.0037111 & 0.00066232 \\ 0.0037111 & 0.059193 & 0.0012557 \\ 0.00066232 & 0.0012557 & 0.0032174 \end{bmatrix}$$

In a real-world system, pseudolites will also come into view. When a pseudolite comes into view, both the length of the state vector and the dimensions of the covariance will have to increase by one. The first step is to estimate the new ambiguity term in a similar fashion to the way the ambiguity states were initialized at the first epoch; see Section 3.4.1. The covariance matrix variance term is set to the same ambiguity variance term used in the first epoch, $\left(\frac{50}{\lambda} cycles\right)^2$, while the off-diagonal terms for the row and column are set to zero. Taking the previous example with pseudolite 4

coming back into view, including the estimate of -564.1 for $\nabla\Delta N^{14}$ determined by the code, would be

$$\begin{aligned} x_{10} &= \nabla\Delta N^{12} = \text{-2837.24} \\ x_{11} &= \nabla\Delta N^{13} = 10314.35 \\ x_{12} &= \nabla\Delta N^{14} = \text{-564.1} \\ x_{13} &= \nabla\Delta N^{15} = 124.73 \end{aligned}$$

with the covariance given by

$$\mathrm{P} = \begin{bmatrix} 0.0063449 & 0.0037111 & 0 & 0.00066232 \\ 0.0037111 & 0.059193 & 0 & 0.0012557 \\ 0 & 0 & 3350 & 0 \\ 0.00066232 & 0.0012557 & 0 & 0.0032174 \end{bmatrix}$$

The value of 3350 for the new ambiguity state variance assume a widelane wavelength.

The base pseudolite PRN used for double difference operations cannot be assumed constant over the entire data set. This thesis included a function that translated the ambiguities from that last epoch to the current. A transformation matrix was formed, based on the available prns and base prn at both the last epoch and current epoch. The double differenced ambiguities are combinations of single differenced ambiguities which makes this transformation possible. No information is lost in the translation: the new state and covariance are just different measurement combinations. This function must be performed before the ambiguity states and covariance matrices are adjusted for lost or gained pseudolites.

The relation is given as:

$$\mathbf{x}_{new} = \mathbf{T}\mathbf{x}_{old} \tag{3.44}$$

$$\mathbf{P}_{new} = \mathbf{T}\mathbf{P}_{old}\mathbf{T}^T \tag{3.45}$$

Consider using the previous example, when all five pseudolites were in view and the current base PRN was going out of view, the translation matrix $\mathbf{T}$ to switch the double difference base PRN from 1 to 3 would be

$$\mathbf{T} = \begin{bmatrix} 1 & 0 & 0 & 0 & 0 & 0 & 0 & 0 & 0 & 0 & 0 & 0 & 0 \\ 0 & 1 & 0 & 0 & 0 & 0 & 0 & 0 & 0 & 0 & 0 & 0 & 0 \\ 0 & 0 & 1 & 0 & 0 & 0 & 0 & 0 & 0 & 0 & 0 & 0 & 0 \\ 0 & 0 & 0 & 1 & 0 & 0 & 0 & 0 & 0 & 0 & 0 & 0 & 0 \\ 0 & 0 & 0 & 0 & 1 & 0 & 0 & 0 & 0 & 0 & 0 & 0 & 0 \\ 0 & 0 & 0 & 0 & 0 & 1 & 0 & 0 & 0 & 0 & 0 & 0 & 0 \\ 0 & 0 & 0 & 0 & 0 & 0 & 1 & 0 & 0 & 0 & 0 & 0 & 0 \\ 0 & 0 & 0 & 0 & 0 & 0 & 0 & 1 & 0 & 0 & 0 & 0 & 0 \\ 0 & 0 & 0 & 0 & 0 & 0 & 0 & 0 & 1 & 0 & 0 & 0 & 0 \\ 0 & 0 & 0 & 0 & 0 & 0 & 0 & 0 & 0 & \mathbf{0} & \mathbf{-1} & \mathbf{0} & \mathbf{0} \\ 0 & 0 & 0 & 0 & 0 & 0 & 0 & 0 & 0 & \mathbf{1} & \mathbf{-1} & \mathbf{0} & \mathbf{0} \\ 0 & 0 & 0 & 0 & 0 & 0 & 0 & 0 & 0 & \mathbf{0} & \mathbf{-1} & \mathbf{1} & \mathbf{0} \\ 0 & 0 & 0 & 0 & 0 & 0 & 0 & 0 & 0 & \mathbf{0} & \mathbf{-1} & \mathbf{0} & \mathbf{1} \end{bmatrix} \tag{3.46}$$

Note that the top left corner is a 9 by 9 identity matrix, which preserves the position, velocity, and acceleration estimates. The bottom righthand corner values (which are bolded) represent the portion of $\mathbf{T}$ that rearranges the ambiguity estimates. The same transformation matrix, $\mathbf{T}$, is applied to the covariance according to Equation 3.45. When $\mathbf{T}$ is multiplied by $\mathbf{x}_{old}$ it forms

$$\begin{aligned} \nabla\Delta N^{31}_{new} &= -\nabla\Delta N^{13}_{old} \\ \nabla\Delta N^{32}_{new} &= -\nabla\Delta N^{13}_{old} \quad +\nabla\Delta N^{12}_{old} \\ \nabla\Delta N^{34}_{new} &= -\nabla\Delta N^{13}_{old} \quad +\nabla\Delta N^{14}_{old} \\ \nabla\Delta N^{35}_{new} &= -\nabla\Delta N^{13}_{old} \quad +\nabla\Delta N^{15}_{old} \end{aligned}$$

3.6.3 Tropospheric Model. The tropospheric model used in the filter was the same as that used to generate the tropospheric delay in the truth simulation. There are two differences between the truth and filter model for the tropospheric delay calculation.

The first source of residual tropospheric error was due to the atmospheric values used in each model. The truth model used true values for atmospheric pressure, temperature, and relative humidity. Errors were added to the true atmospheric values, which were then used in the filter model. These errors were modeled as zero-mean Gaussian random biases with adjustable standard deviations. The standard deviations were set as 4 percent for relative humidity, 1 degree Kelvin for temperature, and 3 millibars for the pressure.

The second error source was from the difference in using the estimated versus the true positions of the receivers and transmitters. The truth model used the true positions while the filter model used the estimated positions. This difference resulted in very small, essentially insignificant, errors for both the slant ranges and elevation angles. This difference was very small in magnitude because the position errors were only a few centimeters while the ranges were measured in kilometers.

3.6.4 Optimal Smoothing. The optimal smoothing algorithm presented in Section 2.4 was implemented to improve the accuracy of the state estimates while decreasing the size of the covariance values. The algorithm required modifications when pseudolites were allowed to come in and out of view and the base PRN for double difference operations changed between epochs. The equations give in Chapter 2 are restated here as

$$
\begin{aligned}
\hat{\mathbf{x}}(t_f|t_f) &= \hat{\mathbf{x}}(t_f^+) \\
\hat{\mathbf{x}}(t_i|t_f) &= \hat{\mathbf{x}}(t_i^+) + \mathbf{A}(t_i)[\hat{\mathbf{x}}(t_{i+1}|t_f) - \hat{\mathbf{x}}(t_{i+1}^-)] \\
\mathbf{A}(t_i) &= \mathbf{P}(t_i^+)\mathbf{\Phi}^T(t_{i+1}, t_i)\mathbf{P}^{-1}(t_{i+1}^-) \\
\mathbf{P}(t_f|t_f) &= \mathbf{P}(t_f^+) \\
\mathbf{P}(t_i|t_f) &= \mathbf{P}(t_i^+) + \mathbf{A}(t_i)[\mathbf{P}(t_{i+1}|t_f) - \mathbf{P}(t_{i+1}^-)]\mathbf{A}^{\mathrm{T}}(t_i)
\end{aligned}
$$

which are run backward from the final time t_f after a first forward pass is made through the data with the extended Kalman filter.

These fixed-interval smoother equations obtained by Meditch [19] will fail when the number of states from one epoch to another is not consistent, or the quantities that the states represent change between epochs. When pseudolites go out or come back into view, the number of ambiguity states changes from one epoch to another. When the double difference base PRN changes, the quantities that the ambiguity states represent also change. To account for these occurrences, the same functions that were used in the forward filter to handle this in the forward filter are adapted for the optimal smoothing algorithm.

When the smoothed estimate, $\hat{\mathbf{x}}(t_i|t_f)$, is generated backward in time, it is formed from $\hat{\mathbf{x}}(t_{i+1}|t_f)$ and $\hat{\mathbf{x}}(t_{i+1}^-)$, which both correspond to the next epoch. If pseudolite 4 was in view at t_{i+1} but not at t_i both $\hat{\mathbf{x}}(t_{i+1}|t_f)$ and $\hat{\mathbf{x}}(t_{i+1}^-)$ will have to be modified just like they lost a pseudolite due to visibility. They are modified by removing the state estimate for pseudolite 4, along with the corresponding rows and columns from the covariance matrix.

Conversely, if pseudolite 4 was in view at t_i but not at t_{i+1} the states $\hat{\mathbf{x}}(t_{i+1}|t_f)$ and $\hat{\mathbf{x}}(t_{i+1}^-)$ will have to add the state estimate for this PRN, in addition to their covariances $\mathbf{P}(t_{i+1}|t_f)$ and $\mathbf{P}(t_{i+1}^-)$, using the procedure shown in Section 3.6.2.

When the base PRN is changed, the states and covariances must also change in a similar manner. The states $\hat{\mathbf{x}}(t_{i+1}|t_f)$ and $\hat{\mathbf{x}}(t_{i+1}^-)$ must be altered to reflect the correct double difference base PRN. The covariances are also required to change accordingly.

3.6.5 Nonlinear Filtering. A number of methods or techniques have been proposed to deal with measurement nonlinearities that were introduced in Section 2.6.3. One was is to simply increase the measurement variances, as done by references [9, 32]. A second method is to implement a full second order filter based on a second order Taylor series approximation to the nonlinear model. A third method has proposed to just include the bias correction terms only [1, 20]. This has been shown to produce very similar performance to the full second order filter without the computational burden of the second moment calculations [20]. The first order extended Kalman filter update equations can be modified to include second order terms for nonlinear filtering, yielding

$$\mathbf{A}(t_i) = \mathbf{H}(t_i)\mathbf{P}(t_i^-)\mathbf{H}^T(t_i) + \hat{\mathbf{B}}_m(t_i^-) + \mathbf{R}(t_i) \tag{3.47}$$

$$\mathbf{K}(t_i) = \mathbf{P}(t_i^-)\mathbf{H}^T(t_i)\mathbf{A}(t_i)^{-1} \tag{3.48}$$

$$\hat{\mathbf{x}}(t_i^+) = \hat{\mathbf{x}}(t_i^-) + \mathbf{K}(t_i)\left\{\mathbf{z}(t_i) - \mathbf{h}\left[\hat{\mathbf{x}}(t_i^-), t_i\right] - \hat{\mathbf{b}}_m(t_i^-)\right\} \tag{3.49}$$

$$\mathbf{P}(t_i^+) = \mathbf{P}(t_i^-) - \mathbf{K}(t_i)\mathbf{H}(t_i)\mathbf{P}(t_i^-) \tag{3.50}$$

where

$$\mathbf{H}[t_i; \hat{\mathbf{x}}(t_i^-)] \equiv \left.\frac{\partial \mathbf{h}[\mathbf{x}, t_i]}{\partial \mathbf{x}}\right|_{\mathbf{x}=\hat{\mathbf{x}}(t_i^-)} \tag{3.51}$$

and the measurement bias correction term is defined by

$$\hat{\mathbf{b}}_{mk}(t_i^-) \equiv \frac{1}{2} tr\left\{\frac{\partial^2 h_k[\hat{\mathbf{x}}(t_i^-), t_i]}{\partial \mathbf{x}^2}\mathbf{P}(t_i^-)\right\} \tag{3.52}$$

with $k = 1, 2, \cdots, m$ and m represents the number of measurements.

The differences between the three modified nonlinear filters are in the derivation for $\hat{\mathbf{B}}_m(t_i^-)$ where:

Bias Correction Term Only	$\hat{\mathbf{B}}_m(t_i^-) \equiv \mathbf{0}$
Modified Truncated Second Order	$\hat{\mathbf{B}}_{mkl}(t_i^-) \equiv -\hat{\mathbf{b}}_{mk}(t_i^-)\hat{\mathbf{b}}_{ml}^T(t_i^-)$
Modified Gaussian Second Order	$\hat{\mathbf{B}}_{mkl}(t_i^-) \equiv \frac{1}{2}tr\left\{\frac{\partial^2 h_k[\hat{\mathbf{x}}(t_i^-),t_i]}{\partial \mathbf{x}^2}\mathbf{P}(t_i^-)\frac{\partial^2 h_l[\hat{\mathbf{x}}(t_i^-),t_i]}{\partial \mathbf{x}^2}\mathbf{P}(t_i^-)\right\}$

The non-zero second partial derivatives are given as

$$\left.\frac{\partial^2 h_k[\mathbf{x},t_i]}{\partial^2 x_1}\right|_{\mathbf{x}=\hat{\mathbf{x}}(t_i^-)} = \frac{1}{\lambda}\left\{\frac{((x^j-x_1)^2+(y^j-x_2)^2+(z^j-x_3)^2)^2-(x^j-x_1)^2}{[(x^j-x_1)^2+(y^j-x_2)^2+(z^j-x_3)^2]^{3/2}}\right\} - \frac{1}{\lambda}\left\{\frac{((x^k-x_1)^2+(y^k-x_2)^2+(z^k-x_3)^2)^2-(x^k-x_1)^2}{\left[(x^k-x_1)^2+(y^k-x_2)^2+(z^k-x_3)^2\right]^{3/2}}\right\} \tag{3.53}$$

$$\left.\frac{\partial^2 h_k[\mathbf{x},t_i]}{\partial^2 x_2}\right|_{\mathbf{x}=\hat{\mathbf{x}}(t_i^-)} = \frac{1}{\lambda}\left\{\frac{((x^j-x_1)^2+(y^j-x_2)^2+(z^j-x_3)^2)^2-(y^j-x_2)^2}{[(x^j-x_1)^2+(y^j-x_2)^2+(z^j-x_3)^2]^{3/2}}\right\} - \frac{1}{\lambda}\left\{\frac{((x^k-x_1)^2+(y^k-x_2)^2+(z^k-x_3)^2)^2-(y^k-x_3)^2}{\left[(x^k-x_1)^2+(y^k-x_2)^2+(z^k-x_3)^2\right]^{3/2}}\right\} \tag{3.54}$$

$$\left.\frac{\partial^2 h_k[\mathbf{x},t_i]}{\partial^2 x_3}\right|_{\mathbf{x}=\hat{\mathbf{x}}(t_i^-)} = \frac{1}{\lambda}\left\{\frac{(((x^j-x_1)^2+(y^j-x_2)^2+(z^j-x_3)^2)^2-(z^j-x_3)^2}{[(x^j-x_1)^2+(y^j-x_2)^2+(z^j-x_3)^2]^{3/2}}\right\} - \frac{1}{\lambda}\left\{\frac{((x^k-x_1)^2+(y^k-x_2)^2+(z^k-x_3)^2)^2-(z^k-x_3)^2}{\left[(x^k-x_1)^2+(y^k-x_2)^2+(z^k-x_3)^2\right]^{3/2}}\right\} \tag{3.55}$$

$$\left.\frac{\partial^2 h_k[\mathbf{x},t_i]}{\partial x_1 \partial x_2}\right|_{\mathbf{x}=\hat{\mathbf{x}}(t_i^-)} = \frac{1}{\lambda}\left\{\frac{-(x^j-x_1)(x^j-x_2)}{[(x^j-x_1)^2+(y^j-x_2)^2+(z^j-x_3)^2]^{3/2}}\right\} - \frac{1}{\lambda}\left\{\frac{-(x^j-x_1)(x^k-x_2)}{\left[(x^k-x_1)^2+(y^k-x_2)^2+(z^k-x_3)^2\right]^{3/2}}\right\} \tag{3.56}$$

$$\left.\frac{\partial^2 h_k[\mathbf{x},t_i]}{\partial x_1 \partial x_3}\right|_{\mathbf{x}=\hat{\mathbf{x}}(t_i^-)} = \frac{1}{\lambda}\left\{\frac{-(x^j-x_1)(z^j-x_3)}{[(x^j-x_1)^2+(y^j-x_2)^2+(z^j-x_3)^2]^{3/2}}\right\} - \frac{1}{\lambda}\left\{\frac{-(x^k-x_1)(z^k-x_3)}{\left[(x^k-x_1)^2+(y^k-x_2)^2+(z^k-x_3)^2\right]^{3/2}}\right\} \tag{3.57}$$

$$\left.\frac{\partial^2 h_k[\mathbf{x},t_i]}{\partial x_2 \partial x_3}\right|_{\mathbf{x}=\hat{\mathbf{x}}(t_i^-)} = \frac{1}{\lambda}\left\{\frac{-(y^j-x_2)(z^j-x_3)}{[(x^j-x_1)^2+(y^j-x_2)^2+(z^j-x_3)^2]^{3/2}}\right\} - \frac{1}{\lambda}\left\{\frac{-(y^k-x_2)(z^k-x_3)}{\left[(x^k-x_1)^2+(y^k-x_2)^2+(z^k-x_3)^2\right]^{3/2}}\right\} \tag{3.58}$$

3.6.6 Weighted Measurement Covariance Matrix. This section describes a novel method to weight the measurement covariance matrix $\mathbf{R}$ selectively, based on the predicted tropospheric delay for each measurement generated by the tropospheric model. This allows the filter to weight measurements, relative to their corresponding predicted tropospheric delay.

Tropospheric delay is a function of the atmospheric parameters, slant range, and elevation angle. The atmospheric parameters are constant for all measurements in a given simulation run. The longer the slant range and the lower the elevation angle, the larger the tropospheric delay. If two measurements have the same atmospheric values, and one measurement has a larger predicted delay, it is due to either a longer slant range and/or a lower elevation angle. For example, if the tropospheric filter computes a tropospheric delay of 8 m for prn 1, and 2 m for PRN 2, the residual tropospheric error after a model can be expected to be 4 times larger for PRN 1 than for PRN 2. It would follow that, as the predicted delay increases, the corresponding value in the $\mathbf{R}$ matrix should also increase. The standard deviations of the measurements (i.e., the square roots of the variance terms along the diagonal of the $\mathbf{R}$ matrix) for the phase is the Root Sum Square (RSS) of the standard deviations for the tropospheric delay error and the non-tropospheric errors. If these standard deviations are 0.09 m and 0.07 m respectively, the RSS is 0.114 m or 0.5991 L1 cycles. The variance is $0.5991^2 = .359$ and the covariance is half the variance as described in Section 3.4.2, which results in the baseline $\mathbf{R}$ matrix for the phase partition as

$$\mathbf{R}_\phi = \begin{bmatrix} .359 & .1795 & .1795 & .1795 & .1795 \\ .1795 & .359 & .1795 & .1795 & .1795 \\ .1795 & .1795 & .359 & .1795 & .1795 \\ .1795 & .1795 & .1795 & .359 & .1795 \\ .1795 & .1795 & .1795 & .1795 & .359 \end{bmatrix} \tag{3.59}$$

This is the approach used in the baseline filter for the measurement covariance matrix computation. When the weighted measurement covariance method is used, the standard deviation for the tropospheric component is not assumed to be 0.09 m for every measurement. Instead, the standard deviations for the tropospheric components were determined by

$$\sigma_{tropo} = |.03 \times tropodelay| = \begin{bmatrix} .161 \\ .080 \\ .053 \\ .213 \\ .004 \end{bmatrix} \tag{3.60}$$

where the absolute value of the scaled (0.03) tropospheric delay in meters to result in a vector of standard deviations. When these values were used in place of a vector of 0.09 m values the $\mathbf{R}$ matrix which is calculated as $.05 * (\sigma_{tropo} * \sigma_{tropo}^T)$, is given as

$$\mathbf{R}_\phi = \begin{bmatrix} .848 & .257 & .213 & .542 & .170 \\ .257 & .312 & .129 & .328 & .103 \\ .213 & .129 & .214 & .272 & .085 \\ .542 & .328 & .272 & 1.384 & .217 \\ .170 & .103 & .085 & .217 & .136 \end{bmatrix} \tag{3.61}$$

The scale factor 0.03 was chosen because it typically was equally likely to produce values above 0.09 as it was to produce values below 0.09 for this trajectory.

3.6.7 Tropospheric Model Error States. The errors in the tropospheric model include measurement errors in the sensors, atmospheric errors due to ground effects, and the use of estimated positions of the transmitters and receivers.

The first error source is the set of errors due to imprecise instruments for measuring atmospheric pressure, temperature, and relative humidity. These errors will affect all measurements by roughly the same percentage.

The second error is due to ground effects from foliage and buildings. The height of a typical test mission could be 2500 meters above the earth's surface, so ground effects that only affect the first 25 meters only represent 1 percent of the total signal range.

The third error is due to using estimated positions of the transmitters and receivers. Because these errors are in the centimeter range, their effect is almost insignificant to the total error of the tropospheric model.

Figure 3.6.7 shows the true tropospheric delay in the top subplot and the residual tropospheric error after the model was applied in the bottom subplot. This was for a typical simulation run.

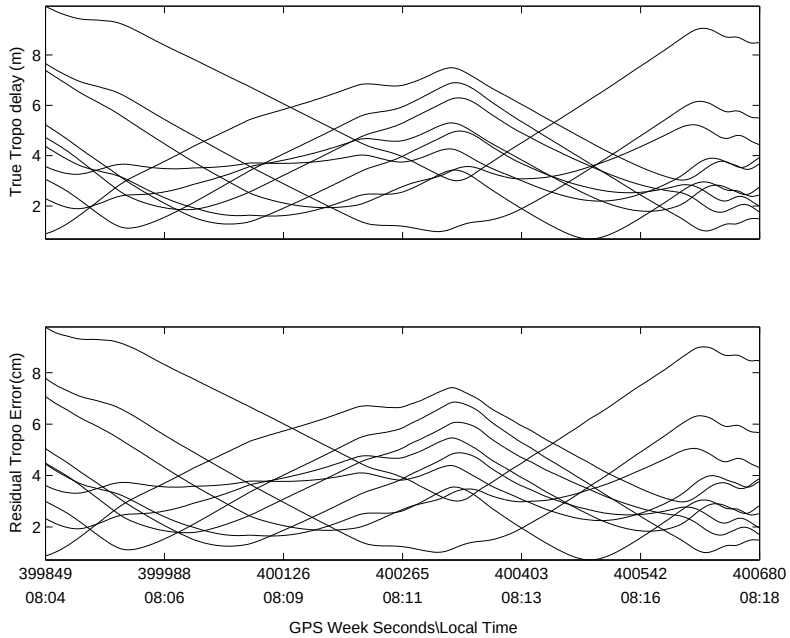

Figure 3.7 True Tropospheric Delay and Residual Tropospheric Error

Although the plots in Figure 3.7 appear to be the same plot, they are not. Note the scaling of the top subplot is in meters and the bottom subplot is in centimeters. The errors are highly correlated to the true tropospheric delay. When the errors are expressed as a percentage of the true delay, they are nearly constant and are shown in Figure 3.8 for both the mobile receiver in the top subplot and the reference receiver in the bottom subplot.

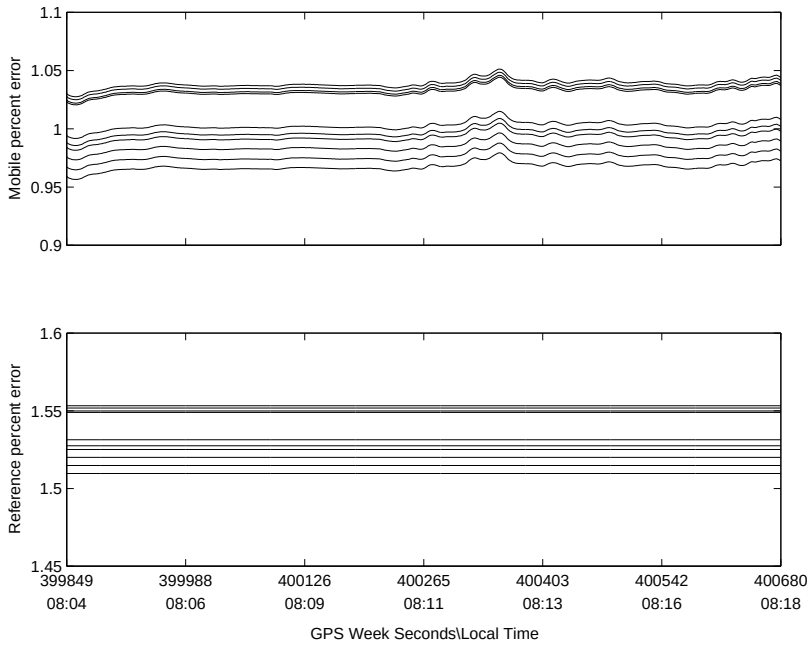

Figure 3.8 Residual Tropospheric Error Expressed as a Percent of Tropospheric Delay

If the residual tropospheric errors after a model is applied are nearly constant, they can be modeled and removed. The error percentages for both the mobile and reference receiver were modeled as First Order Gauss Markov (FOGM) process. Two states were added to the baseline filter, one each for the mobile and reference receiver tropospheric error percentages. These two states were added after the acceleration

states and before the ambiguity states and are defined as

$$\dot{\mathbf{x}}_{10} = (-1/T_t)\mathbf{x}_{10} + w_{t_1}(t)$$
$$\dot{\mathbf{x}}_{11} = (-1/T_t)\mathbf{x}_{11} + w_{t_2}(t) \tag{3.62}$$

with associated dynamic driving noise processes given by

$$E\left\{w_{t_1}(t)w_{t_1}(t+\tau)\right\} = E\left\{w_{t_2}(t)w_{t_2}(t+\tau)\right\} = \frac{2\sigma_t^2}{T_t}\delta(\tau) = q_t\delta(\tau) \tag{3.63}$$

The correlation time, T_t, and variance, σ_t^2, are determined based on the anticipated error percentages and time correlations. The value T_t was set to 75 hours (270000 seconds) to account for typical changes in atmospheric effects, and σ_t was set to 0.03 m to handle the "worst case" error percentage. With these values q_t is calculated to be $1.25 \times 10^{-7} m^2/sec$.

3.7 Carrier-phase Ambiguity Resolution

The structure of the carrier-phase ambiguity resolution techniques are shown in Figure 3.9. First the Z-Transformation is applied to the floating-point ambiguity estimates and covariances. Next, FASF generates the candidate ambiguity sets. If more than one set is generated, a ratio test determines the best ambiguity set, based on the sum of square residuals. The inverse Z-Transformation is applied to bring the selected set of ambiguities back from the LAMBDA domain. LAMBDA, FASF, and the ratio test were described in Chapter 2.

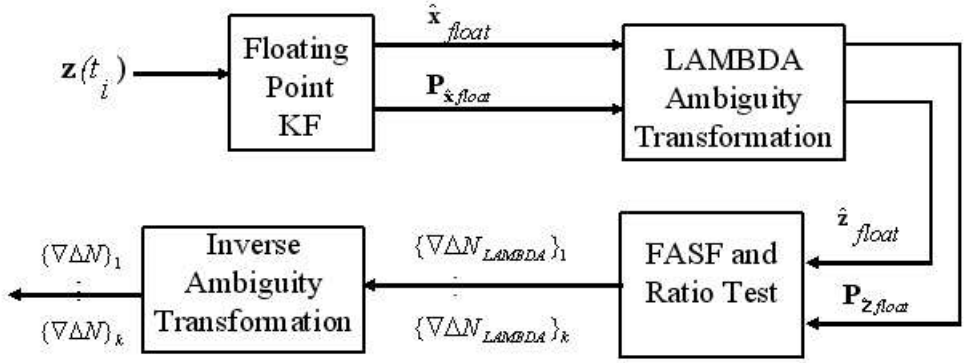

Figure 3.9 Ambiguity Resolution Algorithm Description

3.8 Chapter Summary

This chapter described the truth model and the error generation for both the measurements and measurement model. The floating-point filter was developed along with some modifications. Lastly, the structure of the carrier-phase ambiguity resolution process was described.

IV. Results

4.1 Overview

This chapter presents simulation results and analysis of the algorithm developed in this research. The first section provides the simulation parameters, scenario descriptions, and test case definitions that are used throughout this chapter. The next section analyzes a single filter run to demonstrate the performance. In addition to single-run analysis, Monte Carlo simulations were conducted in which an error sensitivity analysis and a comparison of various filter enhancements was performed. Sections are also included for optimal smoothing, and alternate aircraft trajectories. Recall that the primary purpose of this research is to define design tradeoffs via simulations, and not necessarily to give an absolute measure of the filter's performance.

4.2 Simulation Parameters, Scenario Descriptions and Test Case Definitions

This section describes the simulated trajectory, the atmospheric parameters used in the truth model, along with the scenario descriptions and case definitions. The statistics and criteria used to evaluate the filter performance are also described.

As stated in Section 3.2.2, the trajectory was from actual C-12 flight data. The 832 second (14 minute) section that was used in this research will be referred to as the main flight trajectory. This trajectory resulted in mobile-receiver-to-transmitter ranges of 3 to 32 kilometers. Other flight trajectories were also investigated and they will be described in Section 4.6. For the main flight trajectory, the maximum range from the mobile receiver to any pseudolite was 48 kilometers, while the maximum range from the reference receiver to any pseudolite was 32 kilometers. To simulate pseudolites coming into and going out of view, the maximum range allowed between any pseudolite and the mobile receiver was set at 32 kilometers (just longer than the maximum range to the reference receiver). Any measurement over this limit was

considered out of pseudolite transmission range. This constraint caused the number of visible pseudolites at the mobile receiver to vary between 7 and 10 throughout the simulation, which was shown in Figure 3.6 from Section 3.6.1.

The atmospheric parameters used for the tropospheric truth model are summarized Table 4.1. Atmospheric pressure is the force per unit area exerted against a surface; by the weight of the air above that surface which is sometimes known as barometric pressure [13]. The average atmospheric pressure at sea level is 1013.25 millibars or 29.92 inches of mercury. This was the value used for the truth model for every simulation. Recall that the filter model uses error-corrupted atmospheric values to calculate tropospheric delay. The value of the temperature was chosen as 52 degrees Fahrenheit because that was approximately the average yearly temperature for Holloman AFB, NM. Relative humidity was chosen as 35 percent, because it is a reasonable value for the desert climate at Holloman.

Table 4.1 Atmospheric Parameters Used in Truth Model

Atmospheric pressure	1013.25 mbar (29.92 in)
Temperature	284.26 K (52 F)
Relative humidity	35 percent

Every simulation is classified by a scenario description and test case definition. Each scenario represents a different objective which is shown in Table 4.2. The first two scenarios in the table evaluated the filter's performance with the baseline filter for both the single and widelane observable. The next three scenarios examined the filter's sensitivity to each error source, with the remaining scenarios corresponding to each of the filter enhancements described in Chapter 3.

Table 4.2 List of Scenario Descriptions

Scenario Identifier	Scenario Description
Base	Baseline Filter with Single (L1) Frequency
Base WL	Baseline Filter with Widelane Frequency
PLE	Impact of Pseudolite Location Error
Meas. Noise	Impact of Measurement Noise
Multipath	Impact of Multipath Error
Tropo. Delay	Impact of Tropospheric Delay
PR ave.	L1 and L2 Code Averaging
Bias Corr.	Bias Correction Terms
Smoother	Optimal Smoothing
Weighted R	Weighted Measurement Covariance (R) Matrix
Tropo. State	Tropospheric Model Error States
All Enh.	All Enhancements except Tropo. State

The measurement errors that were described in Chapter 3 represent the nominal error case. In order to test realistic magnitudes of measurement errors fully, the best and worst case scenarios were implemented. They represent one half and twice the nominal case for each of the measurement error sources.

The Monte Carlo simulation included evaluation criteria for both the floating-point results and the ability to resolve the ambiguities. The floating-point criteria included the Root Mean Square (RMS) of the three-dimensional position error, the RMS of the ambiguity error, and the RMS of the standard deviations for the ambiguity state estimates (square root of the state covariance matrix entries).

The RMS position error calculation was a three dimensional Distance RMS (DRMS) which can also be referred to as a Mean Radial Spherical Error (MRSE)

defined as

$$\text{3D RMS} = \sqrt{\frac{\sum_{i=1}^{m} (x_i^2 + y_i^2 + z_i^2)}{m}} \tag{4.1}$$

where x_i, y_i, and z_i represent the position error, in each axis, and m is the number of measurement epochs. These are temporally arranged, versus ensemble-averaged statistics. The RMS statistic for the ambiguity error was defined as

$$\nabla\Delta N_{err} \text{ RMS} = \sqrt{\frac{\sum_{i=1}^{m} \left(\frac{\sum_{j=1}^{n(t_i)} x_j^2(t_i)}{n(t_i)} \right)}{m}} \tag{4.2}$$

where $x_j(t_i)$ is the ambiguity error which was summed for each each ambiguity per epoch (n) and for each epoch (m). The RMS value for the ambiguity standard deviations were calculated in a similar where

$$\sigma_{\nabla\Delta N} \text{ RMS} = \sqrt{\frac{\sum_{i=1}^{m} \left(\frac{\sum_{j=1}^{n(t_i)} \sigma_j^2(t_i)}{n(t_i)} \right)}{m}} \tag{4.3}$$

with $\sigma_j(t_i)$ representing the standard deviation (square root of the ambiguity state covariance) of a given ambiguity. For the Monte Carlo simulation, these values were evaluated for epochs 400 through 832 (final 7 minutes) to allow the filter to converge before calculating statistics on the performance.

The RMS statistic was chosen to represent floating-point filter performance because it required only one value, versus two if mean and standard deviation statistics were used. The primary objective was the fixed-integer carrier-phase performance.

In addition to the floating-point filter criteria, the percentages of correct fixes for both simple rounding and the ambiguity resolution techniques described in Chapter 3 are used. Because ambiguity resolution cannot always resolve the ambiguities,

the percentage of incorrect and unresolved epochs are also given, as shown in Table 4.3.

Round $\%corr$	Percentage of correct fixes using simple rounding
Amb. Res. $\%corr$	Percentage of correct epochs with LAMBDA and FASF
Amb. Res. $\%incorr$	Percentage of incorrect epochs with LAMBDA and FASF
Amb. Res. $\%unres$	Percentage of unresolved epochs with LAMBDA and FASF

Table 4.3 Ambiguity Resolution Evaluation Criteria

The floating-point ambiguity state estimates and their associated covariances were saved for 10 equally spaced epochs in the second half of the simulated test run. The first evaluation criterion was to apply simple rounding of the ambiguities, and then to calculate the percent of the epochs that were correct (i.e., where all of the floating-point ambiguities were within one-half of a cycle of the true integer ambiguity). The rounded solution was considered correct only if all ambiguities for that epoch were correct. The LAMBDA/FASF ambiguity resolution techniques described in Section 2.5.8 were also applied to the same floating-point state estimates and the percentage of correct fixes, percentage of incorrect fixes, and percentage of epochs where the ambiguities were unresolved, were all computed.

4.3 Single Run Performance

This section evaluates a typical run of the baseline filter for the single (L1) observable. The position error, velocity, acceleration, measurement residuals, and ambiguity errors are investigated. While this section examines the filter for a single run, the following section provides Monte Carlo simulation analysis in order to provide a complete picture of filter performance. Recall from Section 3.3 that the truth model only determined the true position of the receivers along with measurement errors. Therefore, error plots are not presented for the velocity and accelerations.

Although the primary goal of the filter is to achieve a high level of accuracy for the ambiguity estimates, the error in estimated receiver position can indicate how well the filter is performing. The X, Y, and Z position errors are shown in Figure 4.1, along with the filter-computed standard deviations (square root of the position variances). Note that the position errors are typically less than the one standard deviation (particularly after the initial transients) which may indicate that the filter is tuned somewhat conservatively.

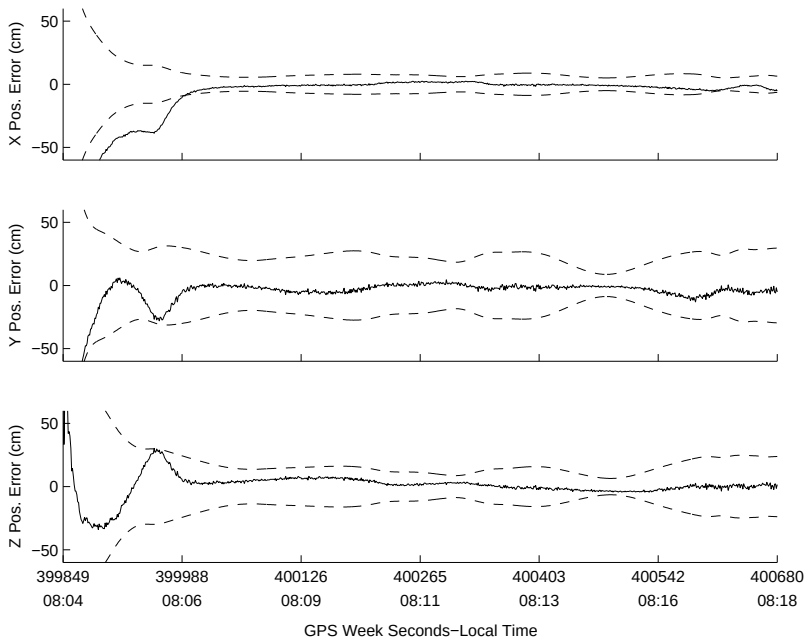

Figure 4.1 Position Errors and Filter-Computed Standard Deviations (Dashed lines)

Notice that the time label given in minutes are rounded to the nearest minute. This label was added to give the reader a sense of the relative time frame of the test run.

A 3-dimensional position error plot more clearly shows the centimeter level accuracy attained by the filter in Figure 4.2. Note that this still represents floating-point ambiguities because ambiguity resolution has not taken place. Recall that a

widelane frequency aids the ambiguity resolution process at the expense of degraded performance in the position solution. If a widelane frequency were used, the performance in the position domain would not achieve this same level. More discussion on the difference in accuracies between the widelane and single frequency is included in Section 4.5.1.

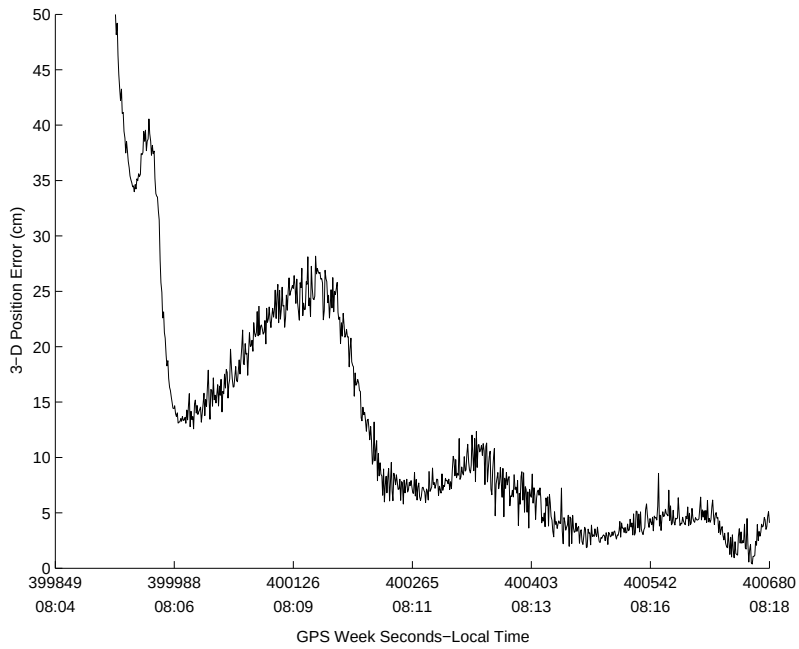

Figure 4.2 3-Dimensional Position Error

The filter also computes the velocities and accelerations in the ECEF frame. When the truth model was generated, only the position of the mobile receiver was simulated. It is still beneficial to plot the velocities and accelerations (Figures 4.3 and 4.4) in order to show when the mobile receiver experienced large accelerations (large for a C-12). Notice that the velocity and especially the acceleration plots indicate large accelerations, both in the middle and at the end of the test run.

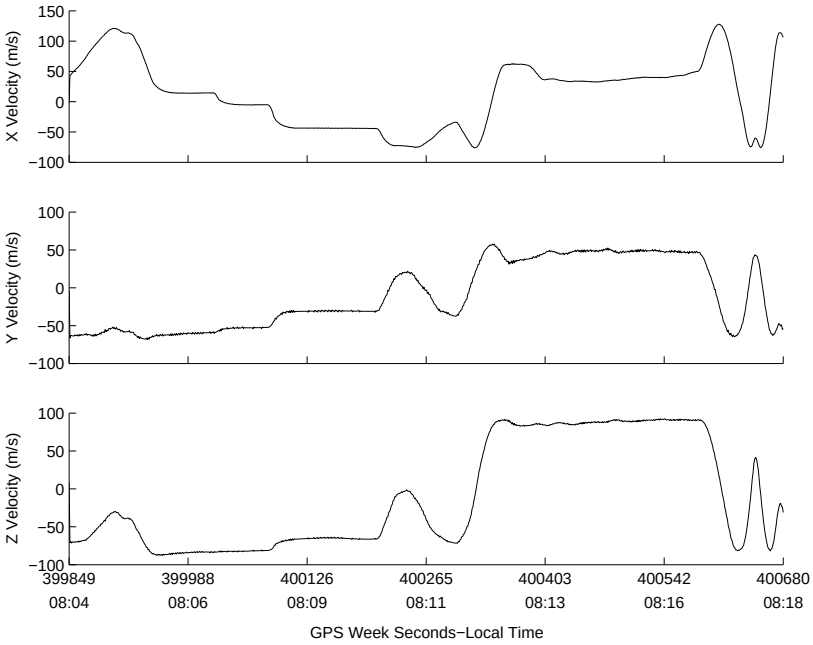

Figure 4.3 Filter-Estimated Velocity

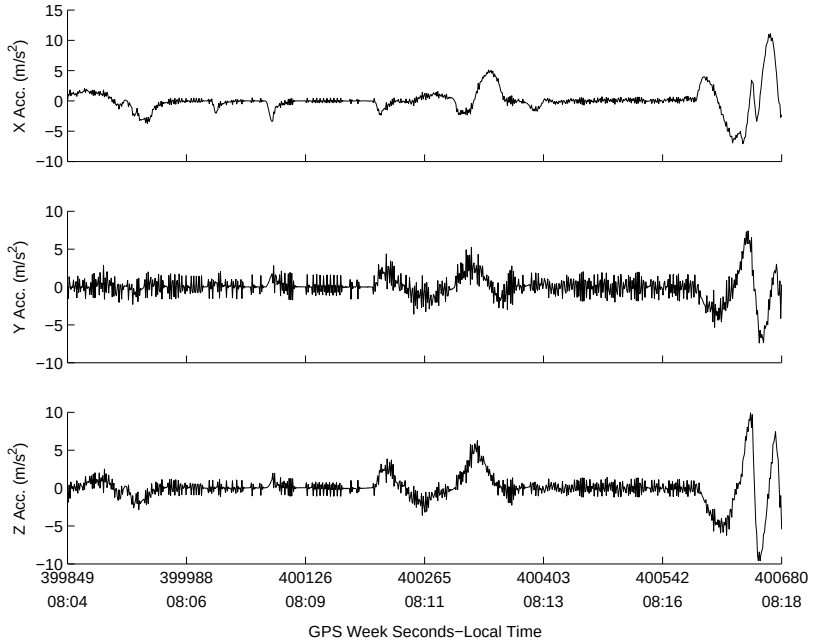

Figure 4.4 Filter-Estimated Acceleration

Residuals are an indicator of filter performance and should be both white (uncorrelated in time) and have a zero-mean distribution. Recall from Section 2.2 that the residuals are defined as the measurement minus the measurement prediction. The residuals for the $\nabla\Delta\rho^{1-2}$ and $\nabla\Delta\phi^{1-2}$ measurements (for comparison purposes) are shown in Figure 4.5. Note the scale of the error for both is given in meters, with the code plot having a larger error range. The code residual appeared to be white for the majority of the plot, with a slight time correlation at the end of the simulation run. The phase residual typically displayed a much smaller magnitude than the code residual, but showed more time correlation. The residuals are a product of measurement errors and dynamics. The phase residuals have much smaller measurement errors, which reduces the size of phase residuals. The dynamics of the receiver affect the code and phase in exactly the same manner. The phase residual plot more clearly shows the effect of vehicle dynamics, because unlike the code measurements, it is not obscured by the measurement errors. These residual errors are due to the inability of the full-state filter to predict future error dynamics precisely during state propagation.

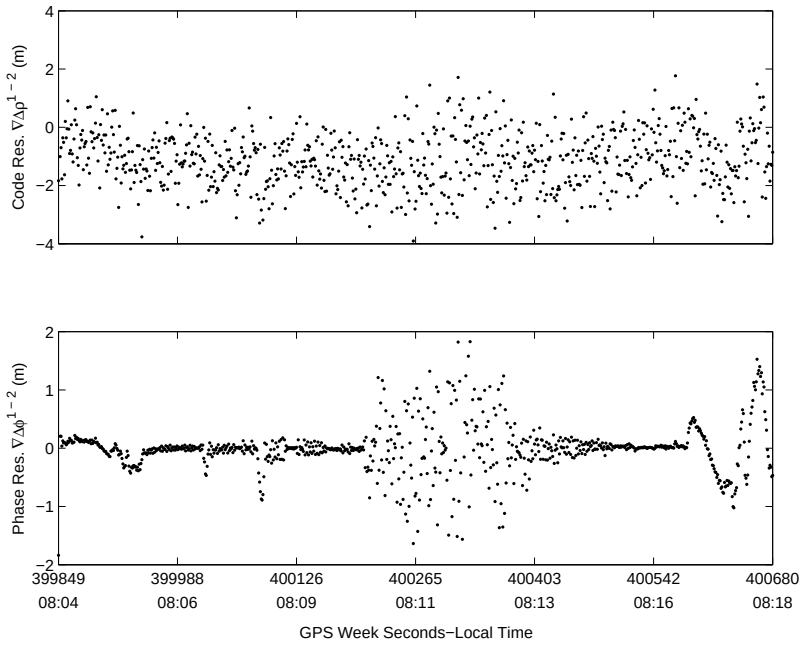

Figure 4.5 Code and Phase Ambiguity Residuals

The ambiguity error for each of the 9 ambiguities, along with their filter-computed 1-σs (square root of their variances), are shown in Figure 4.6. Pseudolites can display much higher levels of relative motion with their receivers than GPS satellite transmitters can. This will result in the filter converging to an ambiguity estimate more quickly. This filter showed convergence with the first 5-7 minutes.

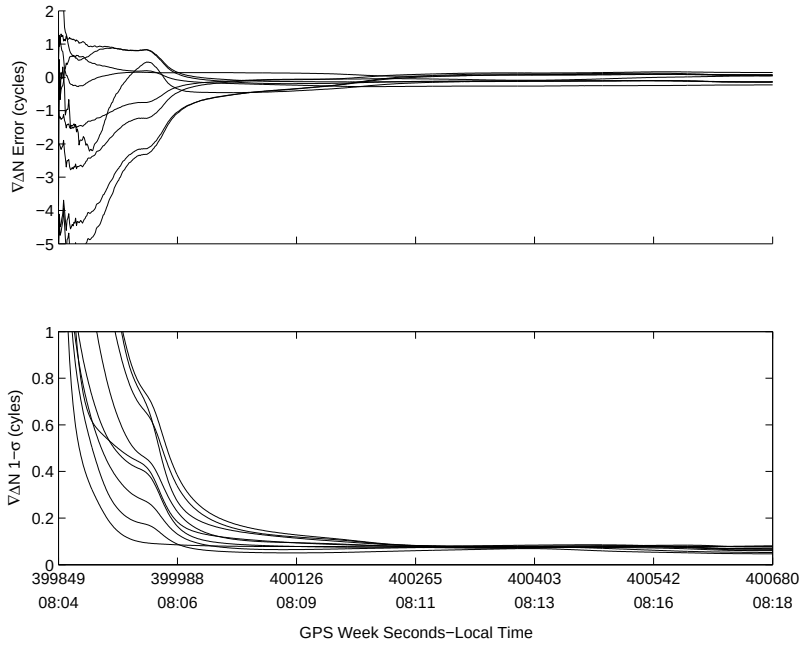

Figure 4.6 Ambiguity Error and Ambiguity 1-σ Plots

4.4 Comparison of Code Versus Relative Motion for Ambiguity Convergence

The two factors that affect the ability of the filter to converge to the correct ambiguity values are the influence of the code measurements and the relative motion between transmitters and receivers. This section analyzes how each of these factors affect filter convergence.

The influence of the relative motion was investigated by artificially increasing the covariance of the code measurement to the point that the code measurements carry very little weight in the filter. Recall from Section 3.5.2 that the covariance of the double difference code measurement was $(5m)^2$. For this test, that value was set to $(1,000,000m)^2$. This essentially removes the effect of code measurements and forces the filter to rely on relative motion only. The results of this test show that, for this simple case, the filter converged more quickly without code than it did with code measurements, as shown in Figure 4.7. From this plot is appears that relative motion is the primary factor in ambiguity convergence.

Ideally, bringing in code measurements, or additional measurements, should not degrade filter performance. Recall that the measurement error sources, especially the multipath, are not zero-mean or uncorrelated in time. The degradation is not a simple mistuning of the code measurement covariance, but rather, a mis-modelling of the error source because the filter is expecting a white, zero-mean measurement error.

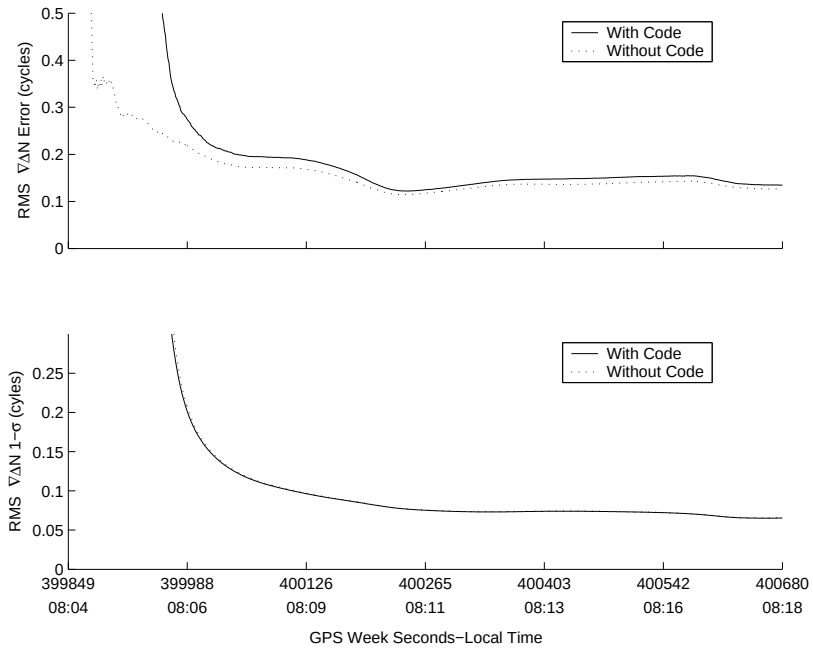

Figure 4.7 RMS Ambiguity Error and Ambiguity 1-σ Plots for $\mathbf{R}_{code} = 10^{12} m^2$

Notice that the covariances are identical in the bottom subplot. This shows that the code measurement variances are not a strong influence on ambiguity covariances.

The influence of code measurements was investigated by changing to a stationary trajectory (i.e., no motion in the mobile receiver). This change caused substantial errors in the ambiguity estimates, increasing the ambiguity estimation errors by approximately a factor of 10. The errors in the filter-corrupted ambiguity estimates

for each of the ten pseudolites are shown in Figure 4.8. This further supports the claim that relative motion is the primary factor in ambiguity convergence.

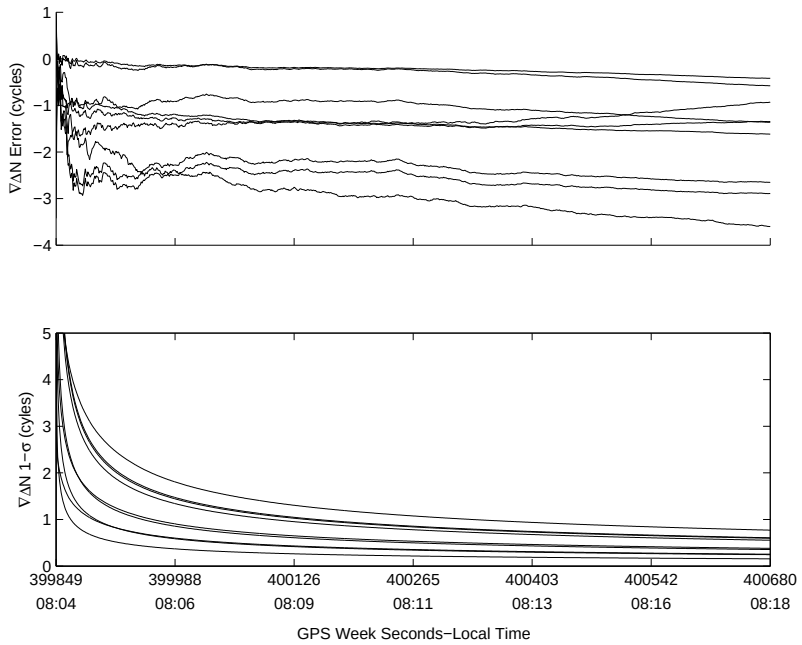

Figure 4.8 Filter Ambiguity Estimate Error and Ambiguity 1-σ Plots for Trajectory without Motion

The analysis suggests a reliance on the relative motion between the transmitters and receivers for accurate ambiguity estimation. These results suggest that a pseudolite-based flight reference system does not need to depend much upon code measurements.

4.5 Monte Carlo Performance

This section first presents the Monte Carlo simulation analysis of the baseline filter for both a single and widelane frequency, then an analysis of the sensitivity of the filter to each error source, and finally a comparison of each filter enhancement described in Chapter 3. The Monte Carlo simulation conducted in this research involved 34 separate tests of 100 runs each.

The baseline filter and filter enhancement scenarios each had three cases: Best, Nominal, and Worst. For these scenarios, all four error sources were set together as the best, nominal, or worst case, in contrast to the sensitivity error analysis where only one source at a time was adjusted to the best or worst case, while the remaining error sources were set to the nominal values. This allowed the relative impact of each error source to be evaluated.

4.5.1 Baseline Filter. The first two scenarios involve the baseline filter for both the widelane and single frequency filters. Each filter was evaluated against the best, nominal, and worst error cases, which are presented in Table 4.3.

Table 4.4 Widelane versus Single Frequency in Baseline Filter

Test #	Scenario	Error Case	3-D RMS	$\nabla\Delta N_{err}$ RMS	$\sigma_{\nabla\Delta N}$ RMS	Round %corr	Amb. Res. %corr	Amb. Res. %incorr	Amb. Res. %unres
1	WL	Best	.063	.031	.046	100	100	0	0
2	Single	Best	.033	.051	.083	99.4	99.3	.6	.1
3	WL	Nom.	.123	.065	.046	100	100	0	0
4	Single	Nom.	.054	.101	.083	99.4	96.3	.5	3.2
5	WL	Worst	.241	.126	.046	99.2	94.8	.3	4.9
6	Single	Worst	.099	.225	.083	75.2	59.2	.4	40.4

The use of a widelane frequency improved ambiguity resolution ability, but at the expense of a larger position error. This is reasonable because, as shown in Section 2.5.7, widelaning increases the effect of error sources that are not frequency correlated (multipath and measurement noise), but does not change the effect of error sources that are frequency correlated (pseudolite position errors and tropospheric delay). The position errors and tropospheric delay are reduced when expressed in cycles, which reduces the ambiguity search space. This is clearly shown by comparing the

single frequency to widelane results for each error case. The widelane tests resulted in larger position domain errors, but smaller ambiguity errors. The remaining Monte Carlo simulation use single frequency (L1) phase measurements in order to show the contribution of each error source better, and the performance improvement of each filter enhancement.

The floating-point filter was tuned for the nominal error case for both the single and widelane observables. The agreement between the RMS ambiguity error (.101 from test 4) and RMS standard deviation (.083 from test 4) indicate how well the filter is tuned. The results also show that the filter is too conservative for the best case, and is overestimating its performance for the worst case error.

Tests 1, 2, 5, and 6 represent a mistuned filter and therefore can be used to determine how robust the filter is to mistuning. These tests indicate that the filter is fairly robust to mistuning. The percentage of correct fixes do decrease going from the nominal error case to the worst case, but the percent of incorrect fixes does not significantly change. In fact, it actually decreased for the single frequency case. The biggest change is the percentage of unresolved cases, which could be used to indicate a mistuning.

To investigate the capabilities of this algorithm fully, the filter was re-tuned for both the best and worst case single frequency filter. The re-tuning of the filter involved increasing the measurement covariance values by a factor of 2.5 for the worst case and decreasing the values by a factor of 2.5 for the best case. The results are shown in Table 4.5, along with Tests 2 and 6 for comparison. The ambiguity resolution process uses a value of "k" to determine how many standard deviations define the search area. The value of k for the worst case was set to 5 instead of 10 for this test only. This was due to a large number of unresolved fixes. The best case re-tuned filter (Test 7) had slightly larger errors in position and floating-point ambiguities, but an improved ability to resolve ambiguities. The worst case re-tuned filter (Test 8) also showed an slightly better performance in the ability to

resolve ambiguities in addition to slightly improving the floating-point position and ambiguity estimates. To summarize, the filter will perform best when it is properly tuned, but this filter can tolerate mistuning to provide adequate results.

Test #	Scenario	Error Case	3-D RMS	$\nabla\Delta N_{err}$ RMS	$\sigma_{\nabla\Delta N}$ RMS	Round %corr	Amb. Res. %corr	Amb. Res. %incorr	Amb. Res. %unres
2	Single	Best	.033	.051	.083	99.4	99.3	.6	.1
7	Retuned	Best	.036	.062	.054	100	100	0	0
6	Single	Worst	.099	.225	.083	75.2	59.2	.4	40.4
8	Retuned	Worst	.097	.222	.167	79.2	63.8	1	35.2

Table 4.5 Baseline Single Frequency Retuned

The baseline filter test showed a widelane frequency outperforms the single frequency in the ability to resolve ambiguities, but a single frequency is better in the position domain. The filter will perform best when it is properly tuned, but this filter can tolerate mistuning to provide adequate results. If the filter is producing a large number of unresolved epochs, that might indicate the measurement errors are larger than anticipated, which results in the filter overestimating its performance. If the filter is mistuned, it is better to underestimate than to overestimate its ability.

4.5.2 Error Sensitivity Analysis. This section examines the error sensitivity of each error source. The sensitivity analysis was conducted by comparing the nominal case to the best and worst case of selected error sources. The error source of interest is set to either the best or worst case error, while the remaining errors are set at the nominal values. The results are compared to the nominal error case (Test 4). The results for the best case are shown in Table 4.6.

Test #	Scenario	Error Case	3-D RMS	$\nabla\Delta N_{err}$ RMS	$\sigma_{\nabla\Delta N}$ RMS	Round %corr	Amb. Res. %corr	Amb. Res. %incorr	Amb. Res. %unres
4	Single	Nom.	.054	.101	.083	99.4	96.3	.5	3.2
9	PLE	Best	.041	.075	.083	99.4	99	.6	.4
10	Meas. Noise	Best	.051	.100	.083	99.4	97.4	.5	2.1
11	Multipath	Best	.053	.103	.083	99.5	97.1	0	2.9
12	Tropo. Delay	Best	.051	.105	.083	100	98	0	2

Table 4.6 Best Case Error Sensitivity

The errors sources that clearly stand out as the most sensitive are the pseudolite position errors (Test 9) along with the tropospheric delay (Test 12). This is reasonable because these errors are larger in magnitude than the multipath and measurement noise, in addition to being more time correlated. When the pseudolite positions (Test 9) were reduced, the percentage of correct fixes was 99, which was 2.7 percent higher than the base case. The pseudolite position errors also showed the only significant improvement in the RMS position and RMS ambiguity errors. The best case tropospheric delay (Test 12) also showed an improvement in ambiguity resolution. The best case for tropospheric delay also resulted in 100 percent correct for the ambiguity rounding, which means that every floating-point ambiguity estimate was within half a cycle of the correct ambiguity. Both the multipath and tropospheric delay scenario achieved zero percent incorrect while increasing the percent correct over the baseline filter.

A sensitivity analysis also examined the effect of changing one error source at a time to the worst case expected error. The worst case error sensitivity results are shown in Table 4.6. Each test (13-16) should show a degraded performance from the base (Test 4), with the magnitude of degradation indicating the relative sensitivity.

Test #	Scenario	Error Case	3-D RMS	$\nabla\Delta N_{err}$ RMS	$\sigma_{\nabla\Delta N}$ RMS	Round %corr	Amb. Res. %corr	Amb. Res. %incorr	Amb. Res. %unres
4	Single	Nom.	.054	.101	.083	99.4	96.3	.5	3.2
13	PLE	Worst	.083	.186	.083	89.6	74.9	.4	24.7
14	Meas. Noise	Worst	.061	.119	.083	99.4	94	.4	5.6
15	Multipath	Worst	.055	.115	.083	99.4	95.3	.6	4.1
16	Tropo. Delay	Worst	.066	.138	.083	95.3	91.9	0	8.1

Table 4.7 Worst Case Error Sensitivity

The pseudolite position error (Test 13) and the tropospheric delay (Test 16) again showed the most significant sensitivity. Only the pseudolite position error displayed a much larger change in the RMS position and floating-point ambiguity errors in comparison to the other scenarios.

The pseudolite position errors and the tropospheric delay were shown from Chapter 3 to have larger magnitudes and stronger time correlations than the measurement noise and multipath. As a result, the filter is more sensitive to these errors when examining the best and worst cases separately for each error source. Only the position errors impacted RMS position and RMS ambiguity errors significantly.

4.5.3 Filter Enhancements. The five filter enhancements that were developed in this research included code averaging, bias correction terms, optimal smoothing, measurement covariance weighting, and tropospheric model error states. This section evaluates the filter enhancements against the best, nominal, and worst case errors with a single (L1) frequency. Tests 2, 4, and 6 are used as the baseline filter for comparison. Note that the filter tuning is the same for best, nominal, and worst case errors (i.e. the re-tuned filter was not used).

The tropospheric model error states will be analyzed for a single run before describing the Monte Carlo results. Recall from Chapter 3 that there were two implementations developed—two separate states for the mobile and reference receiver error percentages, and a single state for the combination error percentage. When the only measurement error was the tropospheric delay, both filters performed well, which can be seen in Figure 4.9.

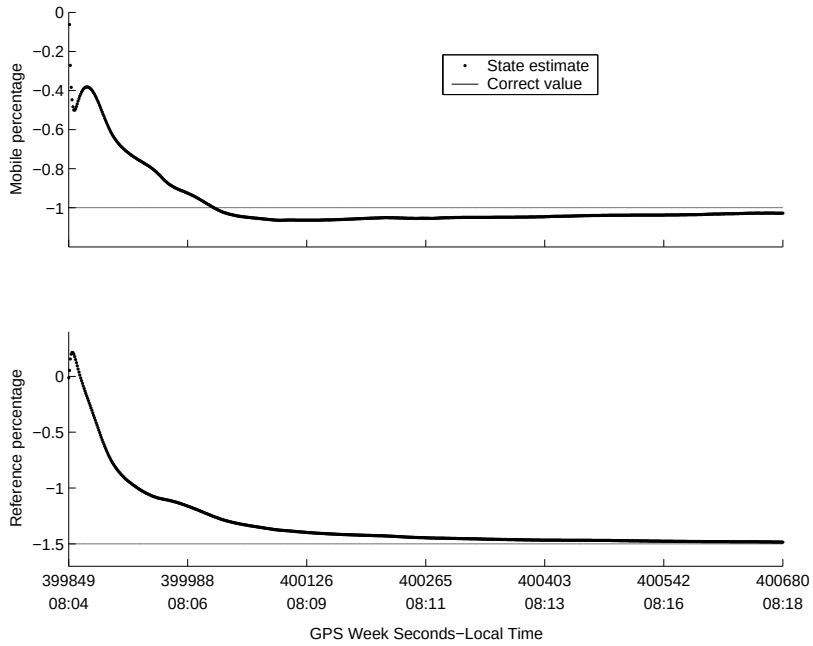

Figure 4.9 Mobile and Reference Rcvr. Estimated Tropospheric Model Error Percentages for Tropospheric Delay Only

Notice that the state estimates are plotted as points, but appear as a thicker line than the plot of the correct value. The next two figures were plotted in the same manner.

When the other measurement errors are added, the filter is still able to estimate the mobile percentage successfully, but not the reference percentage, as shown in Figure 4.10.

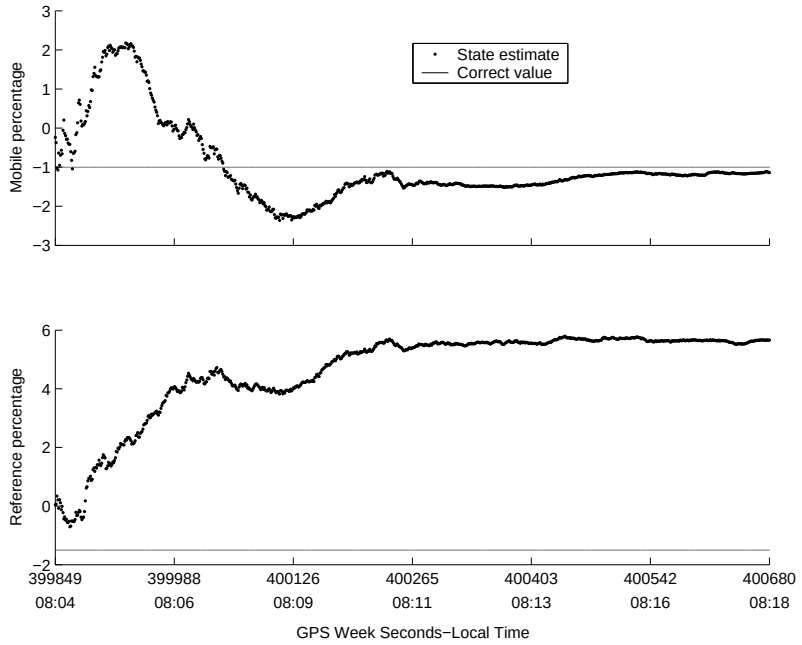

Figure 4.10 Mobile and Reference Rcvr. Tropospheric Model Error Percentages with all Measurement Errors

At first it was thought that the reference error percentage was un-observable, due to lack of relative motion between the reference receiver and pseudolites. However, if this were true, the filter would not have been able to estimate the percentage when only the tropospheric delay was present. Instead, the lack of relative motion for the reference receiver means that the pseudolite position errors cause biases in the measurements. This obscures the filter from correctly discerning the tropospheric model scale factor error, which looks like pseudolite location biases. This motivated the single tropospheric state as previously discussed in Chapter 3. When this implementation was used, the filter-estimated percentages typically fell between the correct mobile and reference receiver percentages, as shown in Figure 4.11. The single tropospheric state implementation was used for the Monte Carlo simulations.

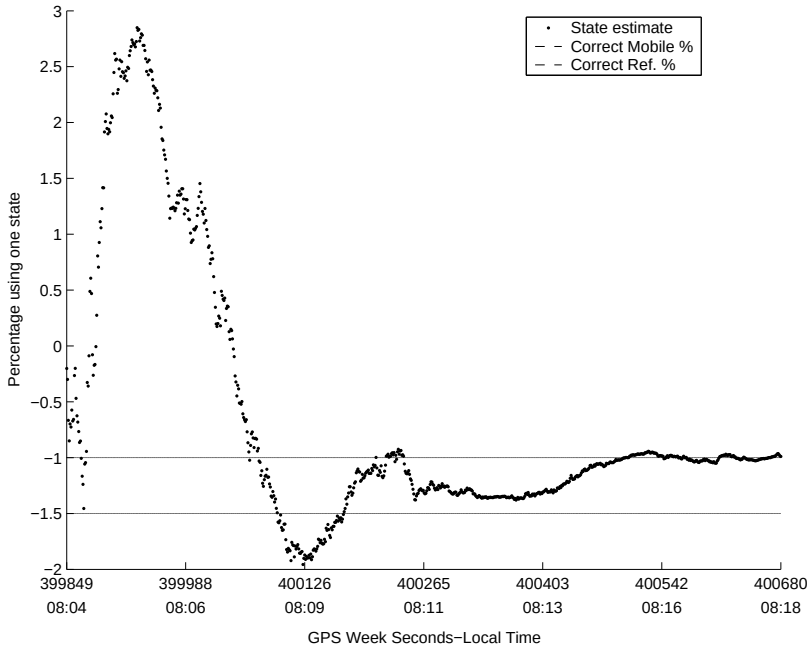

Figure 4.11 Combined Tropospheric Model Error Percentage with all Measurement Errors

The correct mobile percentage was -1 percent and the correct reference percentage was -1.5 percent. This plot shows the filter converging to a value close to the correct mobile percentage.

Table 4.8 shows the results for the best error case. Both of the enhancements that targeted the tropospheric delay improved the ambiguity resolution process. The filter's performance was very high for the best case and there was relatively little room for improvement. Note that the optimal smoother actually resulted in slightly worse results than the baseline filter. After the filter has converged, typically there is little, if any, benefit from smoothing due to small dynamics driving noises. The results in the table indicate the same 10 points in time at which the smoother did not outperform the filter. If another 10 points in time are selected, the smoother could have outperformed the filter. Basically, after a filter has converged and has a really good dynamics model, a smoother cannot be expected to outperform a filter in

a consistent, significant manner. Only the tropospheric model error states increased the accuracy of the filter in the position domain.

Test #	Scenario	Error Case	3-D RMS	$\nabla\Delta N_{err}$ RMS	$\sigma_{\nabla\Delta N}$ RMS	Round %corr	Amb. Res. %corr	Amb. Res. %incorr	Amb. Res. %unres
2	Single	Best	.033	.051	.083	99.4	99.3	.6	.1
17	PR Ave.	Best	.033	.049	.083	99.4	98.3	.7	1
18	Bias Corr.	Best	.037	.052	.083	99.4	99.3	.6	.1
19	Smoother	Best	.041	.049	.083	99.4	98.4	.8	.8
20	Weighted R	Best	.033	.050	.069	100	100	0	0
21	Tropo. State	Best	.026	.051	.089	100	99.8	0	.2

Table 4.8 Best Case Filter Enhancement

Table 4.9 shows the results for the nominal error case. The code averaging, weighted measurement covariance, and the tropospheric model error states could have resolved 100 percent of the ambiguities correctly with simple rounding. The smoother offered the most improvement for when comparing the percentage of correct ambiguities fixes, but also slightly increased the percentage of incorrect fixes. Recall that the smoother actually decreased the performance for the best case. The code averaging, weighted measurement covariance, and the tropospheric model error states offered a more modest increase of correct ambiguities, but with zero percent of incorrect fixes. Again, the bias correction terms did not improve the filter's performance.

Test #	Scenario	Error Case	3-D RMS	$\nabla\Delta N_{err}$ RMS	$\sigma_{\nabla\Delta N}$ RMS	Round %corr	Amb. res. %corr	Amb. res. %incorr	Amb. res. %unres
4	Single	Nom.	.054	.101	.083	99.4	96.3	.5	3.2
22	PR Ave.	Nom.	.056	.111	.083	100	96.6	0	3.4
23	Bias Corr.	Nom.	.057	.110	.083	99.3	96.3	.5	3.2
24	Smoother	Nom.	.057	.107	.083	99.4	99.4	.6	0
25	Weighted R	Nom.	.053	.105	.069	100	97.9	0	2.1
26	Tropo. State	Nom.	.041	.106	.089	100	97.3	0	2.7

Table 4.9 Nominal Case Filter Enhancement

Table 4.10 shows the filter enhancements results for the worst case errors. The optimal smoother (Test 29) and the weighted measurement covariance matrix (Test 30) resulted in the highest percentage of correct fixes, but it also increased the percent of incorrect fixes. The increase in percentage of correct fixes was 27.9 for optimal smoothing and 14.7 for the weighted measurement covariance matrix. Again, code averaging (Test 27) and the bias correction terms (Test 28) showed little improvement over the baseline filter. The tropospheric model error state was the only case to show improvement in the position accuracy. It also had the best performance for simple rounding, although the ambiguity resolution improvement was slight.

Test #	Scenario	Error Case	3-D RMS	$\nabla\Delta N_{err}$ RMS	$\sigma_{\nabla\Delta N}$ RMS	Round %corr	Amb. Res. %corr	Amb. Res. %incorr	Amb. Res. %unres
6	Single	Worst	.099	.225	.083	75.2	59.2	.4	40.4
27	PR Ave.	Worst	.101	.227	.083	76.7	59.8	.2	40
28	Bias Corr.	Worst	.101	.226	.083	75.7	59.2	.5	40.3
29	Smoother	Worst	.095	.221	.083	78.9	86.9	2.9	10.2
30	Weighted R	Worst	.098	.220	.069	79.1	73.9	3.3	22.8
31	Tropo. State	Worst	.078	.217	.089	82.2	61.7	.3	38

Table 4.10 Worst Case Filter Enhancement

When compiling the results for all three error cases, the optimal smoothing and the weighted measurement covariance matrix made the largest difference in the ability to resolve ambiguities. Although they increased the percent incorrect in the worst error case, that could be improved by proper tuning or by adjusting the ratio test criteria in the ambiguity set selection process. Even though code averaging only slightly increased the performance, it is still worth implementing in an operational system in which two signals are available. It requires little computational time and provides a modest increase in the accuracy of the code measurements. The tropospheric model error state method developed in this research did improve ambiguity resolution, but not to the degree that smoothing or the weighted measurement covariance matrix was able to accomplish. As stated previously, the tropospheric model error state method was the only enhancement to reduce errors in the position domain significantly, and it had the highest percentage of correct ambiguities using simple rounding. This suggests that this enhancement could possibly outperform the other enhancements with better tuning parameters in the ambiguity resolution process. The long measurement ranges for this trajectory did not contain harsh measurement model nonlinearities. This would explain why the bias correction terms

did not significantly aid the ambiguity resolution process. The next section contains alternate trajectories that contain higher measurement model nonlinearities, with a comparison of nonlinear filtering techniques to address them.

The previous tests show the benefit of each filter enhancement, but do not show the level of performance when all the enhancements are used together. Table 4.11 shows the resulting level of improvement when all the enhancements are used, except for the tropospheric model error states. The weighted measurement covariance matrix method cannot be applied at the same time the filter is using the tropospheric model error states, and the weighted measurement covariance matrix was chosen because it aided the ambiguity resolution process to a larger degree. The table used the worst error case because it provided the case with the largest room for enhancement.

Test #	Scenario	Error Case	3-D RMS	$\nabla\Delta N_{err}$ RMS	$\sigma_{\nabla\Delta N}$ RMS	Round %corr	Amb. Res. %corr	Amb. Res. %incorr	Amb. Res. %unres
6	Single	Worst	.099	.225	.083	75.2	59.2	.4	40.4
32	All Enh.	Worst	.093	.216	.069	80.8	76.3	2.4	21.3

Table 4.11 All Enhancement Test for Worst Case

It is surprising to note that the baseline filter with only a smoother performed better than Test 32, where other enhancements were also used. Further tests were conducted to explain this phenomenon by adjusting the scaling factor in the weighted measurement covariance (see Equation 3.60). When the scaling factor, which was previously .03, was increased to .05, the filter (with both the smoother and weighted measurement covariance matrix) correctly resolved 84.5 percent of the ambiguities (with an incorrect percentage of 2.6 percent). When the scaling factor increased, the RMS ambiguity covariance also increased from .069 cycles to .079 cycles, which was much closer to the baseline filter RMS ambiguities covariance of .083 cycles. This

shows that the weighted measurement covariance matrix is sensitive to the scaling factor.

This test alone would suggest that the scaling factor should be increased for all the tests using the weighted measurement covariance. Recall that the worst error case effectively has filter mistuning, and the lower ambiguity covariance from the weighted measurement covariance matrix enhancement would represent a higher degree of mistuning than the baseline filter. This mistuning explains why the smoother had better performance without a weighted measurement covariance for the worst error case. In order to prove this, two additional tests were conducted with exactly the same parameters as Test 25, except with different scaling factors in the weighted measurement covariance formulation. The results are listed in Table 4.12 for scaling factors of .05 and .06, along with the original scaling factor of .03 (Test 25). It is clear that increasing the scaling factor for the nominal error case degrades performance. These results support the claim that the lack of performance in the worst error case was due, in large part, to filter mistuning. It is important to note that the weighted measurement covariance greatly increased accuracy of ambiguity resolution in all three error cases.

Test #	Scenario	Error Case	3-D RMS	$\nabla\Delta N_{err}$ RMS	$\sigma_{\nabla\Delta N}$ RMS	Round %corr	Amb. Res. %corr	Amb. Res. %incorr	Amb. Res. %unres
25	Weighted .03	Nom.	.053	.105	.069	100	97.9	0	2.1
33	Weighted .05	Nom.	.057	.108	.079	99.4	87.7	.5	11.8
34	Weighted .06	Nom.	.059	.110	.084	99.2	86.0	.6	13.4

Table 4.12 Weighted Measurement Covariance Matrix Scaling Factor Comparison

The value of τ for the tropospheric model error states was set to 75 hours for the previous cases, which was discussed in Chapter 3. This tuning parameter was

also set to 5 minutes and 1 sec to evaluate its impact, with results shown in Table 4.13.

Test #	Scenario	Error Case	3-D RMS	$\nabla\Delta N_{err}$ RMS	$\sigma_{\nabla\Delta N}$ RMS	Round %corr	Amb. Res. %corr	Amb. Res. %incorr	Amb. Res. %unres
26	Tropo 75 h	Nom.	.041	.106	.089	100	97.3	0	2.7
33	Tropo 5 m	Nom.	.045	.108	.094	100	95.7	0	4.3
34	Tropo 1 s	Nom.	.048	.109	.088	99.4	96.1	.6	3.3

Table 4.13 Tropospheric Model Error States Time Constant Comparison

When the time constant decreased, the values in the tropospheric model error state (x_{10}) appeared to be more uncorrelated in time. As the time constant decreases, the filter is effectively allowing the state estimate, which is absorbing some of the multipath and pseudolite location errors, to vary more with time. This is important because the errors themselves vary with time.

4.6 Alternate Trajectories with Nonlinear Filter Comparisons

This section compares three different trajectories and analyzes the impact of measurement model nonlinearities for each one. The evaluation for each trajectory involves investigation of nonlinear filtering techniques to include 1) EKF with bias correction terms, 2) a modified truncated second order filter, and 3) a modified Gaussian second order filter [20].

4.6.1 Landing Scenario. The previous simulations used a flight trajectory that stayed approximately 3 kilometers above the pseudolite network. The slant ranges for this trajectory were 3 to 32 kilometers. At these ranges, the bias correction terms did not show significant improvement over the EKF in terms of ambiguity

estimation and ambiguity resolution performance. This section investigates a landing scenario and the impact of measurement model nonlinearities.

The trajectory is actually the takeoff of a C-12, which was reversed to emulate a landing scenario. Figure 4.12 shows the 3-D trajectory (with projections onto each axis), while Figure 4.13 shows the same pseudolite and reference receiver locations with the ground projection of this new trajectory. The maximum range for the pseudolite signals was again set to 32 kilometers. This trajectory resulted in 9-10 pseudolites in view. It is important to note that, in this trajectory, the shortest range to the mobile receiver was 2.5 kilometers.

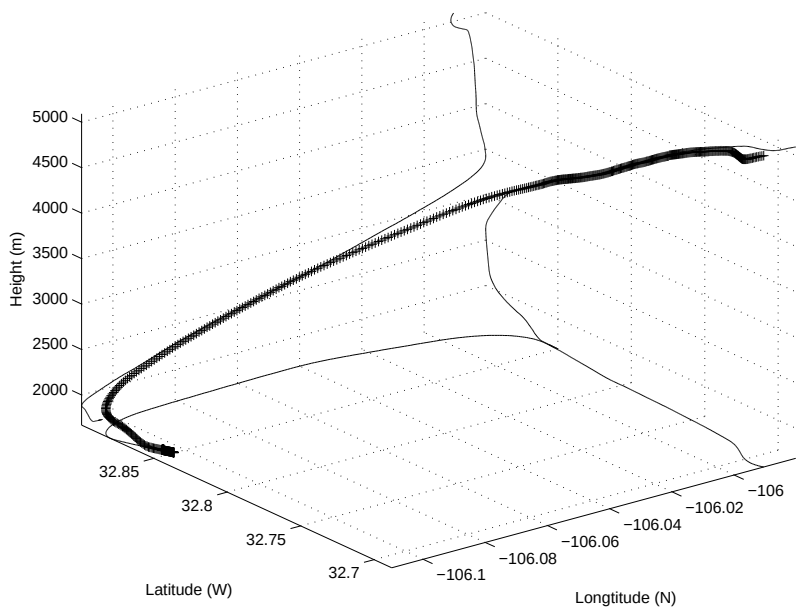

Figure 4.12 Landing Scenario Trajectory Plot

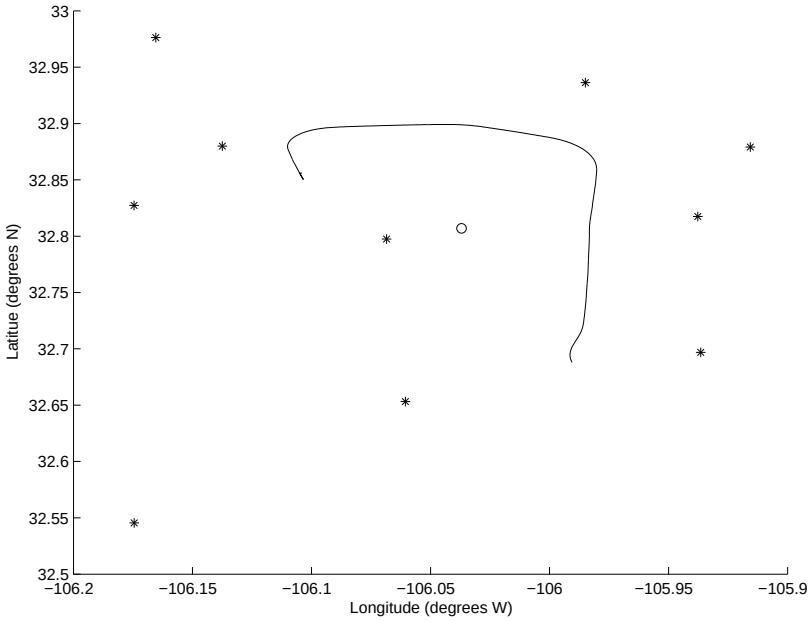

Figure 4.13 Landing Scenario Pseudolite and Reference Receiver Locations with Trajectory Ground Projection

The results shown in Table 4.13 show that only a slight advantage is gained with bias correction terms or second order filtering, with the majority of the benefit coming from the bias correction terms. Note that the bias correction terms alone did better than either second order filter.

Table 4.14 Widelane versus Single Frequency in Baseline Filter

Test #	Scenario	Error Case	3-D RMS	$\nabla\Delta N_{err}$ RMS	$\sigma_{\nabla\Delta N}$ RMS	Round %corr	Amb. Res. %corr	Amb. Res. %incorr	Amb. Res. %unres
35	EKF	Nom.	.298	.129	.084	98.9	99.7	0	.3
36	Bias	Nom.	.430	.129	.084	99	99.8	0	.2
37	Trun.	Nom.	.438	.130	.083	98.9	99.8	0	.2
38	Gaus.	Nom.	.443	.130	.084	98.7	99.8	0	.2

This landing trajectory also did not fully challenge the baseline EKF, because the shortest ranges were still in excess of 2.5 kilometers. These tests are still of general value, however, because they demonstrate that the algorithm performs well with a different trajectory.

4.6.2 Alternate Landing Scenario. Further test were conducted to attempt to challenge the filter with severe measurement model nonlinearities. The simulated flight trajectory was shifted in all three directions to bring the end of the flight within 100 meters of PRN 8 for the last 226 seconds of the 832 second mission (with the last 192 seconds at exactly 73 meters due to a stationary trajectory). This alternate landing scenario is shown in Figure 4.14.

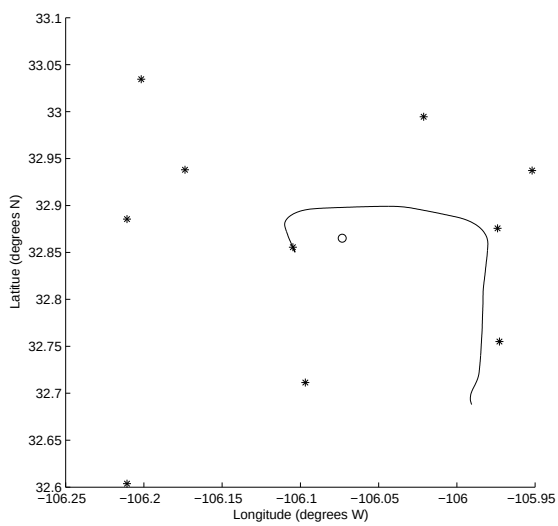

Figure 4.14 Alternate Landing Scenario Pseudolite and Reference Receiver Locations with Trajectory Ground Projection

The results of one simulation run for this trajectory are shown in Figures 4.15 and 4.16 for the EKF and EKF with bias correction terms. The EKF-only case showed a slight increase in ambiguity error for the end of the run. The addition of the bias correction terms did not significantly improve the performance of the filter.

The modified Gaussian second order filter was very similar to the EKF with bias correction terms.

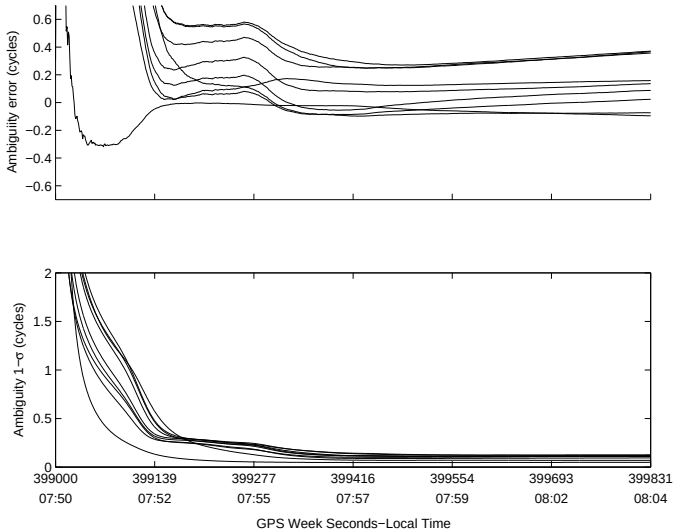

Figure 4.15 Single Simulation Run for Alternate Landing Trajectory with an EKF

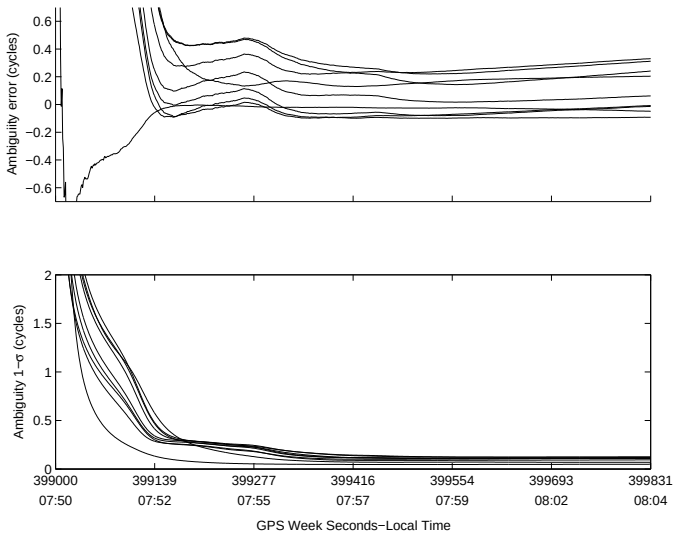

Figure 4.16 Single Simulation Run for Alternate Landing Trajectory with an EKF with Bias Correction Terms

Note that one of the ambiguities in Figure 4.16 is worse than it was in Figure 4.15. This suggests that the addition of the bias correction terms actually degraded the performance at the start of the run.

4.6.3 Take Off Scenario. The alternate landing trajectory was inverted to simulated an aircraft taking off and experiencing the harsh nonlinearities right from the start of the simulation. This forces the filter to deal with the nonlinearities before the filter has converged. The EKF in this scenario did require more time to converge and in that time it experienced the large ambiguity errors shown in Figure 4.17.

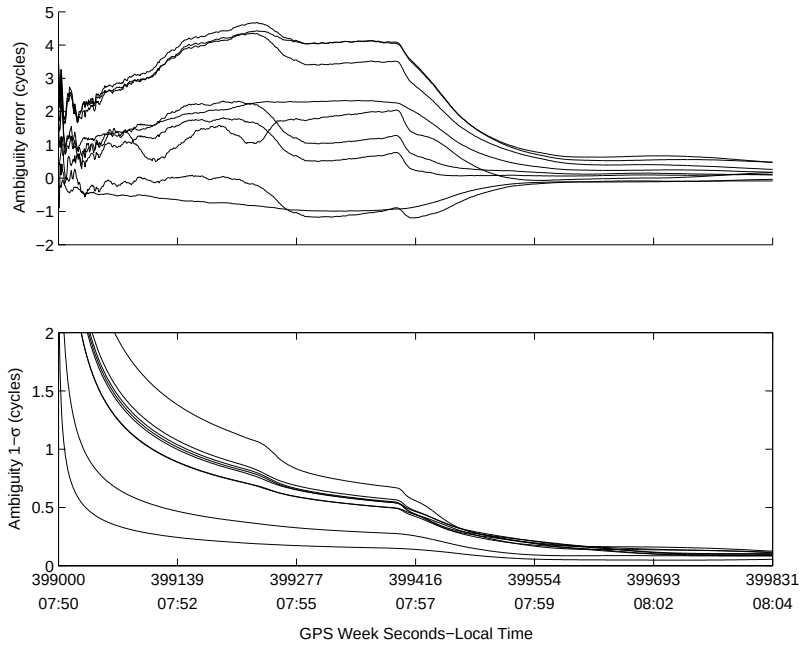

Figure 4.17 Single Simulation Run for Takeoff Trajectory with an EKF (Initialized 73 meters away from a Pseudolite)

When the bias correction terms were added, the filter diverged very quickly (within 15 seconds). The bias correction factors are a function of the covariance matrix. In the baseline filter, the position covariance values used a standard deviation of 100 meters. The filter diverged because the position standard deviation was

greater than the actual distance between the transmitter and receiver, which caused problems with the line of sight vectors.

Two fixes for this problem were attempted. The first was to delay the use of the bias correction terms until after 20 seconds had elapsed, to allow the covariance values to decrease. This was successful, and it produced results nearly identical to the EKF case without bias correction terms. Lowering the covariance to a standard deviation of 4 meters was the second attempted solution. This also solved the divergence problem.

For the application to require any second order nonlinear filtering (full-state or just bias correction terms), the position error must be significant in relation to the range between the transmitter and receiver. Second-order filtering must be applied with care, because it is sensitive to the covariance initialization. When the bias correction terms are used with large covariance values, divergence can occur. The modified truncated and modified Gaussian second-order filters did not provide sufficient improvement over the EKF with bias correction terms to warrant any further investigation for reference system applications. Any further examination of second-order filter techniques for pseudolites could be of value for indoor pseudolite applications, where the nonlinearities are significant enough to warrant such high-order nonlinear filtering.

4.7 Optimal Smoothing

Optimal smoothers not only increase the performance of the floating-point filter and the ability to resolve ambiguities, but they also increase the true window over which ambiguity techniques can be applied in a post-processing application. Typically, the EKF took up to 7 minutes (half of the simulation) to converge on the floating-point solution. That is why ambiguity resolution techniques were only applied in the second half of the test run. Optimal smoothing enables ambiguity

resolution at the start of the mission if real-time processing is not of critical importance.

The section on optimal smoothers in Chapter 3 detailed exactly how the smoothing algorithm was modified for base prn changes, pseudolites coming into view, and pseudolites going out of view. In order to test the smoother for a double difference base PRN change, the base was manually changed from 3 to 8 and the visibility plot is shown in Figure 4.18.

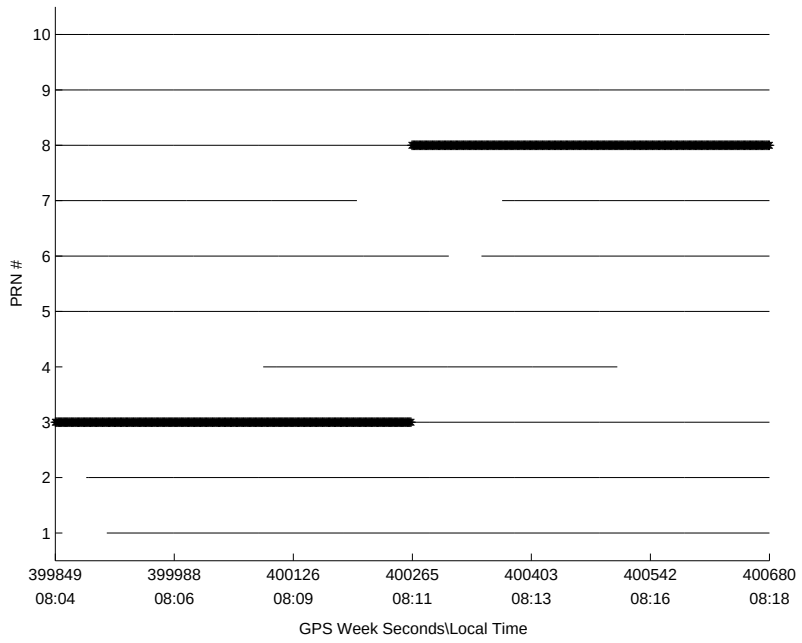

Figure 4.18 Visibility Plot for 20 Kilometer Maximum Range

The smoother allows a converged solution right at the start of the test mission and can be seen in Figure 4.19. This figure shows the RMS ambiguity error in the top subplot and the RMS standard deviations of the ambiguities in the bottom plot. The forward filter is depicted with a solid line, while the smoothed estimates are shown with a dotted line.

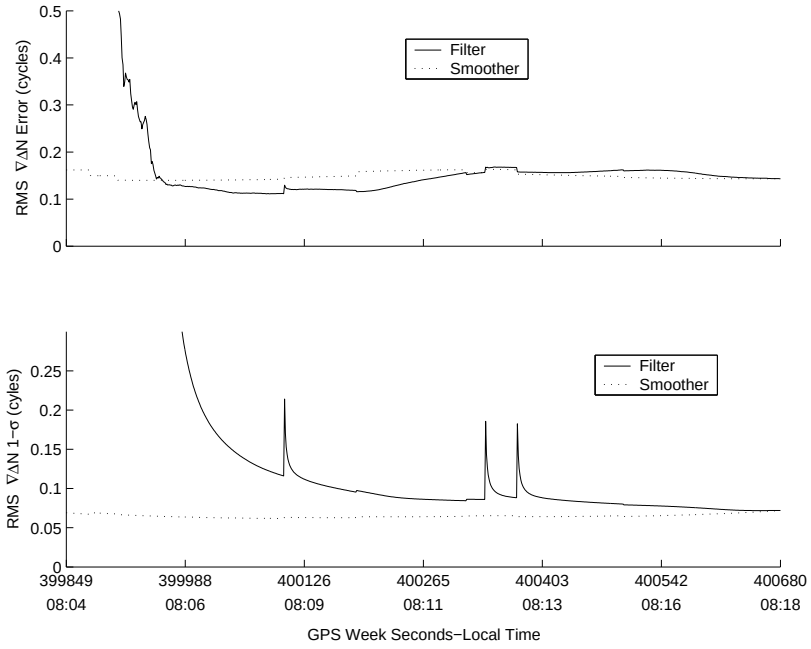

Figure 4.19 Filter and Smoother RMS Ambiguity Error and Ambiguity 1-/sigma Plots

These plots demonstrate the the smoother could handle the pseudolites coming into and going out of view along with the changing base prn for double differencing. The spikes in the plots are a result of a pseudolite coming into view. Recall that the variance assigned to a pseudolite that just came into view is rather large in comparison to the remaining variances, which affects the RMS of the standard deviations.

4.8 Summary

This chapter first described the simulation parameters, scenario descriptions, and test case definitions. This background was required to set the stage for the single run and Monte Carlo results. In the single run analyses, the filter was evaluated based on the position and ambiguity estimation errors in addition to using the flight vehicle velocities and accelerations to explain some of the results from

the residuals. The Monte Carlo simulations evaluated a single frequency filter versus one using a widelane observable. The Monte Carlo simulations also included a sensitivity analysis of each error source and a comparative analysis of five filter enhancements. Alternate flight trajectories were investigated with nonlinear filtering techniques. Lastly, the optimal smoother was shown to increase the epochs available for ambiguity resolution.

V. Conclusions and Recommendations

5.1 Overview

This research presented the theory, models, and simulation results for a pseudolite-based flight reference system. Previous research has indicated that pseudolites can be used successfully for positioning and ambiguity resolution. This research concentrated on the application and adaption of GPS carrier-phase differential techniques to pseudolite measurements for a flight reference system application. The adaptations were required due to the differences in pseudolite versus GPS navigation.

The baseline algorithm consisted of an extend Kalman filter that used a double differenced code and carrier-phase measurement. Widelane or single frequency measurements could be used in this filter, in addition to a number of possible filter enhancements. These filter enhancements included code averaging (when two codes are available), bias correction terms (emulating second order filtering), optimal smoothing, and two methods for reducing the residual tropospheric delay that exists after a tropospheric model has been applied. The first method implemented a weighted measurement covariance matrix based on the tropospheric-model-predicted delays. The second method for reducing residual tropospheric error was explicitly modelling it in the filter.

5.2 Conclusions

A single run of the filter was evaluated to show typical performance of the floating-point filter. The performance was investigated through analysis of the position and ambiguity accuracies, in addition to the velocities, accelerations, and residuals. Although the primary objective was to evaluate ambiguity resolution performance, position accuracy was also important. The accuracy of the algorithm in the position domain is also relevant if a pseudolite-only system is desired (i.e., one

based solely on pseudolite signals). In general, the floating-point filter was typically accurate to within 10-15 centimeters for the position and two-tenths of a cycle for the ambiguities (for single frequency measurements). For widelane measurements, the ambiguity accuracy was within a tenth of a cycle, with a position accuracy within 20-25 centimeters. The performance was investigated by single run analysis and supported by Monte Carlo simulations. For tested trajectories, the filter required 5-7 minutes to converge. Converged estimates were available at the start of the run when an optimal smoother was applied.

The influence of the code measurements and the relative motion between transmitters and receivers are the two factors that allow the filter to converge on the ambiguities. When the code was essentially removed, by increasing the measurement covariance values to an extremely high value, the filter was forced to rely on the relative motion only. This actually increased the speed of convergence with no degradation of accuracy. This suggested that relative motion was the primary driver for ambiguities' convergence. This was confirmed when the filter processed measurements from a stationary trajectory, which decreased the accuracy of the ambiguity estimates by an order of magnitude. This suggests that a pseudolite-based flight reference system does not require code measurements, although code measurements will add robustness to the system.

Monte Carlo simulations were also conducted to evaluate filter performance further. This analysis included an evaluation of widelane versus single frequency, a sensitivity analysis of each error source, and a comparative analysis of five filter enhancements. The widelane measurement reduced the magnitudes of the ambiguity errors, at the expense of increasing the errors in the position domain. As a result, ambiguity resolution was more easily conducted with a widelane frequency than with a single frequency implementation. The filter, using widelane frequency measurements, was able to resolve 100 percent of the ambiguities correctly, while the filter using single frequency measurements was able to resolve 96.3 percent correctly

and .5 percent incorrectly. The difference was more dramatic for larger measurement error cases. Given correctly resolved ambiguities, a single frequency solution has smaller measurement errors than a widelane frequency solution. The filter performed well enough to assert that a single frequency may be all that is required in a fielded system.

The expected level of measurement errors was increased and decreased by a factor in order to characterized filter performance to different levels of measurement error. First, the filter was not altered and evaluated for each of the different levels of measurement errors. This represented a filter mistuning (i.e., either the filter was over- or under-estimating its performance), which allowed the robustness of the filter to be tested. The second type of test involved re-tuning the filter in order to evaluate its performance with the correct level of measurement error. The re-tuned filter improved the filter performance from 99.3 percent resolved correctly to 100 percent for the best case, and 59.2 percent resolved correctly to 63.8 percent for the worst case.

The sensitivity analysis for each error source suggested that the pseudolite position errors and the residual tropospheric error were the dominant error sources. Great care should be taken when surveying the antenna positions of the pseudolites and reference receiver. The filter sensitivity to the un-modelled tropospheric delay error motivated two of the filter enhancements developed as part of this research—the weighted measurement covariance matrix and tropospheric model error states. The weighted measurement covariance matrix method utilized the tropospheric model output in selecting measurement uncertainty values based on the predicted tropospheric delay. This relative weighting of measurement uncertainty was based on the range and elevation angle (i.e., the longer the range and/or lower the elevation angle, the larger the predicted tropospheric delay and thus uncertainty magnitude).

The second enhancement explicitly estimated the tropospheric model error as an additional state in the filter. The error, when expressed as a percentage, was the

modelled as a first order Gauss markov process. Initially, the error percentage of the mobile receiver and reference receiver were modelled separately. The filter could successfully estimate the percentage of tropospheric model error in the absence of measurement noise, multipath, and pseudolite location errors. When these error sources were included in the measurement-corrupted ranges, the filter correctly estimated the mobile error percentage, but not the reference error percentage. The lack of motion between the reference receiver and the pseudolites caused the pseudolite location errors to be bias-like. The filter was apparently unable to distinguish the tropospheric model error from the biased multipath and pseudolite location error present at the reference receiver. This problem suggested the use of a single tropospheric state that included the error percentage of both receivers. This implementation successfully improved ambiguity resolution, and was the only enhancement that reduced errors in the position domain.

The other filter enhancements included code averaging, second order filtering, and optimal smoothing. Neither the code averaging nor the bias correction terms significantly enhanced the ambiguity resolution process. The bias correction terms from a second order filter were implemented to improve the linearization approximation for the extended Kalman filter. The effect of the measurement model nonlinearities are attributed to two factors. The first is the degree of uncertainty of the receiver, specifically in a direction orthogonal to the line of sight between a transmitter and receiver. The second factor associated with nonlinearities is short transmission ranges which result in more spherical wavefronts of the received signals. Multiple trajectories for a practical flight reference system were tested to investigate the impact of measurement model nonlinearities and the benefit of the addition of bias correction terms or second order filters. It was concluded the level of uncertainty in the receiver position is so small, when compared to the line-of-sight ranges, that bias correction terms and second order filters are not helpful for the tested trajectories. If the uncertainty is significant when compared to the ranges (like would

be the case for indoor pseudolite applications), further exploration of second order nonlinear filtering techniques is warranted.

The optimal smoothing algorithm developed by Meditch [20] is not tolerant to the state and covariance matrices changing dimensions between measurement updates. The number of ambiguity states varies between epochs based on the number of visible pseudolites. This is caused by pseudolites coming into view and going out of view. The existing smoothing algorithm cannot handle the state dimension changes. The smoother calculates a state vector and covariance matrix at the current time t_i, based on the filter state and covariance at the current time t_i, and both the filter and smoother outputs at the future time t_{i+1}. As part of this research, the smoothing algorithm was modified to allow the number of ambiguity states to change between epochs. The smoothing algorithm could not tolerate a state to represent one quantity at one epoch and a different quantity at the next. For GPS and pseudolite applications this will occur when a base double difference PRN goes out of view. The smoothing algorithm was also modified to allow a change in the base double difference PRN. A translation matrix was formed based on the base PRNs at two adjoining epochs and the vector of visible pseudolites. The translation matrix was applied to both the state vector and covariance matrix to allow the smoothing algorithm to form the smoothed state and covariance estimate properly.

The position and ambiguity solutions from the floating-point filter suggest that the pseudolite ambiguities can be resolved with a pseudolite-only system, and that further integration with an INS or other measurement sources is not required to obtain high-accuracy position. This research concluded that carrier-phase measurements with resolved ambiguities can be produced from pseudolite signals to incorporate and improve accuracy, especially during periods of GPS jamming, to flight reference systems.

5.3 Contributions

This thesis has provided contributions in various areas of research. The following list details these contributions.

- The largest contribution of this thesis is the development and testing of the navigation filter for a pseudolite-based flight reference system. Although very similar to a GPS navigation algorithm, this design concentrated on the differences between GPS and pseudolite systems.
- The Meditch optimal smoothing algorithm was modified to handle a state and covariance matrix with changing dimensions. It was also adapted for changes in the quantities that are represented in the matrices. These adaptations can be easily extended to GPS navigation applications.
- The weighted measurement covariance matrix was developed as part of this research. This method takes advantage of tropospheric model predictions to weight the expected variance of the measurements. This significantly improved the ambiguity resolution of the filter.
- The tropospheric model error states were also developed as an alternative method for reducing tropospheric delay error. This included an additional state that also aided ambiguity resolution. This enhancement also improved the accuracy of the filter in the position domain.
- This research included the analysis of the bias correction terms and two second order filters to reduce the effect of measurement model nonlinearities. The analysis indicated periods when divergence can occur with bias correction terms and ways to eliminate the divergence.

5.4 Recommendations

The filter in this research performed well in its ability to resolve pseudolite carrier-phase ambiguities, and further research and evaluation for this concept is

warranted. The following recommendations are included to provided to guide the next logical steps for a pseudolite-based flight reference system.

- Apply the filter to real pseudolite flight test data. It will be necessary to find a suitable reference system for comparison. Pseudolite data is available from the original Holloman test along with tape measure results [25]. However, the geographic size of this test was fairly small, and it will therefore not fully challenge the filter with significant tropospheric error.
- Incorporate an inertial system to compare the performance of a Pseudolite/Inertial Navigation System (PL/INS) to a pseudolite-only system. The coupling of an inertial system with pseudolite measurements should only improve the performance of the floating-point filter, and would be helpful if there are pseudolite measurement dropouts. The Kalman filter used in this research would have to be converted to an error-state Kalman filter that estimates the error in the inertial system.

  This recommendation is relatively easy to implement if real flight test data is available for both GPS and an INS. The fixed-integer solution from the GPS receiver could be used as the true trajectory in order to simulate pseudolite measurements that are corrupted with simulated measurement errors. The filter would use the real INS data and the simulated pseudolite measurements.
- Implement a Multiple Model Adaptive Estimation (MMAE) algorithm for the set determination function of the ambiguity resolution process. This would replace the ratio test of the residuals with parallel Kalman filter conditioned on each possible set of ambiguities [15].
- MMAE techniques can also be applied to reducing the residual tropospheric error. This could be implemented instead of the weighted measurement covariance or the tropospheric model error states.

- Model each visible pseudolite with a separate state for the tropospheric model error state method. If the time constant is lowered, the filter may be able to reduce the pseudolite position error and multipath.
- Develop a practical method that selects the best period of time to perform the ambiguity search process. This decision should be based on pseudolite visibility, magnitude of acceleration of test vehicle, and size of ambiguity covariance values. This research applied ambiguity resolution techniques to epochs scattered throughout the entire data set, with the exception of the first few minutes to allow the filter to converge. Selecting the best time conditioned on a high number of visible pseudolites, small accelerations of the test vehicle, and low ambiguity covariance values should provide a better methodology for a practical system. If not all the pseudolites were visible during this period, the filter can use the fixed ambiguity solutions with reduced covariances to reflect that these are the correct ambiguities and iteratively solve for the remaining ambiguities.

Bibliography

1. Athans, M. and others. "Suboptimal State Estimators for Continuous-time Nonlinear Systems from Discrete Noisy Measurements." *IEEE Transactions Automatic Control*. 504–518. 1968.

2. Changdon, Kee. "Precise Calibration of Pseudolite Positions In Indoor Navigation System." *Proceeding of the 12th International Technical Meeting of the Satellite Division of the Institude of Navigation (ION GPS-95)*. Sept, 1999.

3. Chao, C.C. "The Tropospheric Calibration Model for Mariner Mars." JPL Technical Report, 1971.

4. Chen, D. "Fast Ambiguity Search Filter (FASF): A Novel Concept for GPS Ambiguity Resolution." *Proceedings of the 6th International Technical Meeting of the Satellite Division of the Institude of Navigation (ION GPS-93)*. Sept, 1993.

5. Cobb, H. Stewart. "Precision Landing Tests with Improved Integrity Beacon Pseudolites." *Proceeding of the 8th International Technical Meeting of the Satellite Division of the Institude of Navigation (ION GPS-95)*. September 12-15, 1995.

6. Cobb, H. Stewart. "Practical Investigations on DGPS For Aircraft Precision Approaches Augmented by Pseudolite Carrier Phase Tracking." *Proceeding of the 10th International Technical Meeting of the Satellite Division of the Institude of Navigation (ION GPS-95)*. September 12-15, 1997.

7. Cobb, H. Stewart and others. "Theory and Design of Pseudolites." *Proceedings of the National Technical Meeting of Institude of Navigation*. Sept, 1994.

8. Dai, Liwen and others. "Pseudolite applications in positioning and navigation: Modeling and geometric analysis." *Proceedings of the ION-KIS-2001*. 482–489. 2001.

9. Denham, W.F. and S. Pines. "Sequential Estimation when Measurement Function Nonlinearity is Comparable of Measurement Error," *Journal of AIAA*, *4*:1071–1076 (1966).

10. Dierendonck, A.J. and P. Enge. "GIC/Wide Area Differential GNSS Signal Design." *Proceedings of DSNS-93*. 1993.

11. Elrod, Bryant and others. "Testing of GPS Augmented with Pseudolites for Precision Approach Applications." *Proceedings of the 7th International Technical Meeting of the Satellite Division of the Institude of Navigation (ION GPS-94)*. Sept, 1994.

12. Ford, Tom and others. "HAPPI - a High Accuracy Pseudolite/GPS Positioning Integration." *Proceedings of the ION-GPS-96*. 1719–1728. Sept, 1996.

13. Glickman, Todd S. *Glossary of Meterology* (Second Edition). Boston, MA: Amercian Meterological Society, 2000.

14. Hebert, Jeffrey M. *Velocity Determination For An Inverted Pseudolite Navigation Reference System*. MS thesis, Air Force Institute of Technology, 1995.

15. Henderson, Paul E. *Development and Testing of a Multiple Filter Approach for Precise DGPS Positioning and Carrier-Phase Ambiguity Resolution*. MS thesis, Air Force Institute of Technology, 2001.

16. Land, Tom and others. "Implementaion of the Inverted GPS Range for Modernized GPS Testing." *Proceedings of the ION-GPS-02*. 1530–1539. Sept, 2002.

17. Lawrence, Robert S., et al. "Enhanced Precision Reference System." *Proceedings of the Institude of Navigation Annual Meeting 2001*. 304–309. June 2001.

18. Martin, Sven. "Antenna Diagram Shaping for Pseudolite Transmitter Antennas - A Solution to the Near-Far Problem." *Proceeding of the 12th International Technical Meeting of the Satellite Division of the Institude of Navigation (ION GPS-95)*. Sept, 1999.

19. Maybeck, Peter S. *Stochastic Models, Estimation, and Control, Volume 1*. Mathematics in Science and Engineering, Vol 141-1, Arlington, Virginia: Navtech Book and Software Store, 1994.

20. Maybeck, Peter S. *Stochastic Models, Estimation, and Control, Volume 2*. Mathematics in Science and Engineering, Vol 141-2, Arlington, Virginia: Navtech Book and Software Store, 1994.

21. Misra, Pratap and Per Enge. *Global Positioning System Signals, Measurements, and Performance* (First Edition). Lincoln, Massachusetts: Ganga-Jamuna Press, 2001.

22. Navtech. *High Accuracy GPS Positioning Techniques & Applications II*. Tutorial 610B. Alexandria, VA, September 2002.

23. Ndili, Awele. "GPS Pseudolite Signal Design." *Proceedings of the 7th International Technical Meeting of the Satellite Division of the Institude of Navigation (ION GPS-94)*. Sept, 1994.

24. Ormsby, Capt Charles D. *Global Positioning System Carrier Phase Integer Ambiguity Determination Using Multiple Kalman Filters-Prospectus*. PhD dissertation, Graduate School of Engineering, Air Force Institute of Technology (AETC), Wright-Patterson AFB OH, july, 2002.

25. Raquet, John and others. "Development and Testing of a Mobile Pseudolite Concept for Precise Positioning," *Journal of The Institue of Navigation*, *43*:149–165 (1996).

26. Raquet, John F. Class Notes to EENG 533, Air Force Institute of Technology.

27. Raquet, John F. Class Notes to EENG 633, Air Force Institute of Technology.

28. Raquet, John F. *Development of a Method for Kinematic GPS Carrier-Phase Ambiguity Resolution Using Multiple Reference Receivers*. PhD dissertation, University of Calgary, Calgary, Alberta, 1998.

29. Rizos, C. and S. Han. "A New Method for Constructing Multi-Satellite Ambiguity Combinations for Improved Ambiguity Resolution." *Proceeding of the 8th International Technical Meeting of the Satellite Division of the Institude of Navigation (ION GPS-95)*. September 12-15, 1995.

30. Stansell, T. "Recommended Pseudolite Signal Specification." *Navigation: Journal of The Institute of Navigation Vol 3*. 1986.

31. Teunissen, P. "The Least-Squares Ambiguity Decorrelation Adjustment: A Method for Fast GPS Integer Ambiguity Estimation," *Journal of Geodesy, Springer-Verlag* (1995).

32. Toda, N.F. and others. "Region of the Kalman Filter Convergence for Several Autonomous Navigation Modes," *Journal of AIAA*, *7*:622–627 (1969).

33. Van Dierendonck, A.J. "Local Differential Tropospheric Delay Corrections." Internal Memo for RTCA Special Committee 159 Working Group 4, August,.

34. Vanek, Barry J. *GPS Signal Offset Detection and Noise Strength Estimation in a Parallel Kalman Filter Algorithm*. MS thesis, Air Force Institute of Technology, 1999.

35. Weiser, Martin. "Development of a Carrier and C/A-Code Based Pseudolite System." *Proceeding of the 11th International Technical Meeting of the Satellite Division of the Institude of Navigation (ION GPS-95)*. Sept, 1998.

36. Young, B. *An integrated Synthetic Aperature Radar/Global Positioning System/Inertial Navigation System for Target Geolocation Improvement*. MS thesis, Air Force Institute of Technology, 1999.

Vita

Captain Terry J. Bouska grew up in New Hampton, Iowa where he graduated from the New Hampton High School in 1993. He entered undergraduate studies at Iowa State University in Ames, Iowa where he graduated with a Bachelor of Science Degree in Electrical Engineering in 1998. He was commissioned through Detachment 250 AFROTC at Iowa State University.

His first assignment was at Eglin AFB in the Air Force Research Laboratory Munitions Directorate. He spent three years as a developmental engineer conducting system engineering and program management duties. In September 2001 he entered the Graduate School of Engineering and Management, Air Force Institute of Technology. Upon graduation, he will be assigned to the 746th Test Squadron, 46th Test Group, Holloman AFB, NM where he will continue work with GPS navigation systems.

Permanent address: ON FILE

REPORT DOCUMENTATION PAGE

Form Approved
OMB No. 074-0188

The public reporting burden for this collection of information is estimated to average 1 hour per response, including the time for reviewing instructions, searching existing data sources, gathering and maintaining the data needed, and completing and reviewing the collection of information. Send comments regarding this burden estimate or any other aspect of the collection of information, including suggestions for reducing this burden to Department of Defense, Washington Headquarters Services, Directorate for Information Operations and Reports (0704-0188), 1215 Jefferson Davis Highway, Suite 1204, Arlington, VA 22202-4302. Respondents should be aware that notwithstanding any other provision of law, no person shall be subject to an penalty for failing to comply with a collection of information if it does not display a currently valid OMB control number.
PLEASE DO NOT RETURN YOUR FORM TO THE ABOVE ADDRESS.

1. REPORT DATE *(DD-MM-YYYY)*	2. REPORT TYPE	3. DATES COVERED *(From – To)*
25-03-2003	**Master's Thesis**	Jun 2002 – Mar 2003

4. TITLE AND SUBTITLE

DEVELOPMENT AND SIMULATION OF A PSEUDOLITE-BASED FLIGHT REFERENCE SYSTEM

5a. CONTRACT NUMBER

5b. GRANT NUMBER

5c. PROGRAM ELEMENT NUMBER

6. AUTHOR(S)

Bouska, Terry, J., Captain, USAF

5d. PROJECT NUMBER

5e. TASK NUMBER

5f. WORK UNIT NUMBER

7. PERFORMING ORGANIZATION NAMES(S) AND ADDRESS(S)
Air Force Institute of Technology
Graduate School of Engineering and Management (AFIT/EN)
2950 Hobson Way, Building 640
WPAFB OH 45433-7765

8. PERFORMING ORGANIZATION REPORT NUMBER

AFIT/GE/ENG/03-03

9. SPONSORING/MONITORING AGENCY NAME(S) AND ADDRESS(ES)
746th Test Squadron AFMC
Attn: Mr. Phil Simpson TS/CA
1644 Vandergrift Rd.
Holloman AFB NM 88330
DSN: 349-2125
e-mail: Philip.simpson@46tg.af.mil

10. SPONSOR/MONITOR'S ACRONYM(S)

11. SPONSOR/MONITOR'S REPORT NUMBER(S)
N/A

12. DISTRIBUTION/AVAILABILITY STATEMENT

APPROVED FOR PUBLIC RELEASE; DISTRIBUTION UNLIMITED.

13. SUPPLEMENTARY NOTES

14. ABSTRACT

Current flight reference systems are vulnerable to GPS jamming and also lack the accuracy required to test new systems. Pseudolites can augment flight reference systems by improving accuracy, especially in the presence of GPS jamming. This thesis evaluates a pseudolite-based flight reference system which applies and adapts carrier-phase differential GPS techniques. This algorithm developed in this thesis utilizes an extended Kalman filter along with carrier-phase ambiguity resolution techniques.

The simulation of the pseudolite-based positioning system realistically models measurement noise, multipath, pseudolite position errors, and tropospheric delay. A comparative evaluation of the algorithms performance for single and widelane frequency measurements was conducted in addition to a sensitivity analysis for each measurement error source, in order to determine design tradeoffs. Other analyses included the use of optimal smoothing, non-linear filtering techniques, and code averaging. Specific emphasis is given to two alternate methods, both developed in this research, for handling the residual tropospheric error after applying a standard tropospheric model.

Initial results indicate algorithm is capable of accurately resolving the pseudolite carrier-phase ambiguities, and providing a highly accurate (centimeter-level) navigation solution. The filter enhancements, particularly the optimal smoother and both tropospheric error reduction methods, improved filter performance significantly.

15. SUBJECT TERMS

Pseudolite, Global Positioning System, GPS, Flight Reference System, Navigation Reference System, Optimal Smoothing, Differential Global Positioning System, DGPS, Kalman Filter, Carrier Phase Ambiguity Resolution, Tropospheric Delay, Nonlinear Filtering,

16. SECURITY CLASSIFICATION OF:			17. LIMITATION OF ABSTRACT	18. NUMBER OF PAGES	19a. NAME OF RESPONSIBLE PERSON
a. REPORT	b. ABSTRACT	c. THIS PAGE			Raquet, John F.,Major, USAF (ENG)
U	U	U	UU	141	19b. TELEPHONE NUMBER *(Include area code)* (937) 255-3636, ext 4580; e-mail: john.raquet@afit.edu

Standard Form 298 (Rev. 8-98)
Prescribed by ANSI Std. Z39-18